QATAR UNIVERSITY

COLLEGE OF ENGINEERING

ORGANIC/INORGANIC SEMICONDUCTOR BASED OPTO-ELECTRONIC DEVICES: LIGHT DETECTORS AND DYE-SENSITIZED SOLAR CELLS.

BY

ALI SEHPAR SHIKOH

A Dissertation Submitted to

the Faculty of the College of

Engineering

in Partial Fulfillment

of the Requirements

for the Degree of

Doctorate of Philosophy in Electrical Engineering

January 2018

Committee Page

The members of the Committee approve the Dissertation of Ali Sehpar Shikoh defended on **20/12/2017**.

Dr. Farid Touati
Chair, Thesis/Dissertation Committee

Prof. Imaddin Al-Omari
Committee Member (External Examiner)

Dr. Ahmed Mohammed Massoud
Committee Member

Dr. Aboubakr M. Abdullah
Committee Member

Prof. Hazim Qiblawey
Graduate Studies Representative

Approved:

Khalifa Al-Khalifa, Dean, College of Engineering

Abstract

SHIKOH, ALI S., Doctorate : January : 2018,

Doctorate of Philosophy in Electrical Engineering

Title: Organic/Inorganic Semiconductor Based Opto-electronic Devices: Light Detectors and Dye-Sensitized Solar Cells.

Supervisor of Dissertation: Farid Touati and Zubair Ahmad.

Emerging opto-electronic devices (e.g. light sensors and solar cells) based on thin-film devices have been emphasized, owing to their many interesting properties including low cost, reduced weight, high flexibility and solution process-ability. The present study aims to enhance the performance of opto-electronic devices by means of optimizing processes associated with their fabrication and investigating different device configurations.

In the first phase, improvements in the electrical and photodetection properties of thin film devices were done. Sensitization with dyes is an emerging process to improve device optical properties. The devices sensitized using di-tetrabutylammonium cis-bis(isothiocyanato)bis(2,2′-bipyridyl-4,4′-dicarboxylato)ruthenium(II) (N719) dye showed large leakage currents (2.62 µA). To reduce this leakage current and improve rectification behavior, the N719 dye was co-sensitized with 5,12-bis([1,1':3',1''-terphenyl]-2'-yloxy)anthra[2,1,9-def:6,5,10-d'e'f']diisochromene-1,3,8,10-tetraone (AS-2). This has led to a significant reduction in the leakage current to around 0.07 µA and increased linearity and higher breakdown voltage. Nevertheless, properties like sensitivity and responsively resided within acceptable ranges. Promising photodetection results were also achieved

when the titanium dioxide (TiO_2) active layer was completely replaced with PCBM:P3HT, thereby creating a hybrid device BHJ based configuration.

In the second phase, new type of copper nanowires (CuNWs), reduced graphene oxide (rGO) and poly(2,3-dihydrothieno-1,4-dioxin)-poly(styrenesulfonate) (PEDOT:PSS) based counter-electrode was developed to replace costly indium tin oxide/platinum (ITO/Pt) electrode. The fabricated hybrid electrode exhibited high transparency alongside low sheet resistance (20 Ω cm^{-2}). Upon integration in the PV device, the CuNWs/rGO/PEDOT:PSS based counter-electrode displayed long-term stability and produced superior performance in terms of photodetection parameters such as response time, reset time and responsivity.

Nonetheless, focus was paid on optimizing the photovoltaic properties of the TiO_2 photo-electrodes, which were prepared by the electrophoretic deposition (EPD) technique. The post deposition-sintering process of these electrodes was also optimized. When integrated within DSSCs the photo-anode containing TiO_2 semiconductor layer deposited at 5 V_{DC} produced the highest efficiency of 4.2%. A further increase of 6.66% in efficiency was achieved due to the restrained nucleation and growth (i.e. altered crystallinity) of anatase nanoparticles, when single step sintering was replaced with two-step sintering process.

These results are expected to have a significant effect on solar cell and photo-detection industry by fostering improvement of thin-film opto-electronic devices.

Dedication

I delicate this thesis to my beloved family, especially

To my parents:

Without your tireless efforts and sacrifices, I wouldn't have made it this far.

To my late grandmother:

Thank you for your endless love and kindness.

Acknowledgments

The author would like to express his sincere appreciation to his lead supervisor Dr. Farid Touati (Electrical Engineering Department – Qatar University) and co-supervisor, Dr. Zubair Ahmad (CAM – Qatar University), for their encouragement and guidance. The author would also like to thank, Prof. Mohieddine Amor Benammar (Electrical Engineering Department – Qatar University), Dr. Abdul Shakoor (CAM – Qatar University), Dr. Nader Meskin (Electrical Engineering Department – Qatar University), Dr. Nasser Abdullah Alnuaimi (Director CAM – Qatar University), Dr. Mariam Al-Maadeed (Former Director CAM – Qatar University) and Dr. Peter Kasak (Technical Manager CAM – Qatar University) for their immense support during the course of the underlined research work. Further, the author would like to thank Mr. Essam Shabaan Mohamed Attia (CLU – Qatar University), Dr. Mohammad Yousuf (CLU – Qatar University) and Dr. Anton Popelka (CAM – Qatar University) for bringing extension to the author's knowledge (regarding various sets of equipment housed in Qatar University) and for being extremely helpful in getting the samples characterized. Lastly, the author would like to thank CENG Dean, office of Graduate Studies and Office of Research for their continuous support, during the course of his studies.

Table of Contents

List of Tables

List of Figures

Chapter 1: Introduction

1.1 Motivation:

The continuous pressure to produce cheaper and efficient opto-electronic devices means that the fabrication of high quality products must be achieved using only minimum amount of materials and reduced manufacturing steps [1]. Among a wide variety of opto-electronic devices used for light sensing and energy production, the ones based on semiconductor are considered promising as future technologies, Figure 1-1. However, a large barrier impeding the expansion of large-scale implementation of photovoltaic (PV) systems (solar cells and sensors) has been by far the fabrication cost [2]. One of the solutions to achieve reduction in the cost is the development of thin film devices that save both material and energy in the production process and thus render a paradigm shift in PV manufacturing [2, 3].

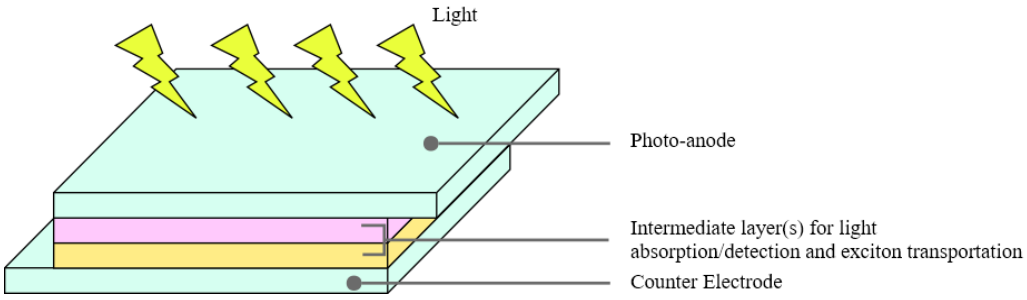

Figure 1-1: Generic diagram of an opto-electronic device.

The term thin film refers to material layers deposited by various methods such as vapour or electrodeposition with thickness too small (< 20 μm) to permit characterization by conventional mechanical procedures designed for bulk materials as described in in American Society for Testing Materials (ASTM) standards [1]. In the last decade, quality has greatly improved in most market segments as promising new thin film technologies (including gallium arsenide, copper indium gallium diselenide and organic heterojunction) demonstrate enhanced commercial viability.

In particular, organic materials unlike their inorganic counterparts exhibit physical and chemical properties that can be tailored by means of manipulating physical conditions or incorporating functional groups for the fulfilment of specific requirements [4]. Also, they offer reduced production cost, solution processability and are suitable for flexible, eco-friendly and disposable opto-electronic devices [5]. Nonetheless, organic materials have a performance that is still inferior as compared to the conventional inorganic counterparts, mainly due to the poor electrical properties such as low dielectric constant and low charge carrier mobility [6]. Thus, further research needs to be carried out in order to improve the performance of organic opto-electronic devices.

Previously, organic photovoltaic platforms have been proposed in various configurations such as tandem geometry, bulk heterojunction, dye-sensitized photosensor (DSPS) and organic-inorganic hybrid blend [7-11]. The aim of the present study is to explore various options for bringing improvement to organic opto-electronic devices based on dye-sensitized active layer and hybrid configurations.

1.2 Objectives:

Although substantial research and development (R & D) efforts have been made in order to improve the properties of thin film photo-sensors and solar cells, still further improvements are required for their market penetration. The main objective of this work is to fabricate, optimize and characterize opto-electronic thin film devices by means of improving fabrication procedures, replacing key components (i.e. counter-electrode) and employing hybrid configurations.

In pursuit of the above objective, several work packages are devised as summarized as follows:

1. Develop novel fabrication and processing techniques to optimize properties like porosity, crystallinity, thickness etc., related to dye stained semiconductor (e.g.) TiO_2 active layer.
2. Develop alternative counter-electrode that is worthy of replacing the one based on ITO/Pt configuration and enhances the number of potential applications of opto-electronic devices (solar cells and photosensors) based on dye-sensitized semiconductor layer.
3. Investigate electrical, optical and morphological characteristics related to components and devices (fabricated during the course of current study) by means of various thin-film characterization equipment including scanning electron microscope (SEM), transmission electron microscope (TEM), UV-Vis spectroscope, solar simulator etc.
4. Employ hybrid configurations for photodetection applications.

5. Analyse and interpret data and make necessary changes to bring further improvements.

1.3 Outline:

In chapter 2, literature review and theory related to thin-film photodetectors and solar cells has been presented. This chapter has been divided into two parts. The first part presents an overview of photo-sensors, their types and the figures of merit used to evaluate their performance. Later, an introduction to organic photo-detectors and the major device types employed is presented. The second part is related to dye-sensitized solar cells and the components involved in their fabrication.

Chapter 3 discusses in detail the materials required for the fabrication of copper nanowires (CuNWs) and transparent conducting electrodes based on their randomly scattered network. Materials used in the fabrication of thin film solar cells and photodetectors, are also presented. Subsequently, procedures required for the fabrication of these devices are discussed. In the end, an overview of the characterization techniques utilized for morphology and performance evaluation is presented.

Chapter 4 deals with the effect of co-sensitization of ruthenium (Ru) based N719 dye with newly developed organic dye AS-2. Initially, spectrophotometer was used to calculate the absorbance of N719 and AS-2 dyes. Later, the two dyes were mixed in different proportions and utilized in DSSC/DSPS fabrication. Lastly, the effects of co-sensitization on electrical, photodetection and photovoltaic properties of the DSSC/DSPS are analysed, compared and discussed in detail.

The integration of P3HT:PCBM bulk heterojunction (BHJ) layer in DSPS assembly is presented in Chapter 5. This chapter starts off with the description of procedures followed for the deposition of P3HT:PCBM active layer on glass substrate. Later, the fabrication of hybrid BHJ photo-sensor is discussed in detail along with the photodetection characteristics obtained for the device, in both dark and light conditions.

Chapter 6 deals with the replacement of ITO/Pt based counter-electrode with the one based on CuNWs. This chapter starts with the synthesis of CuNWs and its deposition on glass substrate. Later, methods used to reduce oxidation and RMS roughness of CuNWs based electrode, are presented. Then, the results obtained in terms of electrical, optical and durability characteristics of the counter-electrode are discussed alongside the photodetection parameters obtained for the hybrid electrode based DSPSs.

Chapter 7 relates to the optimization of TiO_2 based photo-anodes by means of employing varied electrophoretic deposition (EPD) and sintering techniques. EPD voltage level was altered and the effect of voltage changes on the morphological and electrical properties of the photo-anode/device are analysed. In addition, effects of varied post deposition sintering process on dye-sensitized photosensor (DSSC) performance are also presented and discussed in detail.

Last but not the least, the research work reported in this dissertation is summarized in Chapter 8. Future work is also suggested in the 2nd section of this chapter, followed by the conclusion of the thesis.

Chapter 2: Theory and Literature Review

2.1 Photodetector:

Photodetectors lay at the heart of any front-end of optical communication receivers. Hence, in terms of noise and bit-error rate, photodetectors determine the overall performance of optical communication systems. The function of the photodetector is to convert light into electrical signal, which is later amplified and processed till information extraction. The process of photodetection is governed by physical processes like controlling the incident light absorption and the transportation of resulting charge carriers for the production of electric signal. The relationship between the optical and electrical properties and the extent to which they could be engineered, form the basis of recent advances in photodetection technology thus fostering continuous progress in this field [12].

As shown in Figure 2-1, photodetectors can be divided into two major types i.e. photon and thermal detectors (or sensors) [13]. In case of thermal detectors, the absorption of incident radiation results in increased temperature, which is sensed as a change in electrical resistance of the material (bolometers) or as a change in the internal electrical polarization (pyrometers) [14]. They generally exhibit a response that is slow and independent of incident light's wavelength, thereby rendering them unsuitable for optical communication and photodetection. In contrast, photon detectors (or photo-electric sensors) are wavelength-dependent and a signal is produced based on the interaction of light photons with the electrons in the active layer of the detector.

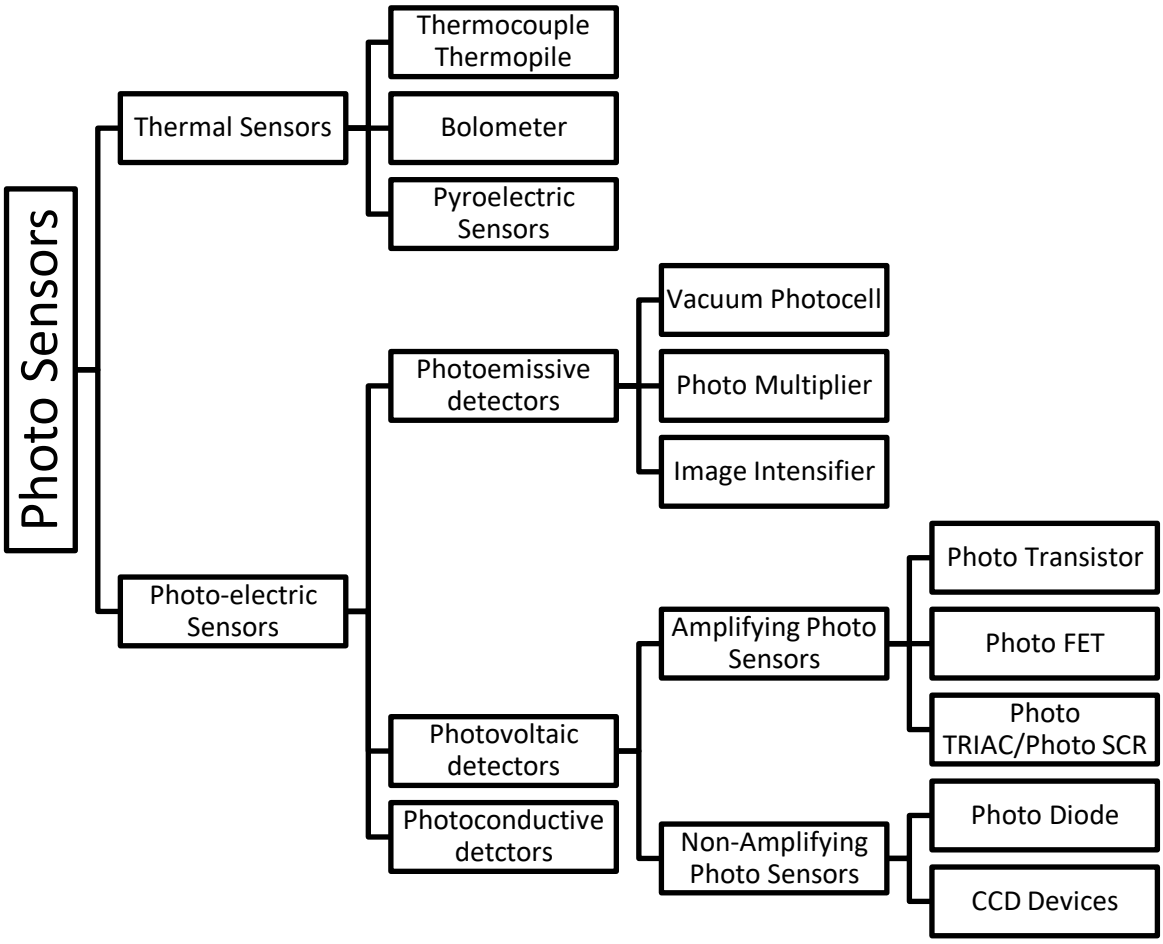

Figure 2-1: Types of Photodetectors.

Photo-electric sensors can be further sub-divided into three main types of detectors, i.e. photoemissive, photovoltaic and photoconductive devices. The photoemissive detectors rely on external photoeffect and eject electrons from the photocathode's surface by absorbing photons with energy that is higher than the work function of the cathode material. When the photocathode is placed in a vacuum system, the ejected electrons can be collected at the anode. This concept can be used in the photomultiplier tubes (PMTs), where the photoelectrons can be accelerated several times towards consecutive dynodes, each time emitting subsequent electrons and thus amplifying the signal to a value that can

be easily measured at the anode. Such detectors were initially used commonly for ultraviolet measurements. However, several disadvantages such as being bulky, fragile and needing high operating voltages exclude these devices from many advanced applications.

The other two types are based on semiconductor materials and rely on the internal photoemission effect proposed by Einstein's theory of photoelectric effect and Planck's quantum theory of radiation [15, 16]. The semiconductor material, which forms the basis of such photodetection devices, can either be organic or non-organic.

2.1.1 Inorganic semiconductor materials:

In case of inorganic semiconductor photodetectors, the covalent periodic structure results in set levels of band energy i.e. conduction band and valence band. Photons of light generated from an optical source get absorbed upon interaction with the semiconductor material. In case, the absorbed photons are having energy greater than the energy bandgap between the valence band and conduction band, an electron-hole (e-h) pair is generated. The photo-excited charge carriers (electrons and holes) can move freely within the premises of the semiconductor material. Under the effect of (external) electric field the e-h pairs can be separated and gathered at the contacts as the external photocurrent proportional to the number of absorbed photons.

The inorganic semiconductor photodetection can be elemental, binary compound or oxide based. Some of the inorganic semiconductor materials used in the construction of the active layer are mentioned below [17]:

- Silicon (Si) having a bandgap of 1.1 eV and a wavelength sensitivity of 190 nm to 1100 nm.
- Indium gallium arsenide (InGaAs) having a bandgap of about 0.75 eV and a wavelength sensitivity of 800 nm to 2600 nm.
- Indium phosphide (InP) having a bandgap of about 1.35 eV.
- Indium aluminium arsenide (InAlAs) having a bandgap 0.51 eV [18].

2.1.2 Types of inorganic semiconductor based photodetectors:

The inorganic semiconductor based detectors can be fabricated in a variety of configurations, each serving a specific purpose. These photodetectors can be intrinsic as well as extrinsic in nature. Some of the configurations are discussed below.

2.1.2.1 Photoconductors/photoresistors:

A change in resistance occurs in numerous materials upon their exposure to light and thus are named as light dependent resistors (LDRs). Examples of LDR materials include Cadmium sulphide (CdS) and Cadmium selenide (CdSe) [6]. A typical photoconduction sensor has a dark resistance of around 10 MΩ. The decrease in the resistance is dependent on illumination level and generally has a value of 2.4 kΩ at 50 lux and 130 Ω at 1000 lux [6]. Nevertheless, variations in the resistance with respect to illumination do not show a linear trend and require an additional linearization circuit. The photoconductors have a fairly slow response towards illumination and require a few

seconds to demonstrate any changes in the resistance, thus rendering these sensors unsuitable for applications requiring fast response.

2.1.2.1.1 Phototransistors:

Phototransistors have a three terminal configuration similar to organic field-effect transistor (OFETs), with three electrodes referred to as collector, emitter and base [19]. The base-emitter junction which is sealed in a transparent package gets affected by incident light and thus acts as a diode [20]. Upon exposure to light, the base-emitter junction promotes electrons from valence band to conduction band. For the provision of much larger collector current, amplification of current takes place by normal transistor action. The spectral response of phototransistor is limited to red and infra-red portions of the light spectrum, and adjustments can be made by tuning the base voltage. In addition, the response is generally slow when comparing with photodiode. These sensors are manufactured in the form of integrated circuits (ICs) with integrated amplifiers and other processing circuitry.

2.1.2.1.2 Photodiodes:

It is a PN junction, which is designed such that the light falling on it may enter into the charge-depleted region of the junction. When diode is in dark, a small current referred as reverse saturation current or leakage current flows in its external circuit. This current is due to the drifting of e-h pairs, which are thermally generated in the charge-depleted region. This leakage current increases with the rise in temperature [17]. It also increases along with

the level of illumination because more intense light would produce more number of e-h pairs due to increased number of photons. The photodiode quickly responds to light without any delay and is used for detection of visible and invisible optical signals in various applications including optical communication, optical switching and character recognitions.

The photodiode can be operated in two modes 1) Photovoltaic mode, 2) Photoconductive mode [21]. In case of photovoltaic mode the photodiode generates a voltage upon illumination. However, the dependence of voltage on the illuminated light is nonlinear and the dynamic range is quite small. Further, maximum speed is also not achieved. On the other hand, in case of photoconductive mode the photo-generated current response is fairly linear with respect to changes in illumination, and thus is the adopted mode of operation for photodetection purposes. Additional circuitry might be added to linearize the behaviour and amplifying the generated signal. The response of these sensors is fairly short typically around 250 ns and is suitable to be used in modulated light beam applications [20].

The photodiodes can further be subcategorized into four major types i.e. P-N photodiode, positive-intrinsic-negative (PIN) photodiodes, Schottky photodiodes and avalanche photodiodes, Figure 2-2 [20].

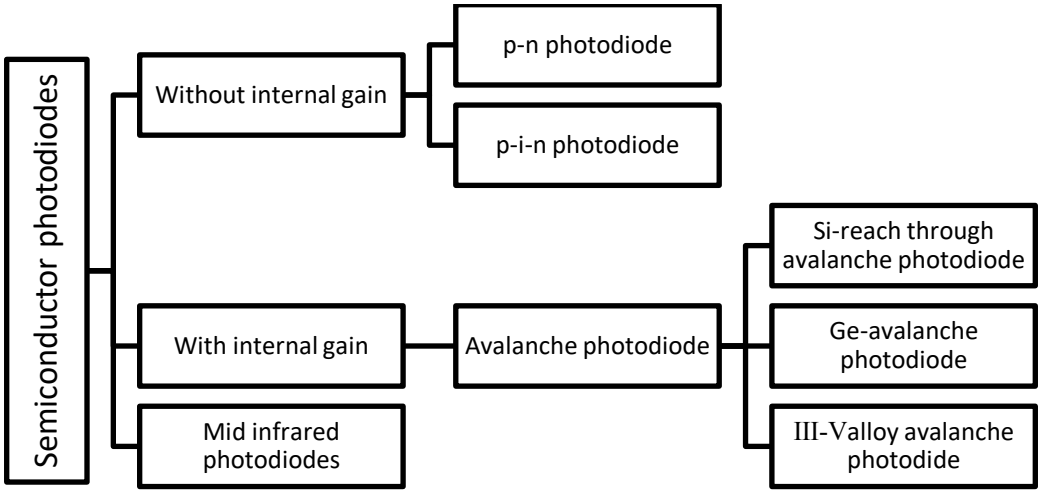

Figure 2-2: Types of semiconductor photodiodes.

The simplest kind of photodetector is an unbiased p-n junction. When photons of light are incident upon the depletion region an e-h pair is created. The electrons and holes generated move in opposite direction under the influence of electric field, thus driving current through the device. When operated in reverse biased condition, this process accelerates and the p and n regions collect majority of charge carriers, resulting in a potential difference across the external load that is proportional to the intensity of the optical radiation falling on the device. It is important to note that the width of the depletion region should neither be too wide nor too narrow for an optimized performance of the P-N junction.

In case of PIN photodiodes, an additional high-resistance layer is added between the P and N regions of the device that offers the functionality of controlling the width of the depletion layer [13]. This in-turn results in the reduction of transit or diffusion time of

the photo-generated e-h pairs, thereby improving the response time. These types of photodiodes have low capacitance thereby presenting high bandwidth and making them appropriate for applications related to high-speed photometry and optical communication [13].

Schottky photodiodes are complex devices requiring rectifying (Schottky-type) and non-rectifying (ohmic-type) contacts [14]. High quantum efficiency, high response speed, low dark current, high ultraviolet (UV)/visible contrast, and possible zero-bias operation, are some of the advantages associated with Schottky photodiode [22]. Schottky photodiodes mainly comprise of a metal layer that is in contact with a semiconductor. The metal/semiconductor junction exhibits rectifying behaviour, arising from the electrostatic barrier present between the metal and the semiconductor. This barrier is formed due to the difference in work function of the metal (Φ_m) and semiconductor (Φ_s). It should be noted that in case of connection with an n-type material the metal should have a work function greater than that of the semiconductor.

When considering avalanche photodiodes, these devices are more sophisticated than the PIN photodiodes and are used to form a high field region ($\sim 3 \times 10^5$ V m^{-1}) where the electrons and holes can acquire enough energy to generate new e-h pairs [17]. This phenomenon is called impact ionization and leads to avalanche breakdown in an ordinary reverse biased diode. A high reverse biased voltage (typical range: 50-400 V) is required to create new carriers by impact ionization [17]. Following careful device fabrication and processing procedures, one can obtain a large carrier multiplication factor. In case of defect-free material, that ensures the uniformity of carrier multiplication over the entire area of the device, a multiplication factor as high as 104 can be achieved.

2.1.3 Organic semiconductor materials:

Organic semiconductors have emerged as appealing materials for several applications since their optoelectronic properties can be chemically tailored and can be deposited by means of cost effective printing methods [23]. Photodetectors based on organic semiconductors tend to have a spectral sensitivity spanning from UV to near-infrared (NIR) and can be made panchromatic or be selectively tuned to be responsive to specific wavelengths [19]. In addition, the sensitivity of the detector can be expanded to higher energy radiation levels (i.e. X-ray and γ rays) using direct or indirect sensing schemes. Organic semiconductors offer temperature processability over large areas (on virtually every substrate) and the possibility of integrating into various devices including diodes, transistors, photovoltaic cells, memories and sensors. Further, they can be fabricated into comfortable geometries ready to be integrated into various (infrastructure building and clothing industry related) technologies, where it is difficult to integrate silicon-based photodetectors. The combination of large area fabrication and conformity may also enable the use of organic semiconductors in medical applications, requiring simultaneous tomography and adaptive detection arrangements.

Organic semiconductors are classified as single small molecules, oligomers and conjugated polymers. The intermolecular bonds present in the solid state molecules have a relatively low energy, giving rise to less ordered structure, due to the low enthalpy gain. When it comes to processing, this aspect is advantageous since the required thermal budget becomes low. In addition, it allows the functionalization of semiconductors for their improved solubility in proper solvents, enabling the implementation of solution-based

deposition protocols and thus paving the way towards high throughput, low-cost device fabrication techniques. Due to the limited scope of the underlined thesis, only theory background related to conducting conjugated polymers and their application in photodetection would be covered.

2.1.3.1 Conducting polymers:

In Greek terminology, 'poly' stands for 'many' and 'meros' stands for 'parts', thus polymers are huge chains or sometimes 3D networks of repeating organic units called monomers. Since monomers are the basic unit of construction, therefore the characteristics of a polymer are strongly dependent on it. The polymer made up of single monomer is referred as homopolymer, whereas on the other hand if a polymer consists of two or more monomers, it is called copolymer. Copolymers can further be classified into alternating copolymers, random copolymers, periodic copolymers, block copolymers and statistical copolymers.

The polymers are generally referred to as non-conducting plastics and thus owing to their insulating properties are used extensively in electrical, electronics and packing industry [24]. However, when considering conjugate polymers, they differ from everyday polymers since they intrinsically conduct electricity and the credit goes to three scientists, A.J. Heeger, A.G. MacDiarmid and H. Shirakawa for the contribution in their discovery and development [25]. These polymers are generally composed of (carbon, hydrogen, sulphur, nitrogen based) macromolecules and contain π-conjunction, with delocalized π-electrons along the main chain of the polymer [26]. Polyacetylene can be regarded as the

simplest example of a π-conjugated polymer, having alternating single and double bonds in its linear hydrocarbon chain [27, 28]. Other examples include Poly(3-hexylthiophene-2,5-diyl) regioregular (P3HT) and Poly(p-phenylene vinylene) (PPV). Since the energy bandgap of such conducting polymers is around 1 eV, therefore they can be classified as semiconductors.

The inherent conductivity of conjugated polymers gets created as a result of the formation of various redox states (upon oxidation or reduction of the conjugated backbone), in association with the formation of polarons (radical cations) and bipolarons [29, 30]. The conductivity of the polymer increases alongside the dopant level, due to the increase in the number of mobile charge carriers [31]. However, environmental stability, thermodynamic stability and effectiveness of dopant ionization are the main issues related to the dopants. With the above mentioned issues taken into consideration, the maximum level of doping is limited and depends on the polymer and the dopant itself. In case of Polypyrrole (PPy), the dopant level ranges from 20% to 50%.

One of the most adopted molecularly doped (fullerene) polymer with high stability and good conductivity is poly(3,4-ethylendioxythiophene) polystyrene sulfonate (PEDOT:PSS), in which PEDOT is p-doped by sulfonyl groups carried by PSS. It consists of 60 carbon atoms arranged as 20 hexagons and 12 pentagons. Although it is a poor light absorber with the optical gap in the range of 1.5 eV to 1.8 eV, it is an excellent electron acceptor with high charge carrier mobility within the range of 2.0 to 4.9 $cm^2 V^{-1} s^{-1}$ [32].

2.1.3.1.1 Band gap and excitation:

The reason behind the absorption of light, by the conjugated polymers is because of the altering single and double bonds present in the backbone of the conjugated polymer. When considering polyacetylene, the backbone consists of carbon atoms (having four electrons in the valence band), where three electrons form three sp^2 bonds (i.e. one with hydrogen and the other two with neighbouring carbon atoms) as shown in Figure 2-3.

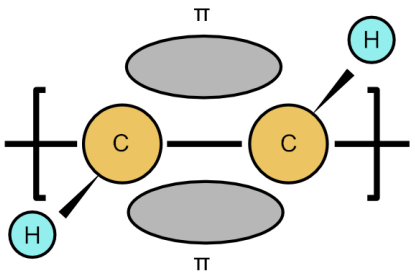

Figure 2-3: Polyacetylene molecular structure.

All three of these bonds (having σ-bond character) are present in the centre of the two nuclei. The remaining electron (present in the p-orbital) interacts with another (p-orbital) electron, thus forming the π-bonding highest occupied molecular orbital (HOMO) and empty π*-anti-bonding lowest unoccupied molecular orbital (LUMO). The bandgap between the HOMO and LUMO is decided by the difference in the energy levels between these two orbitals. Since the π-bonds are not located within the molecular plane and less bound to the carbon nuclei, therefore the energy for the photoexcitation is relatively

reduced. When a photon of light (having an energy equal or greater than the energy bandgap) is absorbed by the π-bonded electron, it gets photoexcited from the valence (HOMO) band to conduction (LUMO) band, with the polymer maintaining the structural integrity via σ-bonds.

2.1.3.2 Charge generation in organic semiconductors:

In contrast to the inorganic semiconductor based devices, there exists a high coulomb attraction between the electron and hole, owing to the low dielectric constant (ε ~ 3-4). Hence the e-h pair remains in its bound state (called exciton), with distorted molecular geometry. This pair diffuses through the material covering a distance of approximately 5-15 nm, before radiatively or nonradiatively decaying back to the ground state level [33, 34]. For the enhancement of the excitons separation process, Tang et al proposed the combination of phthalocyanine dye (as a donor material) with perylene tetracarboxylic derivative (as a p-type material) [35]. This donor-acceptor combination due to the relative alignment of donor and acceptor energy levels, induces excitons separation. Upon the arrival of electron at the donor-acceptor interface, the electron located in the lowest unoccupied molecular orbital (LUMO) orbital of the donor material would get transferred to the LUMO orbital, situated at a relatively lower energy level. In case of holes transportation, the whole process occurs in the opposite direction, Figure 2-4. The generated freely-moving charge carriers later get transported to their respective electrodes via donor and acceptor phases. It is worthy to note that the exact driving force for the excitons generation in still debatable, but it is confirmed that a larger difference in the

energy of the LUMO orbitals of the donor and acceptor will result in higher number of charge carriers [36, 37]. However, this will also result in a greater loss of energy and limited device performance. Nevertheless, exceptions have been reported where the small difference between the LUMO levels still efficiently generates charge carriers.

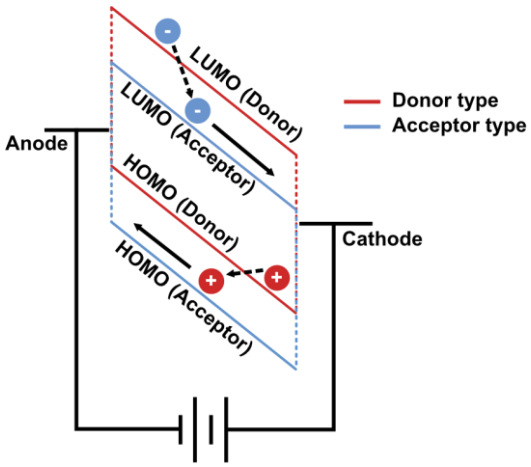

Figure 2-4: Band diagram representation of BHJ based photodetector.

2.1.3.3 Organic photodetector configurations:

In case of organic photodetectors, there are mainly two types of configurations i.e. planar and bulk heterojunction (BHJ). In case of planar heterojunction, an organic film is formed by super-positioning an acceptor material on the top of donor layer. Since, the excitons need to travel up to donor-acceptor interface to dissociate, therefore restrictions are placed on the thickness of the planar structure that should lie within the diffusion length range (≈ 10 nm) to prevent recombination, before the dissociation of excitons takes place. This restriction of thickness of active layer would result in the loss of absorption. Lastly,

the heterojunction formed will have limited contact, resulting in the waste of photon energy and a comparatively low responsivity of photodiodes (PDs).

Optimal structure is attained when the junction area gets increased while keeping the thickness at an adequate level, for maximum absorption of light. This is the case of bulk heterojunction, where a 3D nanoscale phase separation of donor and acceptor materials exist and effective distribution of the heterojunction takes place, throughout the bulk of the active layer. It is of key importance to control the morphology of the deposited layer so that numerous percolated paths are available throughout the bulk materials for the effective transportation of electrons and holes (to their respective electrode) and minimization of recombination. To achieve that, donor and acceptor materials can be mixed in a common solvent, thus forming an active layer from the solution mixture [38]. This also allows the utilization of simple deposition processes like spin coating.

Successful integration of P3HT:PCBM BHJ active layer with thin-film transistor (TFT) backplane in an image sensor has been achieved. Another successful material combination consists of electron-accepting poly(9,9′-dioctylfluorene-co-benzothiadiazole) (F8BT) and the electron donor Poly (9,9′-dioctylfluorene-co-bis-N,N′-(4-butylphenyl)-bis-N,N′-phenyl-1,4-phenylenediamine) (PFB), which has shown good ambient environment stability as well as good ink-jetting behaviour. Smooth thin films having a thickness of ~ 0.8 – 1.0 μm and area of 35 mm^2 have been achieved for printed high concentration PFB:F8BT blends, mixed in 1:1 weight ratio.

Apart from BHJ structure, tandem architecture photovoltaics has attracted a lot of attention. A typical organic tandem cell comprises of a bottom cell and a top cell connected

in series, using an interlayer. The purpose of this configuration is to cover a broad photon spectrum, by means of exploiting the light (that is not utilized by the first device); by using a second device. This concept is also applicable for polymer PDs and single compact device comprising of several single-junction cells (having separate optical detection sub-bands) can be made. Tandem organic PDs based on small molecules have been reported by Matthew Menke et al for efficient broad detection from 300 to 1100 nm [39].

Another approach to fabricate photodetectors is based on dye-sensitized photovoltaic detectors, consisting of a TiO_2 semiconductor layer sensitized using various anionic dyes for the absorption of light over a wide wavelength range [40]. The interface between the dye and nanoporous TiO_2 acts as a heterojunction, with excited electrons (generated via absorption of photon by the dye) being extracted through TiO_2 and holes being transported by a layer of electrolyte. Study done by Jayaweera et al, utilized a dye-sensitized TiO_2 (nanoparticles) semiconductor layer [40]. The TiO_2 nanoparticles allowed for an increase in surface area, which thereby resulted in increased external quantum efficiency. Upon illumination the electrons (generated by means of dye excitation) were transported via TiO_2 semiconductor layer, while the holes were transported using Copper(I) thiocyanate (CuSCN) overlayer. The sensitivity and responsivity of the fabricated device turned out to be equal to 950 nm and 2 mA W^{-1}, respectively. The detectivity (D^*) was reported to be around 10^{10} Jones. The dye-sensitized device structure is discussed in detail, in the later sections related to its application as a solar cell.

2.1.4 Figures of merit:

Several photodetection parameters are commonly used to define the performance characteristics of a photo-detector and determine their suitability for a specific application. These parameters can be considered as the figures of a photodetector. They are used for comparing one photodetector to another and determining the suitability of the photodetector, for a particular application. Some of the key parameters that help in the performance characterization are mentioned below:

2.1.4.1 Current voltage characteristics:

In order to model the current in donor-acceptor organic devices a modified version of the Shockley diode equation for series and shunt resistance can be used, Eq. 2.1 [29], [30].

$$I = \frac{R_{sh}}{R_s + R_{sh}} \left\{ I_o \left[exp\left(\frac{q(V - IR_s)}{nkT} \right) - 1 \right] + \frac{V}{R_{sh}} \right\} \qquad \ldots\ldots\ldots\ldots\ldots\ldots (2.1)$$

Where I is the current, R_s is the series resistance, R_{sh} is the shunt resistance, I_o is the dark saturation current, n is the ideality factor and V is the applied bias voltage.

When plotted, Eq. 2.1 reveals the characteristic *I-V* curve obtained in dark and light conditions as depicted in Figure 2-5. In case when the applied voltage is greater than zero, an exponential increase in the current can be noted since the polarity conditions of the electrode favour the generation of photocurrent, as the anode becomes more positive, whereas the cathode becomes more negative. In contrast, under reverse biased conditions (where the bias voltage is less than zero because of the opposite polarity) anode becomes

negatively charged whereas the cathode becomes positively charged, thus creating an energy barrier between the electrodes and organic film and halting the transportation of electrons.

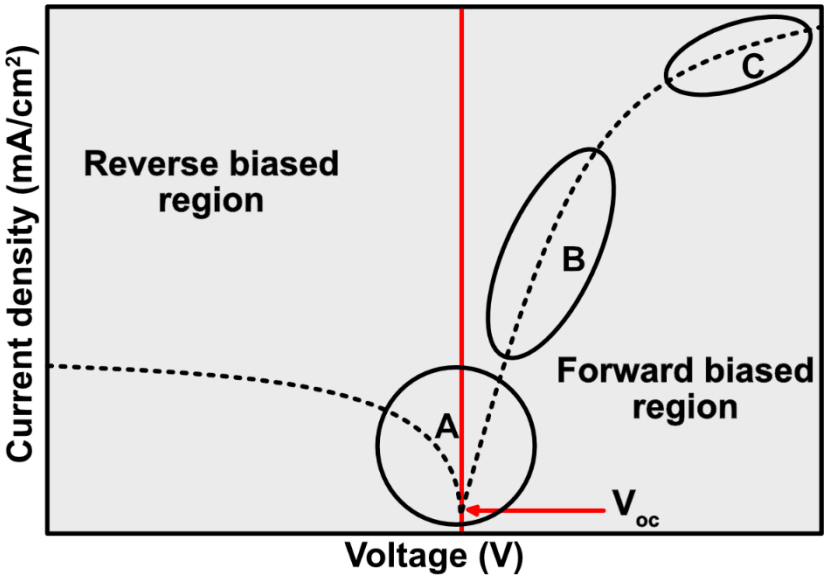

Figure 2-5: J_{dark} vs Voltage in logarithmic scale.

The forward biased characteristic J-V curve has three distinct regions, namely:

A: A linear regime at negative and low positive voltage levels, where the current produced is limited mainly by the shunt resistance.

B: An exponential region occurring at intermediate voltage levels where the diode controls the flow of the current.

C: A second linear region occurring at high voltage levels, where the current is limited by the series resistance of the diode.

2.1.4.2 Dark current:

An organic photodiode is generally operated in the reverse biased conditions, in which only a minute current (known as dark current) flows through the diode in the absence of light. Under light conditions, the electric field influences the photo-generated excitons to move towards their respective electrodes.

In an ideal case, the dark current should be equal to zero. However, there is a negligible amount of dark current flowing due to the carrier recombination at the donor/acceptor interface caused either by diffusion of excitons across the barrier or by the recombination of e-h pairs.

2.1.4.3 Signal to noise ratio and noise equivalent power:

The device experiences fluctuation in voltage/current at the output terminals, even without an input optical signal. Signal-to-noise (*S/N*) is the ratio of signal power ($P_{optical}$) from photocurrent to the photodetector noise power. In other terms, it establishes a comparison between the level of signal and the level of background noise. Higher values of *S/N* mean that there is less interference and the actual signal is strong as compared to the interfering background noise. Eq. 2.2 can express it as follows:

$$\frac{S}{N} = \frac{I_{photo}}{i_{noise}} = \frac{P_{optical}\,(\lambda/_{hc})q\eta}{i_{noise}} \qquad \ldots\ldots\ldots\ldots\ldots\ldots (2.2)$$

Noise equivalent power is the RMS value of the sinusoidally modulated optical radiation at 400 Hz with a reference bandwidth of 1 Hz, which produces this equivalent output electrical signal, Eq. 2.3.

$$NEP = \frac{hc.I_{photo}}{q\eta\lambda} \qquad \ldots\ldots\ldots\ldots\ldots\ldots (2.3)$$

2.1.4.4 Responsivity:

Responsivity ® is a measure of the change in detector current arising from the optical signal. It can be expressed as a ratio of average photocurrent (I_{photo}) produced to the averaged incident radiation causing it, Eq. 2.4. It is conventionally expressed in A W^{-1}. It is desirable to get a higher responsivity value in order to maximize signal to noise ratio (S/N).

$$R = \frac{I_{photo}}{P_{optical}} \qquad \ldots\ldots\ldots\ldots\ldots\ldots (2.4)$$

2.1.4.5 Impulse response:

In ideal case, a photodetector should not take time to respond to the absence and presence of light. However, due to capacitive effects of a photodetector, the device will have a certain fall and rise time associated with the electrical output, when a perfect optical pulse with zero rise-time and fall time descends upon the device. It is preferred to have an impulse response time as short as possible.

2.1.4.6 Detectivity:

The detectivity (*D*) is the reciprocal of NEP Eq. 2.5.

$$D = \frac{1}{NEP} \qquad \text{..... (2.5)}$$

A more useful merit is the specific detectivity (D^*), which does not have a dependence on the active area of the device (A_d) and the bandwidth (Δf). Eq. 2.6 can express it.

$$D^* = D \cdot \sqrt{A_d \Delta_f} = \frac{\sqrt{A_d \Delta f}}{NEP} \qquad \text{..... (2.6)}$$

2.1.4.7 Quantum efficiency:

Quantum efficiency is defined as the electrical sensitivity of a photosensor towards light. It is measured over a range of wavelengths in order to find out the efficiencies at different photon energy levels. It can be divided into two main types i.e. internal (*IQE*) and external quantum efficiency (*EQE*).

EQE is the ratio of number of charge carriers collected to the number of photons incident upon a devices and is thus dependent on wavelength of incident photon, Eq. 2.7 [41].

$$EQE(\lambda) = \frac{I_{ph}}{P} . \frac{hc}{q\lambda} \qquad \text{..... (2.7)}$$

Where I_{ph} is the photocurrent produced, P is the incident light power, h is the Planck's constant, c is the speed of light, q is the elementary charge and λ the wavelength.

In case of *IQE,* only the photons that actually get absorbed are only considered and is thus defined as the ratio of carrier generation rate to the number of photons (of a given energy) absorbed by the device Eq. 2.8.

$$IQE(\lambda) = \frac{EQE(\lambda)}{A} = \frac{EQE(\lambda)}{1 - r(\lambda) - T(\lambda)} \qquad \text{..... (2.8)}$$

Were $A(\lambda)$, $r(\lambda)$, and $T(\lambda)$ are absorbance, reflectance and transmittance, respectively.

2.1.4.8 Spectral response:

It provides a measure of the output response of a photodetection devices over a range of wavelengths [42]. It is conceptually similar to quantum efficiency and is expressed by Eq. 2.9.

$$SR = \frac{q(\lambda)}{hc} QE \qquad \text{..... (2.9)}$$

Where *QE* is quantum efficiency.

2.2 Dye-Sensitized Solar Cells:

Dye-sensitized solar cells (DSSCs) are electrochemical cells that present various advantages over the conventional silicon based solar cells, since they are low in toxicity, exhibit excellent stability and have a good power conversion efficiency [43]. In addition they are simple to fabricate, and architecturally and environmentally compatible [44].

The first successful DSSC fabrication was carried out by O'Regan and Grätzel, in year 1991. It was reported to absorb visible light till 800 nm and had a power conversion efficiency of 7% [45]. After a period of two decades, in 2011 this efficiency increased to 11.4 %, with the help of nanostructured semiconductor electrodes [43, 46-48]. Lately, an increased efficiency of 13% has been reported for DSSC fabricated using a mesoporous semiconductor electrode and porphyrin sensitizers [49]. Since then, extensive research has been carried out for the explanation of various working principles, improvement in conversion efficiency and up scaling the technology to a commercial level. The commercial cost of DSSC fabrication is likely to be low, since the cost associated with the components, materials and fabrication processes pursued is quite low [50].

The upcoming sections present a well-rounded discussion related to DSSCs. The components and the processes involved in the fabrication of DSSCs will also be discussed. Later, a description about the working principles and characteristics of DSSCs will be provided.

2.2.1 Components and working principal:

A DSSC is a photo-electrochemical system consisting of TiO_2 nanoparticles, dye-sensitizer, electrolyte and catalyst coated back contact as illustrated in Figure 2-6.

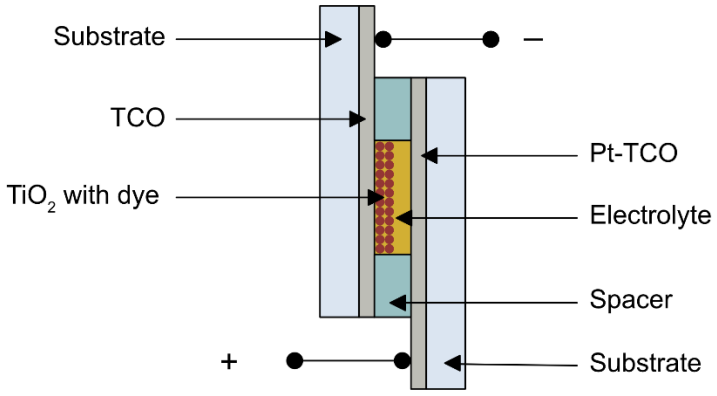

Figure 2-6: Typical DSSC configuration.

When a photon of light having an energy equal or greater than the bandgap between the highest occupied molecular orbital (HOMO) and lowest unoccupied molecular orbital (LUMO) levels is absorbed by a dye molecule, an electron gets relocated from ground state D (HOMO) to an excited state referred as D^* (LUMO), given by Eq. 2.9 [51]. The electron in the excited stated is then transferred to the conduction band (CB) of the TiO_2, provided that the D^* state lies at a higher energy level as compared to the CB of TiO_2. After the donation of electron the photosensitizer molecule gets converted into a positively charged entity D^+ through Eq. 2.10. The electron transferred to the TiO_2 later moves to the transparent conducting oxide (TCO) based back contact by diffusing through the cross-section of semiconductor layer. The electrons reaching the TCO layer are transported to

the counter-electrode after passing through the external circuit and performing useful work. Later, the electrons at the counter-electrode are collected by one of the ion species (transforming it into the other species) through Eq. 2.11. In the end, the electron is transported to the HOMO level of the dye, thereby regenerating it and conserving the whole system as represented by Eq. 2.12. The energy band diagram for DSSC is presented in Figure 2-7.

$$D_{(absorbed)} + hv \rightarrow D^{*}_{(absorbed)} \quad \ldots\ldots\ldots\ldots\ldots\ldots (2.9)$$

$$D^{*}_{(absorbed)} \rightarrow D^{+}_{(absorbed)} + e^{-}_{(injected)} \quad \ldots\ldots\ldots\ldots\ldots\ldots (2.10)$$

$$I_3^- + 2e^-_{(cathode)} \rightarrow 3I^- \quad \ldots\ldots\ldots\ldots\ldots\ldots (2.11)$$

$$D^{*}_{(absorbed)} + \frac{3}{2} I^- \rightarrow D_{(absorbed)} + \frac{1}{2} I_3^- \quad \ldots\ldots\ldots\ldots\ldots\ldots (2.12)$$

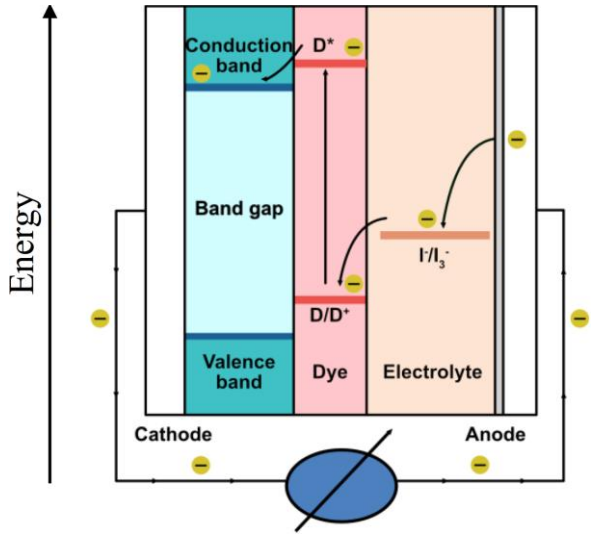

Figure 2-7: Generic energy band diagram for DSSC.

It is important to note that the open-circuit voltage (V_{oc}), measured between the photo-anode and counter-electrode, is determined by the difference between the Fermi level of TiO_2 and the redox potential of the electrolyte utilized [52]. However, the V_{oc} measured experimentally is generally less than the energy difference between the redox potential of the electrolyte and the Fermi level of the TiO_2, due to the contest between the electron transfer and recombination paths [53].

Between the counter-electrode and dye-sensitized semiconductor layer lies an electrolyte layer that typically contains ionized entities that can conduct electricity. The major role of electrolyte is to neutralize the positively charged oxidized dye molecule by means of an electron transfer carried by a negatively charge ion species. The DSSC also requires a catalyst-coated back-contact to facilitate the reactions taking place. Consequently, the performance of a DSSC depends on the HOMO and LUMO levels of the dye material, the fermi level of the TiO_2 nanoparticles and the redox potential of the electrolyte ion-species. The state-of-the-art efficiency of dye-sensitized PV device on lab-scale is currently 15% achieved at École polytechnique fédérale de Lausanne (EPFL) in Switzerland [54].

2.2.2 Components for the fabrication of DSSCs:

The fabrication of DSSC starts with the deposition of the TiO_2 semiconductor layer using various methods i.e. doctor blade, sol-gel, screen-printing, chemical vapour deposition, electrostatic spraying and electrophoretic deposition [55]. Later, the deposited TiO_2 layer is dried and sintered, to improve the conductivity of the semiconductor layer.

The sintered photo-anode is then sensitized using a high light absorbing dye. The dye-sensitized photo-anode are later dried and attached with a platinum based counter-electrode, with a sealant sandwiched between them. Electrolyte is poured in through a drilled hole, which is sealed on afterwards. The components used in the fabrication of DSSC are discussed below.

2.2.2.1 Photo-sensitizer:

An ideal sensitizer should be having several qualities including [56]:

1. The sensitizer should absorb all photons below the near-IR wavelength i.e. 920 nm.
2. It must contain group (like carboxylate and phosphorous) for anchoring onto semiconductor oxide's surface.
3. For the minimization of energy losses incurred during the electron transfer phase, it is important that the LUMO of dye molecule should be slightly above the conduction band of the semiconductor.
4. The HOMO of the dye molecule should be low enough to accept an electron from the ion species present in the electrolyte.
5. It should be stable enough to last for 20 years and should not present any degradation.

The photo-sensitizers can be classified into various groups, as mentioned in the upcoming sections:

2.2.2.1.1 Natural dye-sensitizers:

Dye obtained from natural resources (i.e. fruits, flowers and leaves) offer suitable alternative to high cost inorganic dyes. In addition they are extracted using simple procedures and are environment friendly. These dyes have colours ranging from red to purple and can be divided into four different pigment groups i.e. Carotenoids, Chlorophyll, Flavonoids and Betalains. [57].

Carotenoids are organic pigments, having a large family of isoprenoids, with over 600 members. They are found in chloroplasts and chromoplasts of plants and provide many distinctive red, orange and yellow colours to many fruits and flowers [57]. In addition, carotenoids are also found in some organisms including fungi and bacteria that depend on the photosynthesis process, with the function of light energy absorption and protection of chlorophyll from photo-damage [58]. When it comes to the molecular structure all carotenoids are tetraterpenoids, thus exhibiting a distinctive C_{40} hydrocarbon backbone (forming 8 isoprene molecules) that induces structural and oxygenic modifications. They have a very short light absorption ranging i.e. from 400-550 nm.

Chlorophyll is a natural photosynthesis pigment found in plants and gives them the distinctive green colour. Some of the primary functions of chlorophyll include: efficient harvesting of light energy and its transduction for photosynthesis process [59]. It has two main types i.e. chlorophyll ‘a’ and chlorophyll ‘b’, with the derivate of chlorophyll ‘a’ (methyl trans-32-carboxy-pyropheo-phorbide) being the most efficient one [60]. The chlorophylls are used in DSSC since they have a high absorbance in red and blue regions of the visible spectrum. When establishing a comparison between chlorophyll ‘a’ and

chlorophyll ‘b’ in terms of absorbance spectrum, the chlorophyll ‘b’ has a characteristic blue tinge and exhibits a red shift in comparison to chlorophyll ‘a’ [61].

Flavonoids are widely distributed plant pigments that are commonly used to define large group of natural products containing C_6-C_3-C_6 skeleton and having phenylbenzopyran functionality. The have two benzene rings that are joined by a γ-ring, thereby distinguishing one flavonoid compound from another [62]. These pigments are further categorized into various categories anthocyanins, flavones, flavonolsm, proanthocyanidins etc. Anthocyanins are red pigments found in berries and many other fruits. Flavonols are the monomers of quercetin present in onions as well as tomatoes. In case of flavanols, they are monomers of catechin which is abundantly present in tea, cocoa and apples. Proanthocyanidins are the oligomers of flavanols, similar to catechin/epicatechin present in cocoa, tea, apples and peanuts. Isoflavones are abundantly present in the soybeans. Not all flavonoids demonstrate the capability of absorbing visible light, even when having similar structures. The ones having the capability of absorbing have a lower bandgap between the HOMO and LUMO levels, allowing the excitation of electrons even when a low energy photon is absorbed and eventually leading to a broad absorption in the visible region [63]. Flavonoids get readily absorbed onto the TiO_2 surface through the displacement of hydroxide (OH^-) counter ion from the Ti(IV) site, that combines with a proton donated by the flavonoid [63, 64].

The low efficiencies of natural dye based DSSCs are mainly due to the weak interaction between the dye molecules and TiO_2. The aggregation of dye on the nano-crystalline film is another reason for low efficiency.

One of the ways to broaden the optical absorption in the visible and IR region is to employ a combination of different dyes having absorption peaks at different wavelengths [65]

2.2.2.1.2 Metal complex sensitizers:

Metal complex sensitizers have both types of ligands i.e. anchoring ligands (ACLs) and ancillary ligands (ALL). The adhesion to the semiconductor depends on the properties of the ACLs [66]. On the other hand, ACLs can be used to tune the overall properties of the dye. Modifications to ACLs and ALL can affect the properties of metal to ligand charge transfer (MLCT).

Metal complex sensitizers mainly consist of ruthenium (Ru), iron (Fe), platinum (Pt), osmium (Os) and rhenium (Re) complexes [67]. DSSCs based on square-planar Pt complexes are reported to have an efficiency of 3% at AM 1.5 irradiance [68]. Os-complexes have a wide photo-response with a spectral absorbance ranging from 400 nm to 1100 nm, *IPCE* of 65% and a J_{sc} of 18.5 mA cm^{-2} under AM 1.5 irradiance. However, none of the metal complexes have efficiency greater than the one demonstrated by Ru-complex. The reason behind the superior Ru performance is that HOMO and LUMO levels are better matched with the iodine redox potential and conduction band level of TiO_2 electrode, respectively [69].

2.2.2.1.3 Metal-free photosensitizers:

Metal-free photosensitizers have been investigated to replace Ru-based sensitizers and improve the electrical characteristics of associated DSSCs. It is of key importance to have proper dye selection or to have the designing components finely tuned for an increased efficiency. A general design mechanism of dye is shown in Figure 2-8, with the substituent acting as donor and acceptor separated by the π-conjugated-spacer [66].

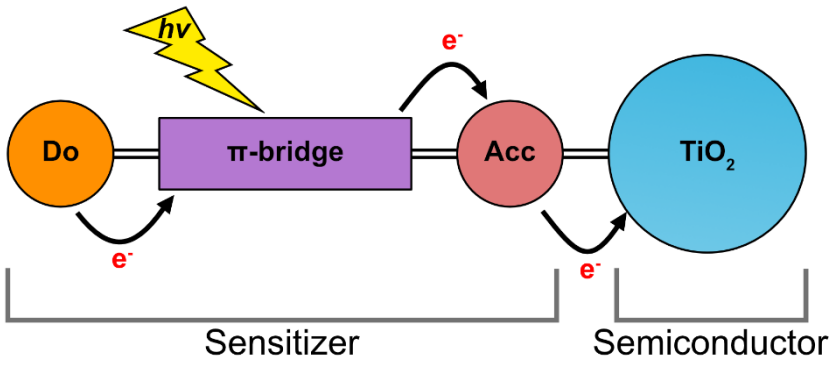

Figure 2-8: Design mechanism for the use of a TiO_2 bonded organic dye.

Tuning of the photoelectric properties can be done by means of altering or matching different substituents present within donor-π-acceptor (D-π-A) structure. The efficiency of metal-free dyes is dependent on the chemistry of the electrolyte being used. Efficiencies of 8%, 6% and 4% have been achieved for metal-free photosensitized DSSC containing liquid, ionic and solid-state electrolytes, respectively [70]. For efficient sensitizer, the selection of the donor groups should be made from the rich aryl amines family i.e.

phenylamine, aminocumarin, indoline and (difluorenyl)triphenylamine. Further, the π-conjugated connector should belong to the compounds containing thiophene units (e.g. oligothiophenes, thienylenevinylenes, or dithienothiophene), since they exhibit superior charge transportation characteristics. When considering acceptor moiety, Acrylic acid group is considered to be the best. The efficiency of metal-free sensitizers is lower than that of Ru-based and is considered unsuitable for industrial applications.

2.2.2.2 Transparent conducting substrate:

In order to be suitable for incorporation within DSSCs, a substrate should exhibit a low sheet resistance, high transparency and should be able to withstand high (sintering) temperatures i.e. 450 – 500 °C. In addition, it should also prevent impurities like moisture and oxygen to penetrate into the solar cell. Transparent conducting oxides such as indium tin oxide (ITO) and fluorine tin oxide (FTO) coated glass substrates are predominantly used since they fulfil majority of the criteria for DSSCs incorporation, including low sheet resistance i.e. ~ 10 $\Omega\ \square^{-1}$ and high transparency. However, ITO and FTO substrates are brittle, fragile, heavyweight and costly [71]. These issues can be addressed by using plastic substrates or metal sheets. Conductive plastic foils such as indium tin oxide/polyethylene naphthalate (ITO/PEN) and indium tin oxide/polyethylene terephthalate (ITO/PET) are light weight and offer flexibility, whereas the metal substrate are robust, cheap and highly conductive [71]. Low temperature resistance, high sheet resistance (60 $\Omega\ \square^{-1}$ in case of ITO/PET substrates) and uncertainties regarding the penetration of moisture and oxygen into the solar cell are the main disadvantages of using conductive plastic sheets as

substrates. When considering the case of metals, the main problem is their incompatibility with iodine-based electrolytes that are corrosive in nature. So far only stainless steel and titanium have proven their chemical stability when employed as substrate in DSSCs and exposed to iodine-based electrolyte. Further, the long-term stability of metal-based cells is still under question and requires further research before their introduction on a commercial scale. The main incentive behind the research in alternative flexible (plastic or metal) substrates is that it enables the roll-to-roll production of DSSCs, thereby potentially leading toward cheap mass production of DSSCs, along with diverse applications.

2.2.2.3 Mesoporous oxide film development:

There are a couple of different wideband metal oxide semiconductor materials used in the fabrication of photonanode like titanium dioxide (TiO_2), zinc oxide (ZnO), tin dioxide (SnO_2), niobium oxide (Nb_2O_5) etc [72]. In addition to that, simple oxides, ternary oxides like strontium titanate ($SrTiO_3$) and zinc stannate (Zn_2SnO_4) along with core-shell structures (ZnO coated SnO_2) have also been studied [73]. Below a short overview related to the development of TiO_2, ZnO and other metal oxides is presented.

2.2.2.3.1 TiO_2:

TiO_2 is the most abundantly used semiconductor owing to the numerous advantages of its use i.e. non-toxicity, low cost, high stability, commercial availability, biocompatibility and better power conversion efficiency, when integrated within a solar cell [72]. In addition, it has a conduction band energy level that is right below the LUMO

level of the most commonly used (Ru based) dyes, for smooth electron transportation. The TiO_2 naturally has several crystal forms/polymorphs including anatase, rutile and brookite. Rutile is generally considered to be the most stable crystal form of TiO_2. However when considering DSSC application anatase is preferred, owing to its wide band gap i.e. 3.2 eV (as compare to 3.0 eV in case of rutile) and higher edge energy of conduction band. This eventually results in a higher fermi-level for the TiO_2 semiconductor layer and thus an increased $V_{oc.}$ A state-of-the-art TiO_2 DSSC employs multilayer photoanode configuration consisting of a TiO_2 blocking layer, light absorption layer and light scattering layer [73]. The function of the blocking layer is to prevent direct contact between the metal-oxide (ITO/FTO) substrate and the redox mediator. The light absorption layer is aimed to provide large surface area for enhanced dye loading and to offer low resistance to the flow of electrons generated as a result of photon-excitation. A light scattering layer can significantly improve the number of excited dye molecules (at any given time) by means of changing the angle of incident light and making it reach farfetched locations of the absorption layer. In addition to the above mentioned layers, an ultrathin overcoating of TiO_2 is also deposited.

The use of semiconductor nanoparticles for the fabrication of photoanode is a common practice, since it allows an increased surface area and therefore better dye loading. However, large surface area means that the chances of recombination between the electrons (lying in the conduction band of the semiconductor material) and electron acceptor species (present in the electrolyte) are increased [74]. The recombination of e-h pairs can be avoided by the introduction of metal oxide semiconductors with varied band gaps, surface passivation, addition of spacer units between the oxidized dye and TiO_2 [74].

2.2.2.3.2 ZnO:

ZnO is one of the first semiconductors investigated for DSSC integration purposes and has been attracting the interest of researchers in recent times due to the relative ease with which ZnO crystals (having different morphologies) can be synthesized. In addition, ZnO nanoparticles can be deposited on a variety of different substrates using deposition methods like screen printing, doctor blade, electrophoretic deposition etc. It has a wide bandgap (3.2 eV) similar to that of TiO_2 (anatase), a higher extinction binding energy (60 m eV) and a high electron mobility [56]. On the other hand, ZnO exhibits a poor chemical stability and dissolves under acidic and basic conditions [73]. In addition, it has a large grain size, reducing the effective surface area available for dye loading [46].

2.2.2.3.3 Other metal oxides:

SnO_2 is another stable metal oxide employed in DSSCs and having a conduction band situated at 0.5 eV. Since the conduction band of SnO_2 is at a lower level as compared to TiO_2, it is used with dyes having a lower LUMO level (e.g. perylene sensitizers) [75]**.** The best reported efficiency of SnO_2 is 2.8%, achieved when sensitized using D149 dye [76]. The highest V_{oc} achieved for SnO_2 DSSCs using conventional iodide/triiodide based electrolytes is around 400 mV. This V_{oc} value can be increased by covering the mesoporous SnO_2 particles with thin shell of other metal oxides like zinc oxide (ZnO), magnesium oxide (MgO) and aluminium oxide (Al_2O_3). So far the best efficiency achieved for hybrid SnO_2 DSSCs is around 6.3%, obtained for ZnO coated SnO_2 [77].

Another applicable metal oxide is $SrTiO_3$, which has conduction band edge that is 0.2 eV higher than that of TiO_2 and also yields a good V_{oc}. However, it has a reported efficiency of 1.8%, only. Lastly, an efficiency of 5% at 0.1 Sun has been reported for Nb_2O_5 metal oxide [78].

2.2.2.3.4 Light scattering layer:

One way of increasing the low-energy level spectral response is by increasing the thickness of the dye-sensitized semiconductor layer beyond ~10 μm. However, this would result in an increased electron transport path, number of trap states and eventually significantly decreased photocurrent. An alternative way of addressing this issue is to increase the light path by means of scattering light, which can be achieved by mixing small sized nanoparticles (~ 20 nm diameter) and large nanoparticles (~250 nm to 300 nm diameter) together. Multi-layer stacking configuration can also be utilized to increase the scattering of light. Wang et al. deposited multiple layer with nanoparticles varying in size (ranging for 100 nm to 23 nm) and achieved an increased incident photon-to-current efficiency (IPEC) in the red part of the visible region alongside a 10.2% power conversion efficiency [79]. Haze, which is the ratio of diffused transmittance to the total transmittance, can be used to quantify the level of scattering achieved by means of different configurations. Chiba et al. demonstrated the incorporation of ~ 400 nm diameter TiO_2 nanoparticles in the photoanode, which significantly increased the haze and the IPCE ratio in the NIR region, has eventually resulted in an efficiency as high as 11.1% [80].

2.2.2.4 Electrolyte:

As discussed before the function of electrolyte is to re-generate the dye molecules (oxidized due to transfer of electron to semiconductor) by donating an electron. The electrolyte is also responsible for the transfer of holes to the counter-electrode. It is one of the key limiting factors in the long-term stability of the DSSC. An ideal electrolyte should have the following properties [66]:

1. It should be highly conductive alongside low viscosity, for faster transportation of electrons.
2. It should have a good interfacial contact with the dye-sensitized semiconductor layer and counter-electrode.
3. The electrolyte should not absorb any light in the visible region of the spectrum in the range 390 nm to 700 nm.
4. It should not take any role in the desorption and degradation of dye molecules by any means.

There are several types of electrolytes, namely, the volatile organic solvents (VOSs), room temperature ionic liquids (RTILs), polymer electrolytes, redox couples, etc. [44].

VOSs are frequently used as electrolyte in DSSCs since they have a high IPCE peak value (lying within the range of 74 – 78%) as compared to ionic liquid electrolytes [44]. However, they tend to exhibit poor long-term stability and complex up scaling procedure. Further, they also have low boiling point, eventually leading towards degradation and loss of additives. These disadvantages have limited the prospects of VOS based DSSCs.

RTIL electrolytes are considered as better alternative to VOSs, since they are non-volatile, have high chemical stability and ionic conductivity. On the down side, ionic liquids tend to have leakage and solvent evaporation. These drawbacks confine the DSSCs to a fixed shape, thereby reducing the number of different applications in which they can be utilized.

Polymer based electrolytes comprising of low lattice energy metal slats dissolved in polymer matrices (i.e. ester, ether etc.), address some of the key issues associated with RTILs, including solvent evaporation and electrolyte leakage. In addition they also exhibit high ionic conductivity and excellent thermal stability. High ionic conductivity is achieved by means of fast segmental movement alongside Lewis-type acid-base interaction between the cations and the donor atoms, existing in the structure [44]. The realization of polymer electrolyte based DSSCs assembly on a large scale is more practical, since the sealing problem becomes downplayed.

In the past, gel polymer electrolytes synthesized using liquid, organic solvents and inorganic, iodine salts, have also been deployed. They tend to establish excellent contact between the electrodes. In addition to that, they also have high ionic conductivity and low vapour pressure.

In case of quasi-solid state DSSC, liquid electrolytes are solidified using organic/inorganic gel electrolytes and sol-gel silica. During the initial stages of the gel formation, the electrolyte can penetrate through the mesoporous semiconductor layer and can establish an efficient direct contact with the dye-sensitized TiO_2 nanoparticles. Since liquid electrolytes are held in gel nets, the instability caused by the electrolyte evaporation

is diminished. In addition, they also tend to have high ionic conductivity since an environment similar to liquid electrolytes is offered for the ionic movement.

2.2.2.5 Counter-electrode:

An ideal counter-electrode should be having the following characteristics:

1. It should be having a low charge transfer resistance as well as high exchange current densities for the prompt reduction of the oxidized form of charge mediator [81].
2. It should have a low overvoltage and should be able to carry photo-generated current over the whole area of the solar cell, for the effective reduction of the ion species.

Below is a list of materials commonly used in counter-electrode configuration.

2.2.2.5.1 Platinum;

Numerous counter-electrodes have been put to test, till the present day. So far, Pt is the best catalyst known for the reduction of I_3^- ion species since it has high current density, high transparency and good catalytic activity [46]. However, Pt is a rare and expensive metal. In addition, catalytic activity also tends to decrease upon the exposure to dye solution in presence of iodine based redox couple, due to the blockage incurred by the dye molecules [82].

2.2.2.5.2 Carbon:

A cost effective alternative to Pt is carbon because of its acceptable conductivity, electrocatalytic corrosion and heat resistant properties. Porous carbon electrodes consisting of crystals can easily be fabricated using graphite. The hybrid platinum/carbon (Pt/C) counter-electrode has been reported to achieve the same efficiency as Pt electrodes (i.e. 6.72%), when used in DSSC assembly, thereby reducing the cost of DSSC fabrication, without any compromise on efficiency [83]. Josef et al. reported an efficiency of 7.55% by incorporating a hybrid counter-electrode consisting of multiwall carbon nanotubes (MWNT) and graphene flakes (Gr-F), into DSSC [84].

2.2.2.6 Sealants and sealing methodologies:

Sealing plays an important role in the long-term stability of the DSSCs and prevents diffusion/leakage of materials in or out of the solar cell. An ideal sealant should be airtight in order to minimize the leakage of solvents. It should hold the cell together over a wide range of temperatures and should not allow direct contact of electrolyte with the collectors and with the other cells [85]. In addition, it must be chemically resistant to solvents, redox couple and other additives present in the electrolyte. Lastly, it should be easily cured at temperatures around 170 °C, using a hot plate or hot iron. A series of sealant materials have been investigated in the past such as thermoplastic hot-melt foils (i.e. Surlyn, Bynel, etc.), elastomeric polymers, adhesives, UV curable glue and glass frit (GF) [86]. GF is considered one of the strongest contenders since it has all the qualities of a substrate thus ensuring maximum compatibility [86]. Furthermore, it is non-penetrable and stable under

UV and high temperature exposures. However, lead-free glass frills require an elevated temperature of 600 °C in order to form an effective sealing, and thus might degrade the dye [85]. It is therefore practically recommended to seal the solar cell before pursuing the dye-sensitization process. Dyeing can be done using drilled holes in the counter-electrode, which should be later sealed.

2.2.3 Photovoltaic parameters:

The performance of a solar cell is evaluated by various parameters, extracted using *I-V* curves as shown in Figure 2-9 [87]. The most important performance evaluating parameters are described below.

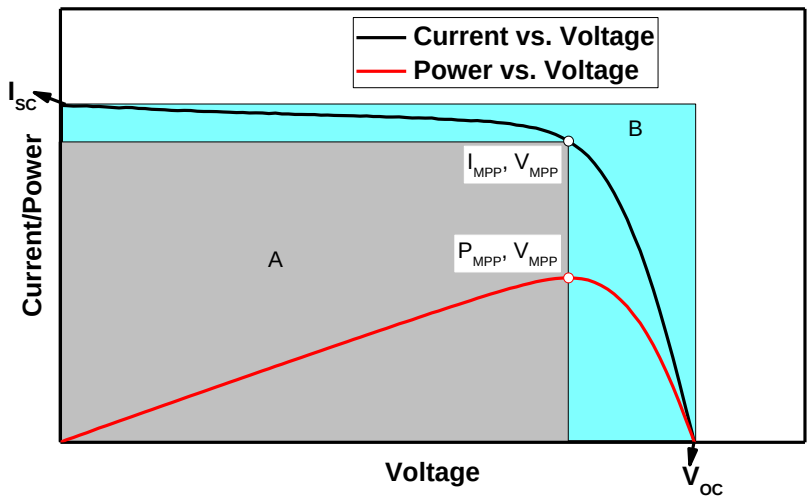

Figure 2-9: I-V curve under illuminated conditions.

2.2.3.1 Short circuit current:

It is the maximum amount of current produced, when the potential difference across the solar cell is zero (short circuit). The higher the value of I_{sc} the better the performance of solar cell is. I_{sc} is measured in Amperes (A) and is dependent of various factors including the technology being used, area of the solar cell, the amount of irradiance falling on the cell and angle of the cell. The short-circuit current density (J_{sc}) is also a commonly used parameter extracted by dividing I_{sc} by the area of the solar cell.

2.2.3.2 Open circuit voltage:

It is the maximum amount of voltage produced when no current flows through the external circuit (open circuit). Like I_{sc}, a higher value of V_{oc} is preferred. It is measured in Volts (V) and has a strong dependence on the technology being used and the temperature of the solar cell.

2.2.3.3 Shunt resistance:

Upon applying a positive potential across the solar cell, the current produced starts decreasing slowly. The rate at which the current drops may vary depending on the shunt resistance (R_{sh}) of the solar cell. A small R_{sh} value will result in an increased leakage current, thereby increasing the rate at which the current drops. It is equal to the inverse of the slope of the (straight line) region lying before the maximum power point (*MPP*).

2.2.3.4 Series resistance:

The series resistance (R_s) is the resistance offered to flow of electrons through the cross section of solar cell. A large series resistance would result in lowering of the current and fill factor. The series resistance can be calculated by the inverse of the slope of the (straight line) region lying after the *MPP*.

2.2.3.5 Maximum power point:

It is the (one and only) point at which the product of voltage and current (i.e. power) becomes maximum as expressed in Eq. 2.13. The maximum power occurring at the *MPP* is denoted by P_{mpp} or P_{max}. It is measured in watts (W), with a higher value preferred for a better performance of the solar cell. It generally occurs at the 'knee' or 'bend' of the *I-V* curve. I_{mpp} and V_{mpp} denote the current and voltage that yield P_{mpp}, respectively. The value of I_{mpp} and V_{mpp} are always less than the respective I_{sc} and V_{oc} values.

$$P_{mpp} = I_{mpp} \times V_{mpp} \qquad \ldots\ldots\ldots\ldots\ldots\ldots (2.13)$$

2.2.3.6 Fill factor:

The fill factor (FF) is the ratio of areas under I_{mpp} - V_{mpp} rectangle to that of the I_{sc} - V_{oc} rectangle as given in Eq. 2.14. In other words, it is the measure of the squareness of the I-V curve. It is preferred to have a higher value of *FF*. In case the I-V curve is a perfect square, the *FF* is equal to 1. However, it is not possible in real devices and the *FF* will

always remain less than 1. Apart from V_{mpp}, I_{mpp}, V_{oc} and I_{sc}, the *FF* depends on R_{sh} and R_s as well.

$$FF = \frac{V_{mpp} \times I_{mpp}}{V_{OC} \times I_{SC}} \qquad \ldots\ldots\ldots\ldots\ldots\ldots (2.14)$$

2.2.3.7 Power conversion efficiency:

Power conversion efficiency (η) is the ratio of maximum output power (P_{mpp}) to the input power (P_{in}) and thus is defined as the percentage of radiation input power converted into electrical power, Eq. 2.15.

$$\eta = \frac{P_{mpp}}{P_{in}} \qquad \ldots\ldots\ldots\ldots\ldots\ldots (2.15)$$

If Eq. 2.15 is rearranged, then P_{mpp} turns out to be

$$P_{mpp} = FF \times I_{sc} \times V_{oc} \qquad \ldots\ldots\ldots\ldots\ldots\ldots (2.16)$$

With the area (A) of the cell taken into account the % efficiency can be rewritten as

$$\eta\ (\%) = \frac{I_{sc} \times V_{oc} \times FF}{P_{inc} \times A} \times 100 \qquad \ldots\ldots\ldots\ldots\ldots\ldots (2.17)$$

2.2.3.8 STC measurements:

It is quite difficult to extract performance indicating parameters out of the outdoor measurements, since the environment to which solar cells/panels are exposed to, is subjected to changes based on the weather conditions, location, time of the day and season. Therefore in order to reliably extract performance evaluation parameters, long term measurements (spanning over a year) are necessary. However due to a fast paced solar industry, a quick alternative is required that is free of the environmental variations and guarantees trustworthy extraction of parameters available for standardized comparison. In order to achieve it various standards have been set, with the standard test conditions (STC) measurement system being the most widely adopted. Since the performance of the solar cell depends on temperature, irradiance and the light spectrum, therefore in STC measurements these parameters are kept constant at 25 °C, 100 mW cm^{-2} and AM1.5 [50].

2.3 Concluding Remarks:

This chapter presented a detailed background theory for the organic photodetectors and dye-sensitized solar cells. Various organic opto-electronic device types and configurations were introduced, alongside the measures one can take to achieve optimized performance. In addition, various parameters used for the characterization of photo-sensors and solar cells were also discussed.

The subsequent sections will deal with the experimental details and the results obtained for the various thin film opto-electronic devices, fabricated during the course of the current research work.

Chapter 3: Materials and General Experimental Procedures

3.1 Materials:

The previous chapter presented the background theory for the organic photodetectors and dye-sensitized solar cells. The later sections will deal with the employed materials and the experimental details related to various thin film opto-electronic devices fabricated during the course of the current research work.

Various types of materials were utilized for the fabrication of electrodes, photodiodes and solar cells. Below is the list of key materials utilized during the course of the pursued research work.

3.1.1 Copper nanowires:

Nanowires are conductive nanofibers having a solid core and a diameter of less than 100 nm. They find their application in a variety of different fields, owing to their electrical optical, magnetic and chemical properties [88-90]. They are considered promising candidates for their integration within nanoelectronics due to their high electrical conductivity and small size [91-93]. In the past, nanowires made of silver (Ag), aluminium oxide (Al_2O_3) and other metal/metal oxides have been reported. Copper nanowires (CuNWs) have attracted a lot of attention due to their high conductivity, transparency and flexibility. In addition, when considering the bulk material, Cu costs only a fraction of the amount incurred for Ag. In the current work, randomly scattered CuNWs networks have

been utilized as a cost-effective replacement of ITO based transparent conducting electrodes in a dye-sensitized photo-sensor (DSPS).

3.1.2 Graphene and its derivatives:

Graphene is a two dimensional allotrope of carbon that consists of a hexagonal arrangement of carbon atoms in a single plane, Figure 3-1 [94]. It has yielded record values for numerous properties including thermoelectric power, carrier mobility, tensile strength etc. Amongst its numerous applications, graphene can be used in touch screens, batteries, car tyres, solar cells etc. to serve purpose of reducing cost, enhancing strength or conductivity. One of the biggest problems with graphene is that it is not easy to fabricate. Graphene oxide, an oxidized derivative of graphene offers a cheap solution for the deposition of graphene layer, by means of its reduction to rGO. The present study utilizes GO oxide platelets for layer deposition and its subsequent reduction to rGO. The purpose of the use of rGO is to prevent CuNWs from oxidation, when used in TCE. In addition, it is also used to act as a catalyst and to work as a conductive medium for transfer of electrons (flowing through the counter-electrode) to one of the ion species present in the liquid electrolyte, filled in DSSCs/DSPS.

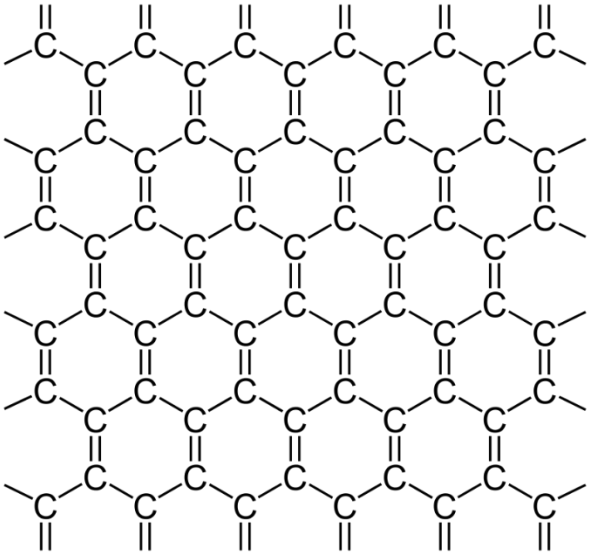

Figure 3-1: Molecular structure of graphene.

3.1.3 PEDOT:PSS:

Poly(3,4-ethylenedioxythiophene) polystyrene sulfonate (PEDOT:PSS) is a conjugated polymer that is conductive in nature and has good electrochemical, ambient and thermal stability, Figure 3-2 [95]. In case of PEDOT, ethylenedioythiophene is the basic monomer building it and is therefore insoluble in many common solvents. PSS solution is added to in order to improve the processability, resulting in an aqueous dispersion of PEDOT:PSS, where PEDOT is in its oxidized state. PSS acts as a counter ion and plays the role of keeping PEDOT chain segments dispersed in aqueous medium. In conventional opto-electronic devices, PEDOT:PSS is commonly used as an anode interlayer, to bring improvement to the contact properties between the ITO and active layer and to increase the work function of ITO for better hole collection and transportation [96]. In current work,

PEDOT:PSS is used to bring improvement in the exaction properties between the CuNWs/rGO/PEDOT:PSS based electrode and electrolyte. In addition, it also serves the purpose of reducing the RMS roughness of the randomly scattered CuNWs network.

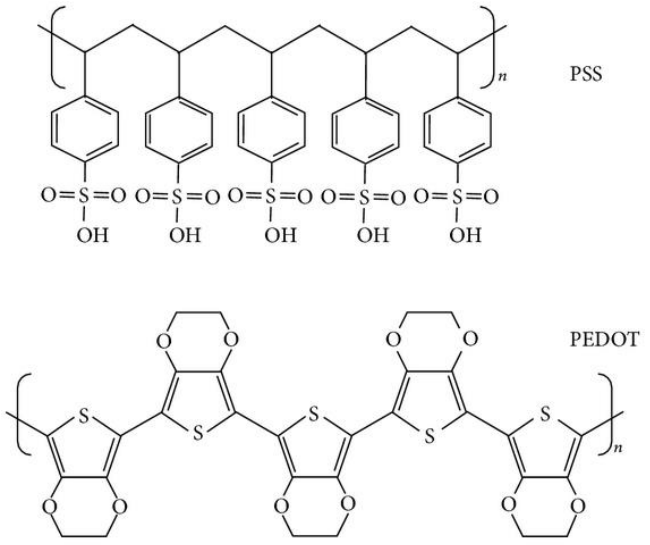

Figure 3-2: Molecular structures of PEDOT and PSS.

3.1.4 P3HT:

Poly(3-hexylthiophene-2,5-diyl) (P3HT) is also a conjugated polymer with a thiophene backbone and is commonly used as a light absorbing and hole transporting material in organic solar cells, Figure 3-3. Highest occupied molecular orbital (HOMO) of the P3HT containing delocalized electrons, is a π-band formed by the π-boned, sp^2 hybridized carbon atoms present in the thiophene rings. The HOMO level of P3HT is

situated at 5.1 eV whereas the LUMO level is present at 3.2 eV. Since the P3HT is an excellent hole transporter with mobility lying between 10^{-5} and 10^{-2} cm^2 V^{-1} s^{-1} (and having an negligible electron mobility), therefore it is used as a p-type material in the formation of an interpenetrating bulk heterojunction layer, later to be used in hybrid DSPS configuration [38, 97, 98].

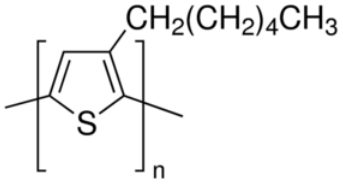

Figure 3-3: Molecular structure of P3HT.

3.1.5 PCBM:

Phenyl-C61-butyric acid methyl ester (PCBM) is a fullerene based molecule containing a Bucky-ball (C60), attached to a methyl-ester group for increased solubility, Figure 3-4. It is an n-type material having an ability to gain six electrons. The π-band (HOMO) of PCBM is situated at 6.1 eV whereas the π*- band (LUMO) is situated at 4.4 eV [99]. The electron mobility in PCBM ranges between 2×10^{-3} and 2×10^{-2} cm^2 V^{-1} s^{-1}. [97]. On the other hand, the hole mobility is negligible. In the current work, PCBM (present in BHJ active layer of the DSPS) serves the purpose of transporting excited electrons from P3HT to ITO substrate.

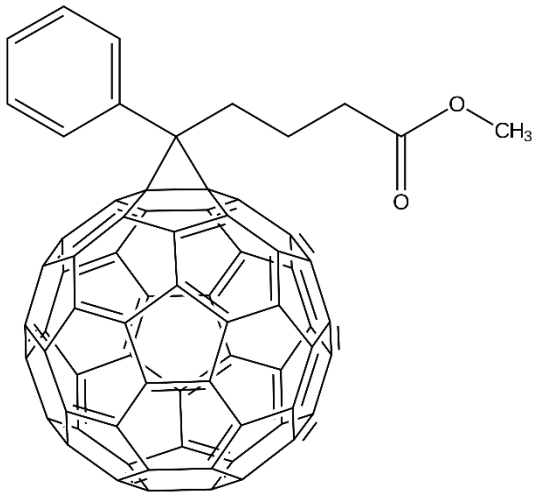

Figure 3-4: Molecular structure of PCBM.

3.1.6 ITO:

Although a certain level of transparency, with adequate conductivity can be obtained for thin metallic films, however high values of transparency and conductivity cannot be achieved simultaneously with the help of intrinsic stoichiometric materials [100]. One could only achieve this by the creation of degeneracy in a wide bandgap (E_g > 3 eV) material, using appropriate dopant and/or non-stoichiometric materials. Examples of non-stoichiometric and doped films based on indium, cadmium, zinc have been reported [101]. Indium tin oxide (ITO), having transmittance and conductivity values as high as 95% and 1×10^4 ohm^{-}1 cm^{-1} respectively, is amongst the most predominantly used thin films, and thus has found a series of electronic, opto-electric and mechanical applications [100]. In the current study, ITO slides having a sheet resistance of 15 Ω □$^{-1}$ and a work function of 4.9 eV were bought from Lumtec and used as photo-anode in DSSC assembly.

3.1.7 TiO_2:

TiO_2 was selected as the main semiconductor layer in DSPS and DSSCs owing to the fact that it is harmless, chemically stable and has a conduction band edge with an energy level that is slightly lower than the energy level of LUMO of N719 dye. A mesoporous layer of P25 TiO_2 consisting of 80% anatase and 20% Rutile and having an average particle size of 25 nm was utilized in the preparation of photo-anode. The use of mesoporous layer allowed for a significantly increased surface area, leading towards enhanced dye absorption as compared to a monolayer of semiconductor material [102-104].

3.1.8 N719 dye:

Cis-diisothiocyanato-bis(2,2'-bipyridyl-4,4'-dicarboxylato) ru-thenium(II) bis(tetrabutylammonium) also known as N719 is a high performance ruthenium based dye, having the ability to sensitize the surfaces of wide band-gap semiconductor (e.g. TiO_2) for photon absorption, Figure 3-5. The HOMO and LUMO levels of N719 are situated at -5.34 eV and -3.43 eV. In addition, its absorption spectrum contains three distinctive absorption peaks occurring at 535 nm, 395 nm and 312 nm [105]. In present study, N719 serves as the main dye for the sensitization of TiO_2 based photo-anodes.

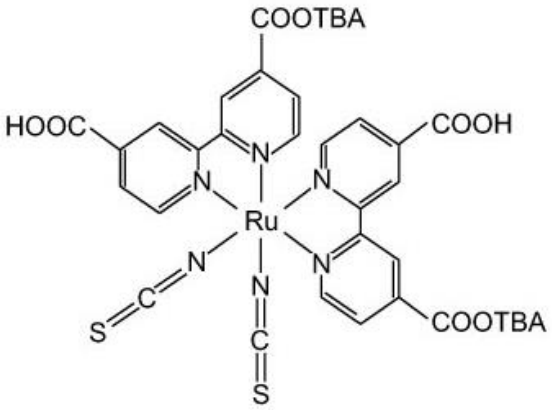

Figure 3-5: Molecular structure of N719 dye.

3.1.9 Iodolyte HI-30:

Iodolyte HI-30 is a high performance, low viscosity, volatile electrolyte consisting of iodide/tri-iodide ion species. It is used to maximize the performance of the opto-electronic devices by means of acting as a redox mediator between the active layer and the counter-electrode. This ionic liquid contains lithium salt and pyridine derivative as additives which are dissolved in acetonitrile solvent. This thesis utilizes Iodolyte HI-30 electrolyte as a redox mediator between the semiconductor layer and counter-electrode, present in DSSCs and DSPSs.

3.2 Fabrication Techniques:

3.2.1 Substrate cleaning:

Cleaning of ITO substrates is crucial in making sure that there are no organic or inorganic contaminants on the surface that might result in reduced adhesion of the subsequent layer to be deposited on top of it. The cleaning protocol pursued is mentioned as follows:

1. Cut the slides into 2.5 × 2.5 cm^2 pieces.
2. Sonicate in soap solution for 15 minutes.
3. Rinse with deionized water.
4. Sonicate in deionized water for 15 minutes.
5. Rinse the slides with acetone.

3.2.2 TiO_2 photo-anode preparation:

In order to deposit a TiO_2 semiconductor layer on top of an ITO substrate, a novel deposition technique known as electrophoretic deposition (EPD) was utilized. The deposition process started off with the preparation of TiO_2 paste. 3g of TiO_2 (P25) along with a small amount of acetylacetone was added to 60 ml ethanol and stirred for 24 hours. A charging solution was prepared separately by dissolving 63 mg of iodine in a solution containing 250 ml ethanol, 10 ml acetone and 5 ml deionized water.

Before commencing the deposition process, the TiO_2 paste was poured into the charging solution and sonicated for 15 minutes. Later, the solution containing charged TiO_2 nanoparticles was poured into a vessel, specially designed for EPD deposition. Once ready

for deposition, two ITO based transparent conducting electrodes (TCEs) were immersed into the solution. Upon the application of voltage, a layer of TiO_2 nanoparticles got deposited on the surface of anode. Once the deposition process was completed, the semiconductor coated photo-anodes were allowed to dry for 30 minutes and later sintered.

3.2.3 Synthesis of CuNWs:

In order to synthesize CuNWs, a single-step process based on the study done by Guo et al was followed [106]. In short, 1.6 mmol copper chloride ($CuCl_2$) and 0.8 mmol nickel(II) acetylacetonate ($Ni(acac)_2$) were dissolved in 20 ml oleylamine solution and kept at 80 °C. After the full dissolution was achieved, the temperature was ramped up to 175 °C to initiate the growth of CuNWs. The temperature of the solution was maintained at the above specified value for a duration of 10 hours, to allow the growth process to complete. Upon the expiry of the duration, the solution was allowed to cool down and excess hexane was poured into the solution containing flask, for the precipitation of nanowires. Once settled, the nanowires were separated from the solution via centrifugation and transferred into toluene.

3.2.4 CuNWs/rGO/PEDOT:PSS counter-electrode:

The preparation of counter-electrode started off with the deposition of a randomly scattered CuNWs layer, via spray coating. CuNWs contained in isopropyl alcohol (IPA) solution were sprayed onto substrates laid flat on hot plate kept at 70 °C. After the deposition, the slides were plasma cleaned in order to remove all the organics.

For the deposition of rGO on top of CuNWs, market purchased graphene oxide (GO) platelets were diluted in IPA and spray coated onto the substrate. Later, the fabricated electrodes were annealed at 180 °C for the effective reduction of rGO and the restoration of conductivity of CuNWs.

In the end, PEDOT:PSS layer was deposited by heating the polymer to 70 °C and then spin coating it onto the sample substrates, being spun at 6000 rpm.

3.2.5 P3HT/PCBM film deposition:

Initially 1 wt% solutions of both P3HT and PCBM were prepared separately, in chloroform. The vials containing both the solutions were stirred at 1000 rpm for 24 hours. Later, the homogenized PCBM and P3HT solutions were mixed together in equal concentrations. To commence with the deposition via spin coating, cleaned ITO substrate was fixed onto the rotating chuck and 100 µl of the mixed solution was dropped onto it. The substrate was spun at a 1000 rpm, dried and finally annealed at 110 °C for a duration of 30 minutes.

3.2.6 DSSC/DSPS assembly:

The assembly process started off with the sensitization of fabricated TiO_2 based photo-anodes, by soaking them in the dye solution. After a period of 24 hours, the sensitized electrodes were rinsed and dried in ambient environment for 30 minutes. The photo-anodes were later combined with counter-electrode with the Surlyn sealant placed between the two electrodes. The whole assembly was heated to allow for an effective

sealing to form. Few drops of Iodolyte HI-30 electrolyte were dropped through a drilled hole to fill the vacant space present between the active layer and the counter-electrode. In the end, the drilled hole was also sealed using sealant and a thin glass slab.

3.3 Characterization Techniques:

3.3.1 Morphological characterization:

3.3.1.1 Scanning electron microscope:

Scanning Electron Microscope (SEM) is used to study the morphology of materials at extremely high magnification levels, by means of utilizing electrons instead of photons. When in operation, the tungsten filament present in the electron gun gets heated (to ~ 2400 °C) and starts emitting electrons, Figure 3-6. The generated electrons are accelerated with the help of anode, having an acceleration potential lying between 1 kV and 30 kV. Since the accelerated electrons are quite scattered, therefore magnetic lenses are used to focus the electrons into a narrow beam. These magnetic lenses also control the amount of electrons that reach the sample. Scanning coils are used to make the electron beam move in such a way that row by row scanning of the sample's surface takes place. The final focusing of the electron beam is done with the help of an objective lens.

Each point on the selected sample's surface is bombarded by electrons, thereby emitting different signals going into the detectors and thus can be utilized for creating surface images. There are three basic type of signals that get detected by the electron microscope i.e. secondary electrons, back scattered electrons and characteristic x-rays. Upon the interaction of primary electrons with samples, some electrons (named as

secondary electrons) get knocked off from the orbitals of the atom. Since these free electrons have very low energy, therefore they can only escape the material from near the surface. After they have escaped the material they get attracted towards the collector having positive potential. Once the electrons pass the collector they interact with the (secondary electron) detector residing behind the collector, thus creating a secondary electron image of the surface, under study. The image generated by the secondary electrons is black and white, with the brightness of the surface image depending on the amount of electrons escaping it. The secondary electron yield is larger when the electron beam strikes protrusions, spherical areas and edges. However, pits and holes appear darker, as less electrons escape them.

Some of the primary beam electrons interact with the sample in such a way that they don't lose much energy. These electrons will go deeper into sample and come out in a similar direction and get detected by the appropriate detector. The electron yield for the back scattered electrons depends greatly on the substrate number. Surface details with larger atomic number than the surrounding matrix will occur brighter on the back scattered electron image.

Characteristic x-rays get created when the primary electron beam (having sufficient energy) excites the atoms of sample, which later return back into their original state after emitting x-rays. These x-rays are collected by the energy-dispersive x-ray (EDX) detector and thus allow the composition of the samples to be measured.

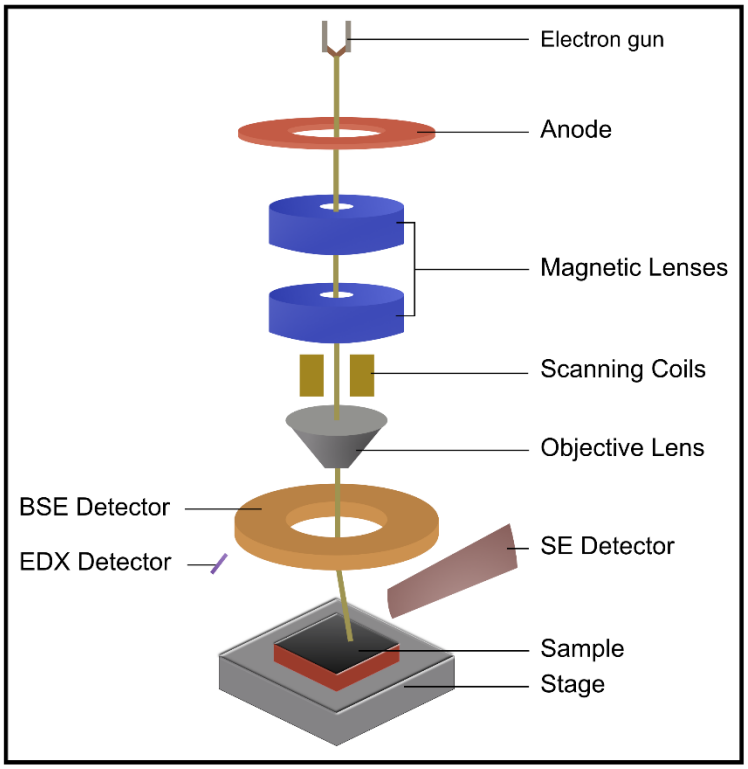

Figure 3-6: Illustration showing the operating principle of SEM.

In the present study, FEI Nova NanoSEM field emission electron microscope (FE-SEM) was used to analyse the morphology and composition of samples related to CuNWs, TiO_2, rGO and PEDOT:PSS, Figure 3-7 (a). When carrying out the measurements the samples were attached to a holder using carbon tape and placed in an air-tight chamber, situated underneath the electron beam column, Figure 3-7 (b). The pressure of the chamber was reduced significantly (~ 5×10^{-6} mbar) using a vacuum pump. Later, the electron beam was turned on with the appropriate accelerated voltage selected. In the end, specific portions of the samples were scanned for image generation, which was later saved for further analysis using ImageJ software.

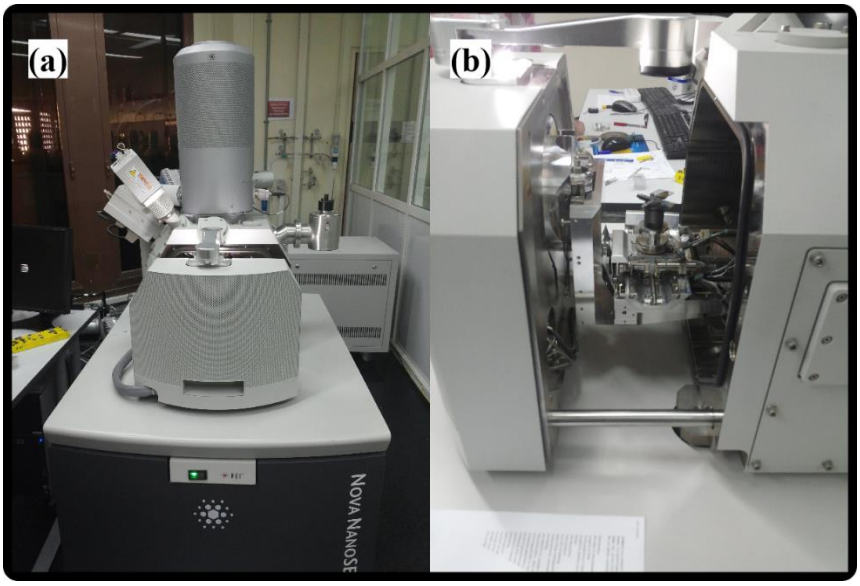

Figure 3-7: (a) Scanning electron microscope assembly, (b) Sample holding assembling fixed inside a vacuum chamber, situated right under the electron beam column.

3.3.1.2 Transmission electron microscope:

A transmission electron microscope (TEM) utilizes a beam of electrons (instead of light), thus exploiting the wave particle duality of electrons, Figure 3-8. It comprises of an electron emission source, electromagnetic lenses and an electron detector. The electron beam is produced by the electron emission source, accelerated and then focused onto a very thin sample (positioned along the electron beam) with the help of lenses. Once passed through the sample, the modified beam produces an image imprint, which is later magnified by a separate set of lenses and detectors. TEM allows the magnification of sample images down to atomic resolution. One type of transmission microscope is the scanning transmission microscope (STEM). In this type of TEM, the electron beam is focused on a

specific point of the sample (not on the whole surface) and later detected. Apart from allowing the magnified visualization of the sample's surface, it also permits the measurement of various transmitted beam characteristics, at different locations of the sample. For example, the electron energy loss (EELS) can be measured by means of a magnetic prism that deflects the beam depending on its energy. The more the beam loses energy, the more it is deflected. The measure of this deflection allows to characterize different parts of the samples. This technique allows not only to visualize but also identify the chemical nature of atoms in ultra-thin samples. In the current study, TEM was utilized for the analysis of the internal structure of IPA coated CuNW samples, deposited on Cu metal grids having a formvar film coating.

Figure 3-8: Transmission electron microscope setup.

3.3.1.3 Atomic force microscope:

Atomic force microscope (AFM), allows the generation of three dimensional (3D) images of the studied surface. The image of the surface is obtained using a very sharp tip attached to cantilever. In case when the tip is away from the surface of the sample, Van der Waals forces of attraction apply between the tip and the sample. On the other hand, if the tip gets close enough to the surface of the sample, electrostatic forces get activated. Upon the movement of the tip, the cantilever attached to it bends. The force needed to bend the cantilever is described by Hooke's law, Eq. 3.1.

$$F = -k^{*}S \qquad \text{..... (3.1)}$$

Where k^{*} is the spring constant and F is the force needed to produce a certain amount of cantilever deflection, donated by S.

The cantilever deflection is monitored using a laser beam which is focused on the cantilever and is later deflected into the detector, Figure 3-9. If the cantilever bends, the position of the deflected laser beam also changes. The scanning is done with the help of a piezotube which can bend or stretch precisely in any desired direction, depending on the electric potential being applied. The scanning can be done either by moving the sample while the tip is stationary, or by moving the tip when the sample is stationary. The lateral resolution of the images is around 30 mm, however the vertical resolution can be up to 0.1 mm.

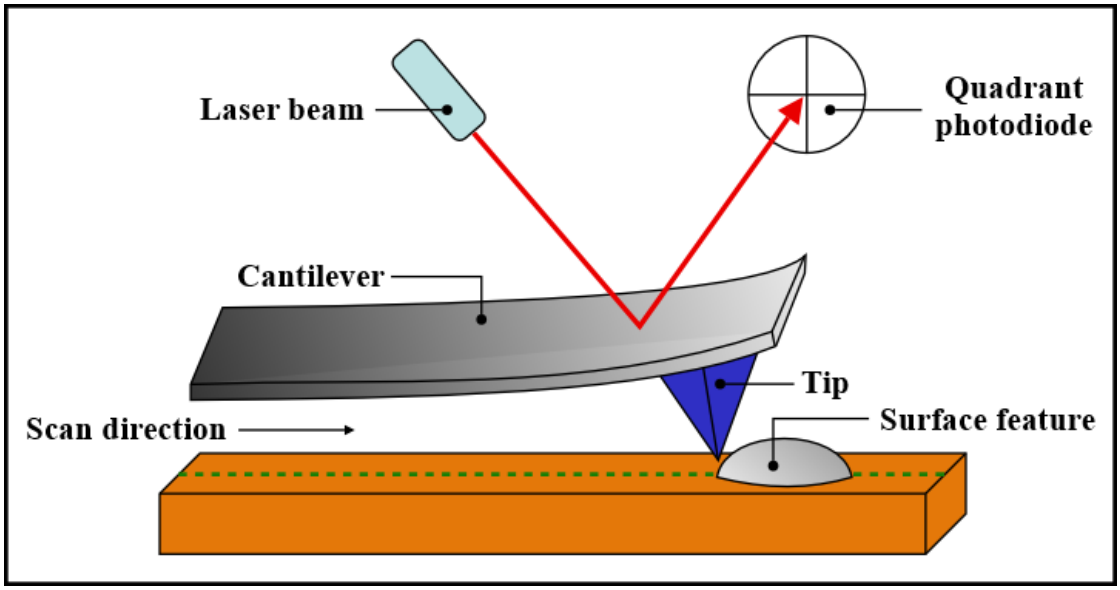

Figure 3-9: AFM schematic describing the principle of operation.

There are three basic AFM imaging modes i.e. contact mode, non-contact mode and tapping mode. In case of contact mode, the tip is in contact with the surface and thus used for studying hard surfaces. In non-contact the tip is vibrating with constant frequency above the surface of the sample. It is used for studying soft or sticky surfaces. Lastly, in tapping mode the tip is closer to the surface and thus vibrates with higher amplitude. In the lowest point of the trajectory the tip is briefly touching the surface. In the current study, AFM was utilized to study various morphological properties associated with CuNWs, rGO and PEDOT:PSS based samples, using non-contact mode.

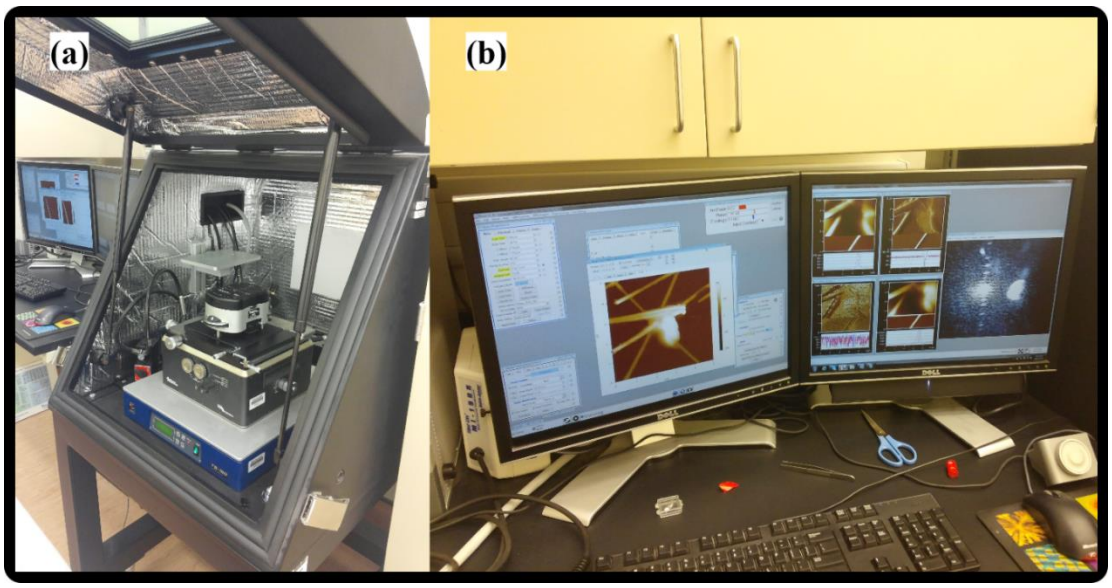

Figure 3-10: (a) Atomic force microscope assembly, (b) computer with the AFM operating software installed.

3.3.2 I-V characterization:

I-V characteristics provide us with an insight to the various electrical properties associated with solar cells and photo-sensors. During the course of research work at Qatar University, Sunlite Solar Simulator, Keithley 2400 and ReRa Tracer 3 software program were used for measurement of I-V characteristics, Figure 3-11.

Figure 3-11: Solar simulator setup used for the characterizaton of DSSC/DSPS samples.

As depicted in Figure 3-12, the solar simulator utilized has the light source fixed on a moveable mounting (held in place with the help of a counter weight) whose height can be adjusted. This allows to carry out measurements at various irradiance levels, ranging from 11 mW cm^{-2} to 120 mW cm^{-2}.

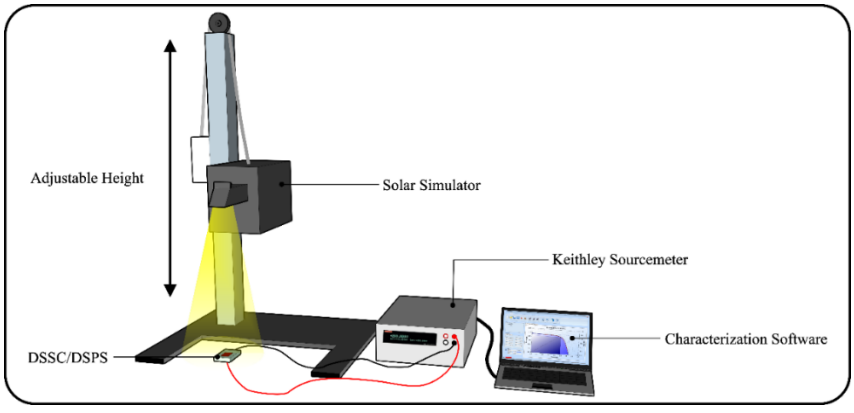

Figure 3-12: Schematic for the solar simulator emphasizing the available option of varying the irradiance level.

3.3.3 Impedance characterization:

3.3.3.1 Electrochemical impedance spectroscopy:

Electrochemical Impedance Spectroscopy has proven to be a powerful technique for studying fundamental components and processes associated with various opto-electronic devices, and is thus widely applied for the characterization of DSSCs/DSPSs. It is used to measure the impedance of a system over a wide range of frequencies and therefore provides information related to the frequency response of the system, including the energy storage and dissipation properties. The EIS data is often expressed graphically in the form of Nyquist and Bode plots.

3.3.3.2 Nyquist plot:

In case of Nyquist plot, impedance is represented as a vector of length $|Z|$ (x-axis) in relationship with negative phase angle Θ. This plot does not give any information about the frequency at a specific point. However, generally the low frequency data are situated on the right side of the plot, whereas the higher frequencies are situated on the left side. A Nyquist plot mainly contains several semicircles with each representing a single 'time constant', and thus signifying a physical behaviour.

3.3.3.3 Bode plot:

In case of bode plot, magnitude of $|Z|$ and phase Θ are plotted as a function of log frequency. In the plot, the frequency independent impedance measurements represent the behaviour of resistive processes, whereas the frequency dependent impedance data

represents the capacitive or diffusive processes. Unlike Nyquist plot this plot explicitly shows frequency information and is therefore regarded useful in the extraction of information related to significant processes used to construct the equivalent circuit.

3.3.4 Optical characterization:

3.3.4.1 Spectrophotometer:

Spectrophotometer is a device that measures light intensity as a function of wavelength. There are four main parts of a spectrophotometer i.e. the light source, object/sample holder, detector and interpreter. The light sources can generate photons lying within infrared, visible and ultra violet wavelength ranges. The light (generated by the Xenon or Halogen bulbs) fall onto a reflector by passing through a slit. The reflector reflects the light which then passes through the sample. At the end of the light path lies the detector that detects the intensity of light received and converts it into an electrical signal. The spectrophotometer can operate in two modes i.e. transmission and reflection mode.

During the course of current study, the spectrophotometer was used to measure the transmittance and absorbance for samples related to CuNWs, rGO, PEDOT:PSS and sensitizing dyes.

Chapter 4: Enhancement of Photodetection Properties By Means of Co-Sensitization

4.1 Introduction:

As mentioned in chapter 2, when considering DSPS/DSSC devices, dye-sensitizer molecules (which are chemically bonded to the porous semiconductor surface) serve the function of absorbing photons of incident light and transferring the resultant excited electrons to the conduction band of the semiconductor, thus immensely effecting the light harvesting potential and the overall photoelectric power conversion efficiency of the fabricated devices. Till today's date, ruthenium based metal complexes are the most commonly utilized sensitizers, owing to their wide absorption spectra and well matched HOMO and LUMO levels [107, 108]. Other promising sensitizers include porphyrin and phthalocyanine systems, having a strong absorption in the IR region, good thermal and chemical stability. However, these dyes use precious metal and have a low molar extinction coefficient leading towards weak light absorbance [109]. In addition, metal-free dyes based on coumarin, indoline, tetrahydroquinoline, triarylamine and heteroanthracene, have also been employed [110]. Such dyes have higher molar extinction coefficient, are comparatively cheaper and environment friendly but have a narrow absorption spectra yielding efficiencies lower than that of metal-complex dyes.

The performance of an individual dye can be enhanced by mixing it with other dyes. Co-sensitization of a dye with other dye(s) can provide an effective means of broadening the photoelectric response range of dye-sensitized opto-electronic devices [111]. This in-turn increases the output current of the DSSC/DSPS and thus results in an increased

efficiency [112]. In addition, various other effects such as low charge transport resistance, longer electron lifetime, enhanced absorbance, broader IPEC, reduction in recombination kinetics, retardation of back reaction, depressed electron recombination, increased V_{oc}, might also be observed upon co-sensitization [113-115].

This chapter deals with improving the electrical and photo-detection properties of the fabricated DSPSs by means of co-sensitizing Ru based N719 dye with a newly developed organic dye named as AS-2, Figure 4-1. Initially, absorption spectra for the dyes was measured. Later, the two dyes were mixed together in different proportions and measured again for the absorption spectra. Upon, the selection of the right dye proportion, the TiO_2 based photo-anodes were soaked either in the N719 dye or dye cocktail solution. Later, the DSPS involving a dye soaked TiO_2 photo-anode and counter-electrode were fabricated and a comparison was established between the two dye-based solar cells, using a series of experiments for the extraction of electrical, photo-detection and sensor based parameters.

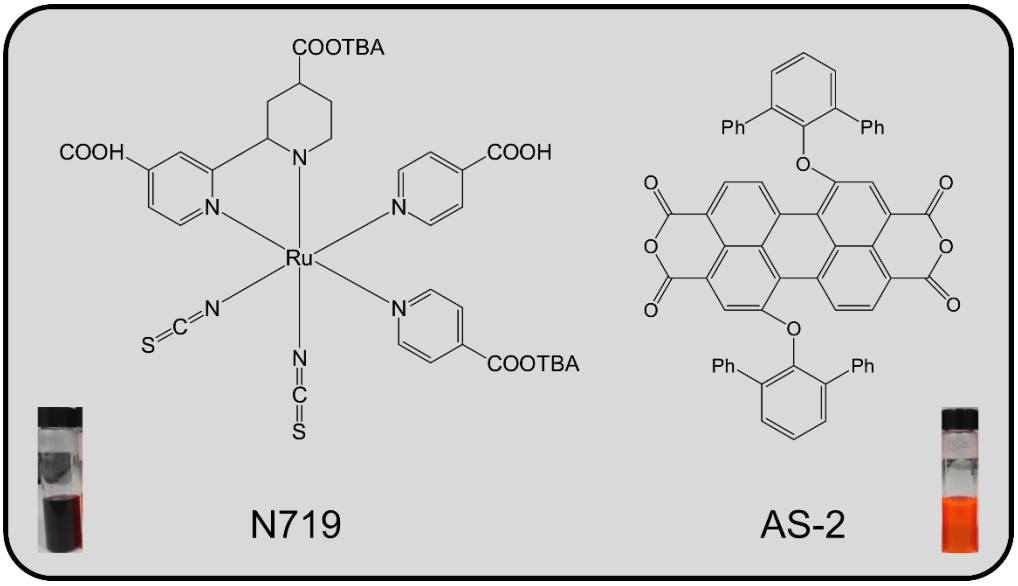

Figure 4-1: Molecular structures of N719 and AS-2.

4.2 Spectrophotometric Characterization:

Initially 0.5 mM solutions of AS-2 and N719 were prepared in acetone and characterized for their absorbance within 300 to 950 nm range, using a spectrophotometer. Absorbance measurements were also done for mixtures containing various proportions of N719 and AS-2 dye, Figure 4-2. In case of N719 two major peaks occurred at 395 nm and 530 nm, indicating maximum absorbance of photons of light, while a minor peak occurred at 366 nm. For AS-2 dye, major peak occurred around 550 nm and two minor peaks occurred at 510 nm and 390 nm. When co-sensitized with N719 in 0.25 (AS-2):1 (N719), significant changes to the N719 absorbance plot were observed. A total of three peaks were formed with the maxima of the highest peak occurring at 547 nm. The maxima of other two peaks occurred at 510 nm and 391 nm.

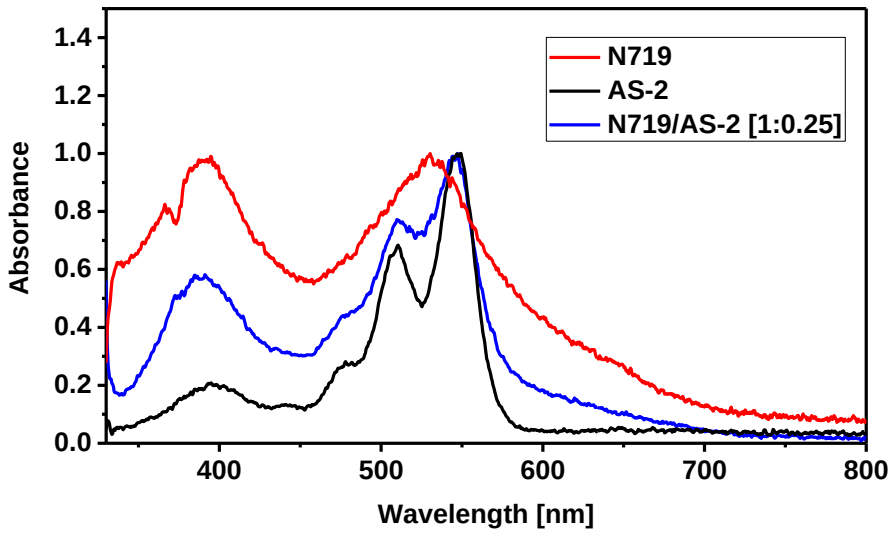

Figure 4-2: Absorbance of individual and hybrid dyes with respect to wavelength.

Apart from the absorbance measurements, various other tests were needed to be performed in order to get a better understanding of the fabricated device's performance and to figure out the suitable application for it. To do so, (dark) electrical and photo-sensory characterization was carried out.

4.3 Electrical Properties:

Devices containing photoanode sensitized either by N719 or N719/AS-2 (1:0.25) hybrid dye, were fabricated using the standard fabrication procedures mentioned in Chapter 3 and later characterized for their electrical parameters in both light and dark conditions. In case of measurements taken in dark conditions, voltage was applied in both reverse and forward biased directions, Figure 4-3. As seen, in dark conditions both devices functioned as a normal diode: they allowed the flow of current after a certain voltage threshold (V_{on})

was reached in the forward biased region, while a reverse bias gave a negligible current until the breakdown voltage was reached. Thus it can be said that both the fabricated devices supported unidirectional flow of current and exhibited a good rectification behaviour. In case of forward bias, the resistance was large at voltage levels lower than V_{on} (i.e. 0.64 V and 0.68 V for N719/AS-2 (1:0.25) and N719 devices, respectively), thereby restricting the flow of current. At higher voltage levels (exceeding the above mentioned values) the current flowed without any restriction, and increased linearly with the voltage [116]. In the reverse bias region, a leakage current/reverse saturation current (generated due to the minority carriers) was found to have a magnitude of 2.62 μA and 0.07 μA, in case of N719 and N719/AS-2 (1:0.25) devices, respectively. This leakage current kept constant until breakdown occurred, thus eliminating the diode functionality. As illustrated from the dark measurements the N719 based DSPSs reach the breakdown more quickly under reversed biased conditions, as compared to the co-sensitized DSPSs, thus indicating an alteration to the diode based properties of DSPSs.

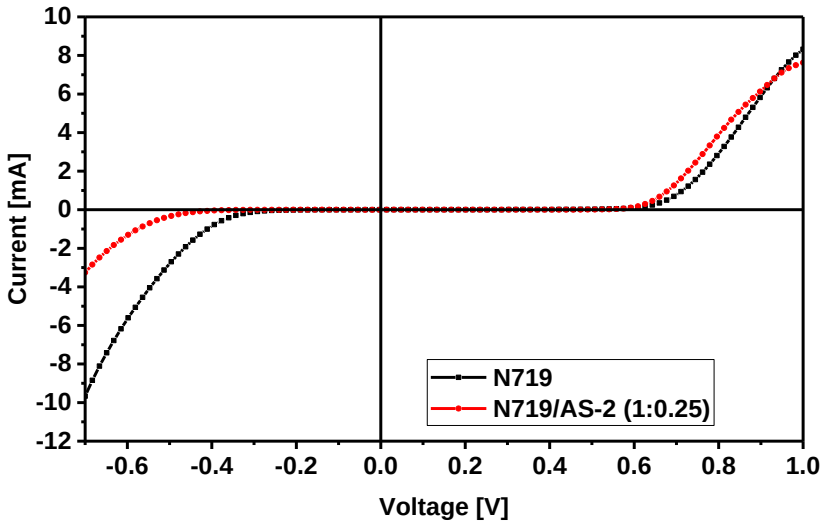

Figure 4-3: I-V characteristics for both the fabricated devices in dark conditions.

Figure 4-4 depicts the logarithmic current density as a function of the applied voltage. The value of band ideality factor η was extracted by fitting the exponential region of the forward I-V curve with the equation for thermionic emission model given by Eq. 4.1 [117].

$$I = I_s\, e^{\left(\frac{qV}{\eta kT}\right)} \qquad \text{.....(4.1)}$$

Where I_s is the reverse saturation current and can be stated as

$$I_s = AA^*T^2 e^{\left(\frac{-q\varphi_b}{kT}\right)} \qquad \text{.....(4.2)}$$

In the above mentioned equations *V* is the applied voltage, q is the electron charge, *A* is the effective device area, A^* is the Richardson constant, φ_b is the zero bias barrier height, k is the Boltzmann constant, T is temperature and n is the ideality factor. The key parametric values obtained are summarized in Table 4.1. The ideality factor (measured from the linear part in the forward bias region of the ln I-V graph) was found to be 2 and 1.35 in case of N719 and N719/AS-2 (1:0.25) based DSPSs, respectively.

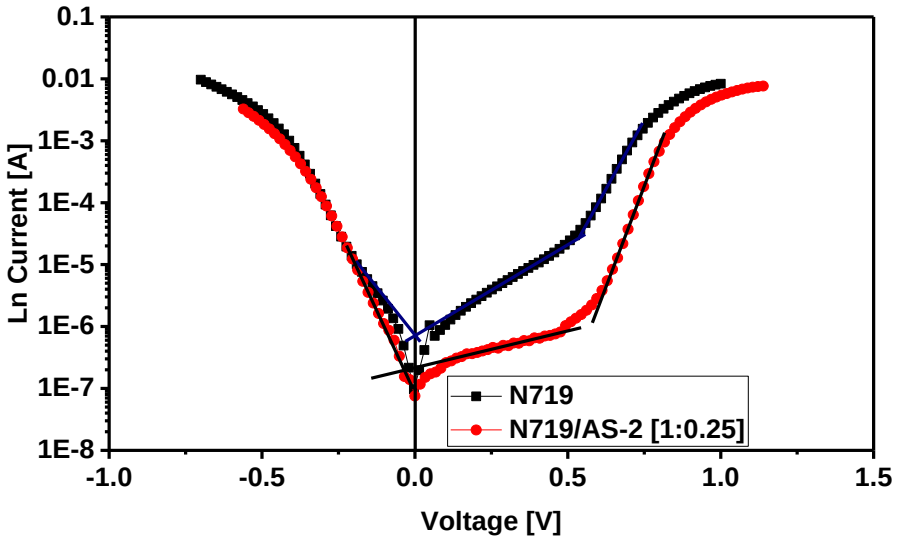

Figure 4-4: Forward and reverse bias characteristics for N719 and N719-AS2 (1:0.25) in dark conditions.

Table 4-1: Summary of parameters obtained for lnI vs V plot in dark conditions.

Parameter	N719	N719-AS2 (1:0.25)
Ideality factor	2.00	1.35
Reverse saturation current (μA)	2.62	0.07

4.4 Photo-detection Properties:

For a solar device to be suitable for photo-detection applications, it should have excellent linearity with respect to changes in irradiance level of the incident light. A photodiode is considered linear if the generated photocurrent increases linearly with the incident light power. To find out whether or not the fabricated devices have a linear relationship between current and irradiance, I-V measurements were taken at varied irradiance levels ranging from 11 mW cm^{-2} to 120 mW cm^{-2}. Later, the gathered I-V curves were utilized in finding out the I_{sc} value at the respective irradiance levels. Figure 4-5 shows the relationship between I_{sc} and irradiance, for the two solar devices. As seen both the devices demonstrated a linear (current vs irradiance) relationship. The short circuit current produced was almost identical for both the devices at low irradiance levels i.e. 10 and 20 mW cm^{-2}. As the power of the incident light was increased the difference amongst the I_{sc} of the two devices was seen to increase, with the largest difference occurring at the highest irradiance level i.e. 120 mW cm^{-2}. As indicated by the dotted straight lines, N719/AS-2 (1:0.25) DSPS tended to have a comparatively better linearity as compared to N719 DSPS with the linear relationship extending to even higher irradiance levels in contrast to the N719 DSPS that deviated from linearity at 120 mW cm^{-2}.

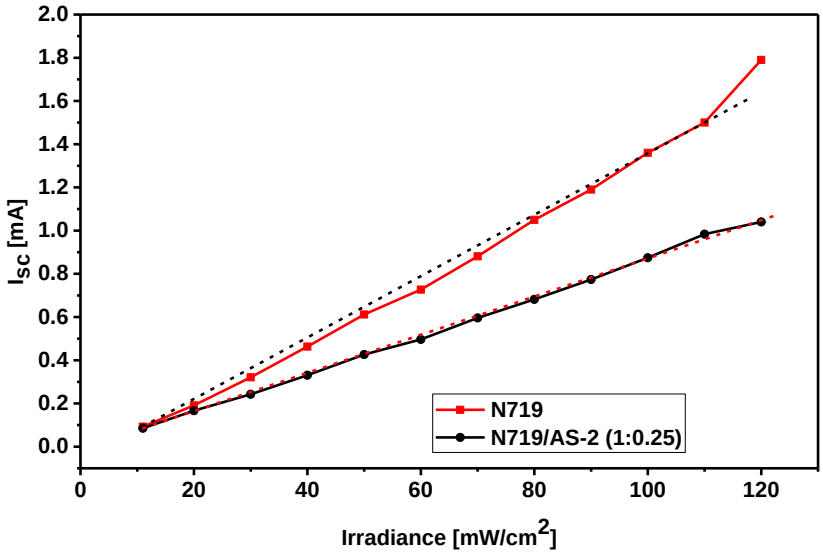

Figure 4-5: Relationship of *Isc* with irradiance.

Figure 4-6 depicts the changes in current with respect to irradiance for the two fabricated devices, while keeping the voltage fixed at 5 different levels (i.e. 0.1 V, 0.2 V, 0.3 V. 0.4 V and 0.5 V). As seen, there existed a linear relationship between the current and irradiance, for both the devices. However, at 120 mW cm^{-2} a deviation was noted in case of N719 based DSPS, at all voltage levels.

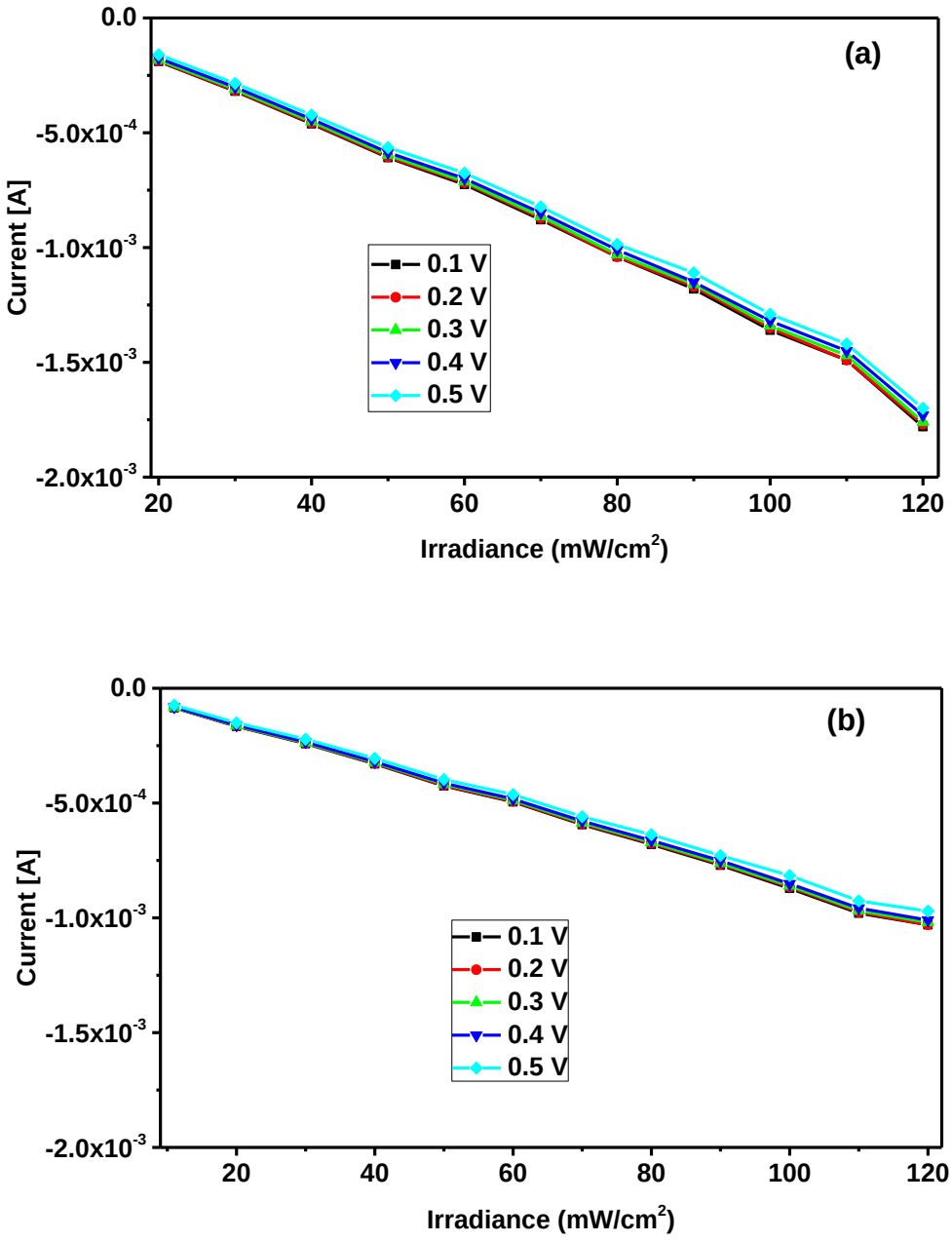

Figure 4-6: Effect of irradiance variations on I_{sc} at different voltage levels for a) N719 and b) N719/AS-2 (1:0.25) based DSPSs.

Both V_{oc} and I_{sc} vary with respect to temperature. In order to find out the temperature coefficient, the fabricated devices were heated up to 70 °C and allowed to cool down slowly. A series of I-V curves were measured as the temperature of the devices (measured by an infrared gun) slowly decreased. Figure 4-7 (a) establishes a comparison of I_{sc} with respect to temperature. As seen, there existed a negative temperature coefficient for I_{sc} for both the devices. However, a decrease in I_{sc} of 0.83 μA $°C^{-1}$ was noted down in case of N719/AS-2 (1:0.25) DSPS as compared to 10.15 μA $°C^{-1}$ for N719 DSPS. Therefore it can be said that I_{sc} for N719/AS-2 (1:0.25) had a minor dependence on temperature. A similar (negative slope) relationship was observed between V_{oc} and temperature, with the V_{oc} temperature coefficient for both the devices turning out to be identical i.e. 2.61 mV $°C^{-1}$, Figure 4-7(b).

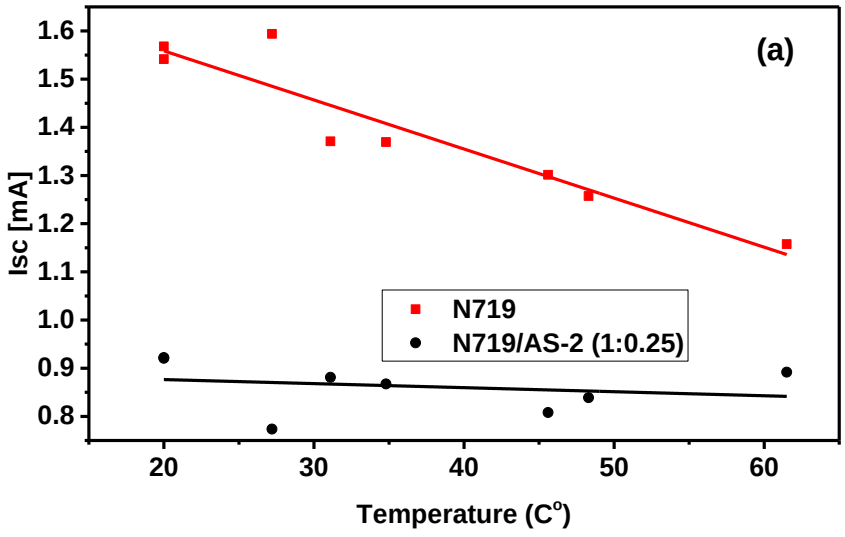

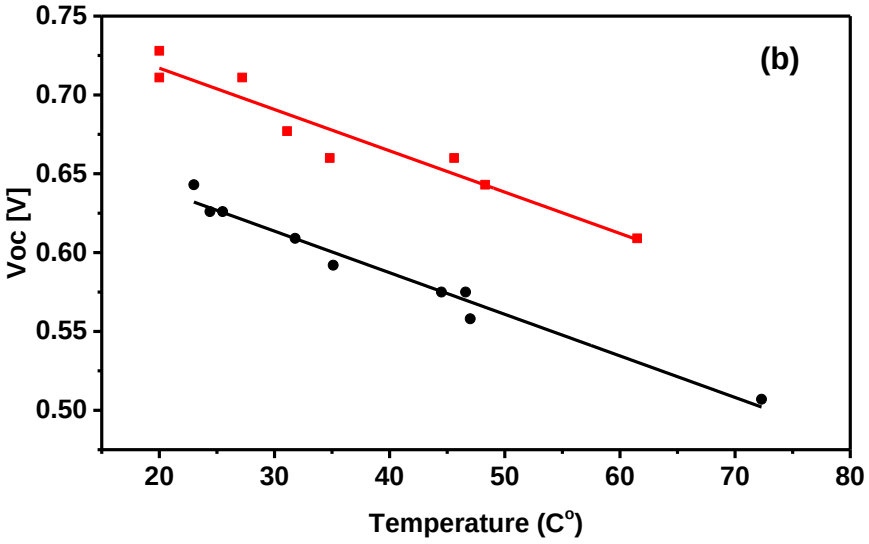

Figure 4-7: Effect of temperature variations on a) I_{sc} and b) $V_{oc,}$ for both the DSPSs.

Figure 4-8 shows the transient response of N719 and AS2/N719 DSPSs. It can be seen that upon exposure of the fabricated devices to transient light pulses, both the devices reacted swiftly. However, the magnitude of current produced by the N719 DSPS was noticed to be clearly greater than the one produced by AS2/N719 DSPS. Table 4.2, presents the summary of key parameters obtained from the above mentioned graph. The magnitude of current produced turned out to be 1.04 mA and 0.77 mA for the N719 and N719/AS-2 (1:0.25) device, respectively. The response time for the N719 dye was noted to be faster as compared to the N719/AS-2 (1:0.25). Interestingly, the reset time for both the devices turned out to be identical i.e. 0.33 s.

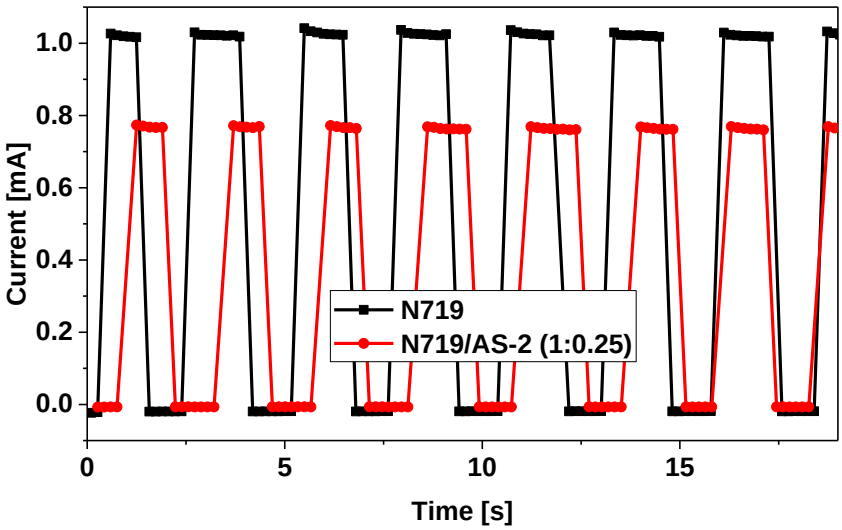

Figure 4-8: Current response for both the fabricated devices upon exposure to transient light pulses.

Table 4-2: Summary of parameters obtained from the transient response graph.

Parameters	N719	N719-AS2 (1:0.25)
Average peak current (mA)	1.04	0.77
Response time (s)	0.33	0.50
Reset time (s)	0.33	0.33
Responsivity ($\mu A.W^{-1}$)	1.02	0.76
Sensitivity ($\mu S.m.W^{-1}$)	13.89	10.29

Electrochemical Impedance Spectroscopy (EIS) analysis was performed to explain the interfacial charge recombination process in the dark, under a forward bias DC voltage of 0.6 V and frequency range varying from 10 Hz to 100,000 Hz. Figure 4-9 shows the Nyquist plots showing the relationship between the real (Z_{real}) and imaginary (Z_{imag}) part of the impedance, obtained for DSPSs based on N719 and hybrid dye. In general, a Nyquist plot consists of three semicircles (situated in higher, medium and lower frequency regions), representing electrochemical reaction at Pt/electrolyte interface, the charge transfer at TiO_2/dye electrolyte interface and Warburg diffusion process of the I^-/I_3^- in the electrolyte, respectively. However, in current case the EIS curve consisted of only two depressed semi-circles i.e. at low and high frequency levels (inset Figure 4-9), since the conventional diffusion resistance of the charge transfer greatly overlapped the conventional diffusion resistance of the redox couple. This may be attributed to short length of I^- ion diffusion available with the thin spacer and the low viscosity of the electrolyte used [118]. The smaller semicircle in the high frequency region reflected the charge transfer resistance on the pt counter-electrode (R_{ct}) while the larger semicircle at intermediate-frequency region represented charge transfer resistance (R_{rec}) at the TiO2/dye/electrolyte interface. The radius of the largest semicircle of the DSPSs based N719/AS-2 (1:0.25) hybrid dye was significantly smaller than that observed for DSPSs sensitized with N719, resulting in lower V_{oc} [114, 115]. This trend was consistent with the I-V curve measurements, with the V_{oc} decreasing from 0.72 V to 0.63 V when N719 is co-sensitized with AS-2.

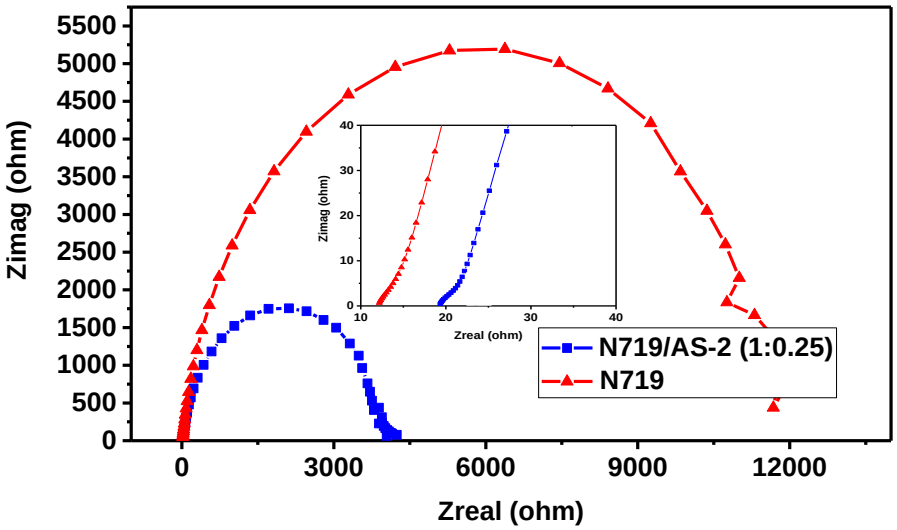

Figure 4-9: Nyquist Plot for the fabricated DSPSs.

4.5 Conclusion:

This chapter dealt with the enhancement of photo-detection properties of DSPSs by means of co-sensitization of N719 with AS-2 dye. When considering the electrical characteristics (measured in dark conditions) the N719/AS-2 (1:0.25) based devices exhibited a high breakdown and lower turn-on voltage levels. In addition the hybrid dye based devices also showed better linearity, temperature independence in terms of current produced. These results render the AS-2/N719 dye cocktail based devices suitable for photodetection applications.

Chapter 5: DSPS Based on BHJ Thin Film and Liquid-Electrolyte

5.1 Introduction:

Bulk heterojunction consisting of homogeneous blend of donor (D) polymer and acceptor (A) molecules, forming an interpenetrating network with nanoscale heterojunction interface, is considered as one of the leading organic photodiode configurations, being employed today [119-122]. For bringing enhancement to the operation of photodiode, it is vital that the charge transfer process is optimized in order to favour the transfer of photo-induced electrons to the external circuit over their recombination with holes. One such approach relates to the improvements in the kinetics of the cathode interface. When considering the operation of dye-sensitized photo-sensors (DSPSs), the cathode interface kinetics are immensely dependent on the electrolyte (redox couple based), which provides ionic conductivity between the positive and negative electrodes and is helpful in addressing two main factors: (1) retardation of the recombination process, (2) efficient transportation of charge carriers between the active semiconductor layer and cathode [122, 123]. When integrated as an intermediate layer (present between the active layer and counter-cathode) within the BHJ photo-sensor assembly, the (redox based) electrolyte can serve the same functions, thereby improving various photo-detection/sensory parameters. In addition, the use of electrolyte also offers a better contact between the active layer and counter-electrode, without the use of high cost and time consuming counter-electrode deposition process (like sputtering) [124]. These advantages eventually make the fabrication process simple, fast and economical.

With the advantages of the organic BHJ and DSPS structures taken into consideration, the current chapter introduces an inexpensive and high yield hybrid BHJ/DSPS configuration, with an added layer of liquid electrolyte, sandwiched between semiconductor and cathode.

5.2 Fabrication of Hybrid Configuration DSPSs:

Initially, 1 wt% solutions of both n-type (PCBM) and p-type (P3HT) materials were prepared in chloroform, separately in different vials. In order to obtain a homogeneous solution, the vials containing PCBM and P3HT solutions were stirred over a duration of 24 hours, at 1000 rpm. The preparation of photo-anode started off with the cleaning of ITO slides, using the standard procedure mentioned in chapter 3. Spin coating was used for the deposition of PCBM:P3HT BHJ semiconductor layer, due to the simplicity, relative ease and its worldwide adoption [125]. The homogenize PCBM and P3HT solutions were mixed together in 1:1 ratio. Later, a 100 µl of the mixed solution was poured onto the surface of an ITO substrate (size 2.5 cm x 2.5 cm) fixed on the spinning chuck and rotated at 1000 rpm. The average thickness of the deposited BHJ films turned out to be in the range of 100 ± 10 nm. Upon the completion of the deposition process, the photo-anode was annealed at a temperature of 110 ℃ over a 30 minutes duration. Standard procedures (mentioned in Chapter 3) were adopted to make DSPSs out of the fabricated photo-anodes. The energy band diagram, steps involved in the preparation of photo-anode and fabrication of the final configuration of BHJ-photo diode are all mentioned in Figure 5-1.

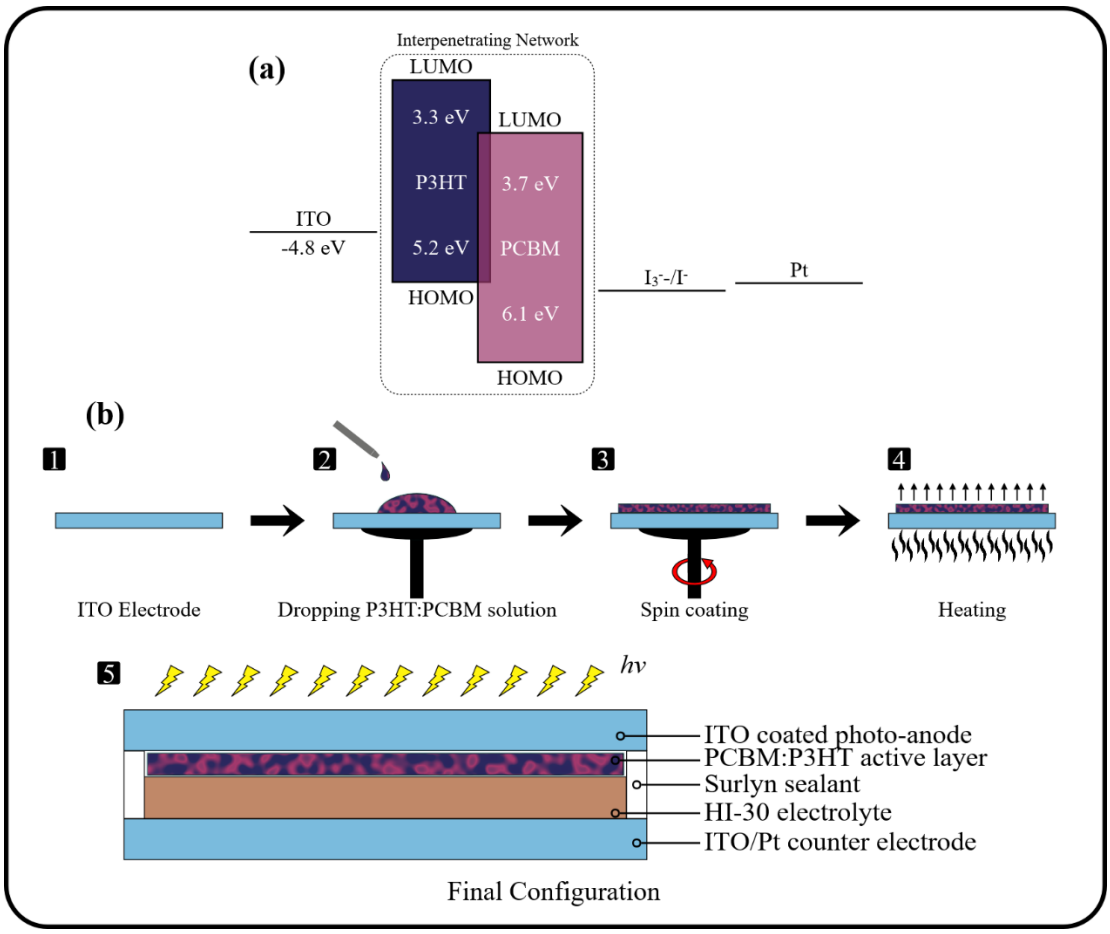

Figure 5-1: (a) Energy band diagram, (b) steps involved in the preparation of the photo-anode and the final configuration of the BHJ photo-diode.

5.3 Electrical Characterization:

5.3.1 Dark I-V characteristics:

When performing I-V measurements in the dark, the fabricated hybrid photo-detector exhibited a non-linear, asymmetric I-V curve with good rectification behaviour, Figure 5-2. In the forward biased region, an exponential increase in the current was noted

at low voltage levels. However, this I-V relationship turned quasi-linear at high voltage levels (> 0.25 V), mainly because of the minimization of the depletion layer, thereby turning the device ON and making it act like a resistor [126]. The value of voltage (V_{on}) at which the photodiode turns ON was estimated from the linear part of the forward biased I-V curve region and was found to be equal to 0.25 V. The rectification ratio (*RR*) determined using the ratio of forward current to reverse current (I_F/I_R) turned out to be 55.5 at ± 0.4 V.

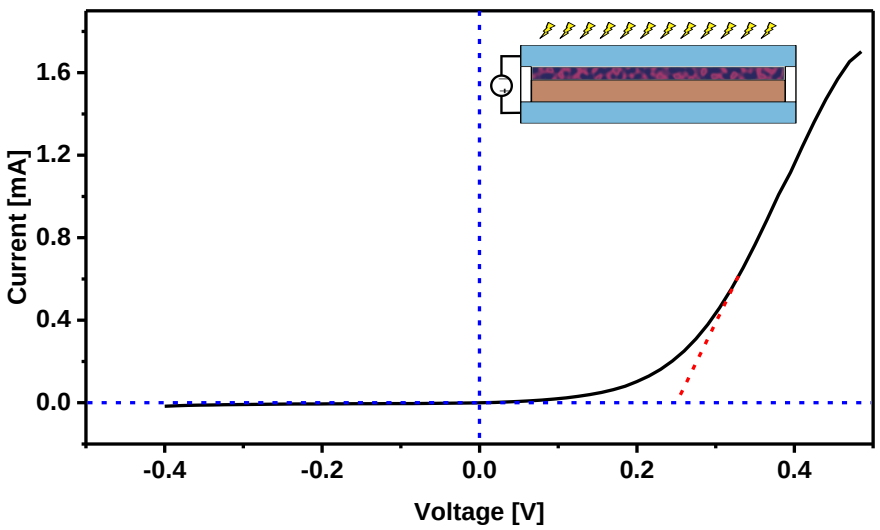

Figure 5-2: Forward and reverse biased I-V characteristics under dark conditions measured at room temperature, for the fabricated BHJ thin film/electrolyte photo-detector.

Figure 5-3 shows a graph between V and ln I, measured in the dark conditions. As observed, the I-V characteristics in the forward biased region were found to be almost

linear. However, at high voltage levels, the characteristics started deviating from linearity due to the overpowering of the increasing series resistance, offered by the contact wires or bulk resistance of the organic semiconductor material. Once operated in the reverse biased region, the leakage current (I_o) produced due to the diffusion of minority carriers across the potential barrier, was found to be equal to 4.25 µA [127].

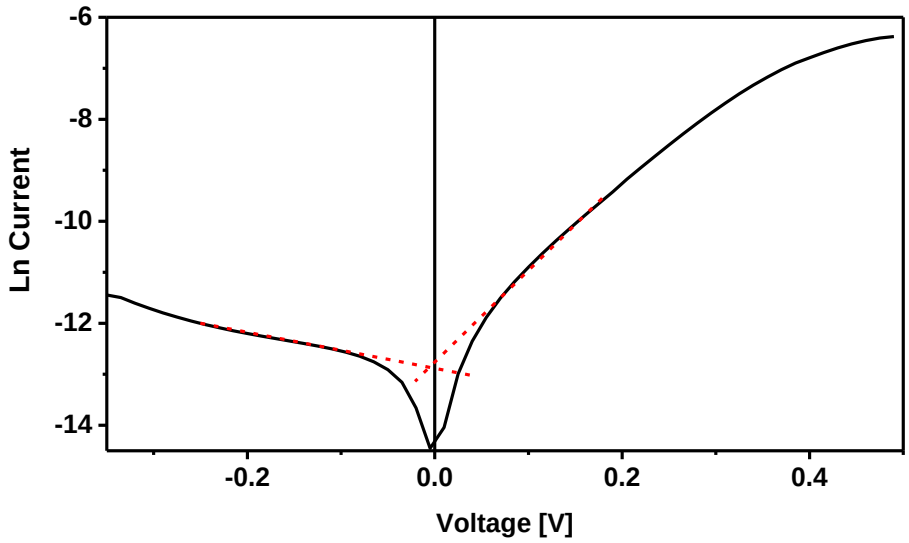

Figure 5-3: Graph between V vs. ln I in the dark.

Ideality factor is an important figure of merit used for evaluating the conformity of a device's performance to that of an ideal diode. It depends on the locus of recombination of charge carriers and has a value of unity in case of an ideal diode having no charge carrier traps and the completely redundant recombination process [128, 129]. However, when considering non-ideal photo-diodes, the ideality factor has a value greater than unity, due

to the trap facilitated recombination of electrons and holes. In case the recombination takes place in the space charge region, facilitated by the recombination centres in the band gap, the value of ideality factor escalates and becomes 2. However, ideality factor values can exceed the prior mentioned value and can be as high as 20 [130]. Because of the fact that in dark conditions a BHJ based photodetector behaves as a diode, Shockley equation describing current as a function of applied voltage can be used for finding out the ideality factor, Eq. 5.1.

$$I = I_o \left[\exp\left(\frac{qV}{nkT}\right) - 1\right] \qquad \text{.....(5.1)}$$

Using Eq. 5.1, the ideality factor was found to be 2.43 ± 0.09, indicating an electrically over-stressed semiconductor junction [131]. Numerous factors including series resistance, tunnelling effects, non-homogeneous thickness of organic film, presence of native oxide layer on electrodes, organic layer effect, voltage drop across interfacial layer and Schottky effect, might be potential reasons of the high ideality factor [126, 132].

The performance of a photo-diode is immensely effected by parasitic losses associated with series (R_s) and shunt (R_{sh}) resistances, whose values can be determined by finding and plotting junction resistance (R_J) values as a function of applied voltage. As seen in Figure 5-4, the value of R_J peaked when no biased voltage was applied to the junction and thus maximum current flowed through it. This maximum *RJ* value (in the reverse biased region) can be considered as a shunt resistance (R_{sh}). On the other hand, the series resistance (R_s) is the lowest *RJ* value occurring in the forward biased region. In case

of the fabricated DSPSs configuration, the R_s and R_{sh} resistance values were estimated to be 133.33 Ω and 74.71 kΩ, respectively. Abrupt peaks occurring in the forward and reverse biased region may have resulted from any changes occurring in the electrolyte/bulk interface, under the influence of applied voltage.

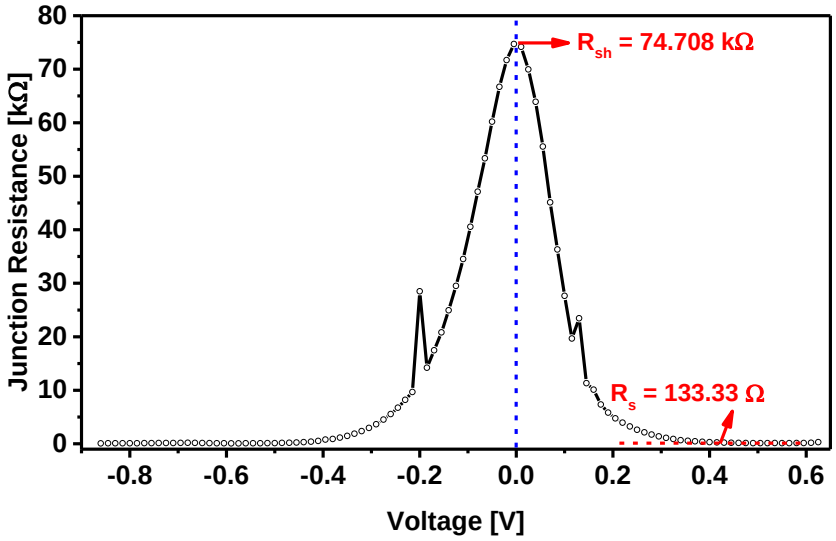

Figure 5-4: Graph between junction resistance and voltage, presenting the values of R_{sh} and $R_{s,}$

Indeed, the transportation of charge carriers in semiconductor diodes involves a series of different conduction mechanism. These mechanism are usually described using a double log I–V graph, in terms of various transport regimes, namely; ohmic, space charge limited current (SCLC) and trap charge limited current (TCLC) regimes. In ohmic region,

the current is directly proportional to the applied voltage. In the case of SCLC region, a quadratic relationship exists between current and voltage. This region can be noticed in two situations i.e. with partially filled traps (trapping parameter: $\Theta < 1$) or fully filled traps ($\Theta = 1$) [133]. TCLC regime exists in-between the ohmic and SCLC region with a V^n dependence of current density on voltage. The double logarithmic *I–V* plot is shown in the inset of Figure 5-5. Varied slopes of different regions signified that the conduction mechanism altered with the applied potential difference. The transition between the regions can also be seen clearly. At voltage levels, lower than the turn-on voltage (V_T) the slope of the characteristic curve was found to be 1.8. Due to the small magnitude of the applied voltage in this region, the number of injected electrons was lower than the number of thermally generated electrons [134]. As a result, the injected electrons were incapable of filling any of the traps located in the organic semiconductor layer. Thus, the injected carriers skipped between the deepest energy traps, making the current almost proportional to the applied potential difference. With further increase in the biased voltage, the slope increased to 3.97, indicating a V^n dependence of current on voltage. Therefore, the region (ranging from 0.17 V to 0.38 V) can be regarded as TCLC region. The higher magnitude of applied potential difference resulted in an increased number of carriers being generated, that might have filled the lower energy traps, facilitating the transport of additional carriers in higher energy traps and thus resulting in a higher current (to voltage) increasing ratio. The slope of the third and final region turned out to be ~2, representing an SCLC region, where all the traps got occupied with the carriers being transported in the organic material without any restriction. The only entity that limited the carriers' transportation is the space charge.

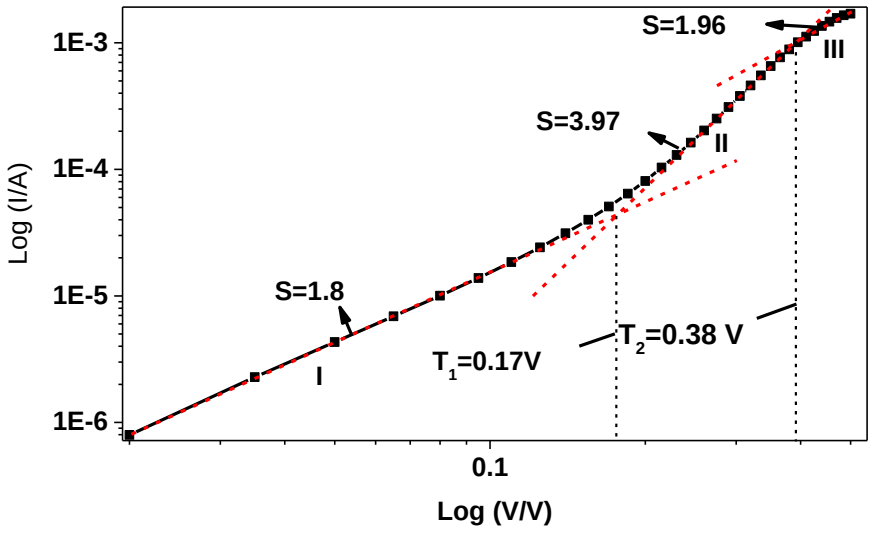

Figure 5-5: The log I-log V characteristics of the cell.

In SCLC region, the charge transport mechanism can be explained by using the Child's law (Eq. 5.2).

$$J = (9\varepsilon_s\theta\mu V^2)/8d^3 \qquad \text{.....(5.2)}$$

where, J is the current density, ε_s is the permittivity, θ is the trap factor, μ is the mobility and d is the film thickness, respectively. The trap factor "$\theta = \frac{J_1}{J_2}$" is defined as the ratio of current densities at the beginning and at the end of the square law region, and its value can be calculated from the ratio of current density values J_1 and J_2, lying at the

beginning and end of region III, respectively [135]. Using Eq. 5.2 the mobility (μ) was calculated which turned out to be equal to 25.47 $\mu m^2 V^{-1} s^{-1}$.

5.3.2 Photo-sensor characteristics:

Initially, the current and voltage characteristics of the sensors were measured and plotted with respect to varied irradiance levels, Fig. 4(a). As seen, the magnitude of generated current increased linearly from 0.1 mA to 0.6 mA. When the photo-sensor was illuminated, e–h pairs generated in the P3HT, got diffused into the P3HT:PCBM blend interface and were split apart due to the built-in electric field. As known, the HOMO level of PCBM is lower as compared to P3HT, thus the holes are transferred from P3HT to PCBM and later to the electrolyte, finally reaching to the respective electrode. A similar explanation can be given for the electron transportation. This difference between the HOMO level of PCBM and P3HT was the main reason behind the upsurge in the number of excited electrons produced, thereby enhancing the photocurrent generation, with respect to increased irradiance levels [136]. The trend of increased photocurrent followed, until a saturation point was reached i.e. maximum number of photoelectrons was being produced, and transferred to the photo-anode. In the case of open circuit voltage (V_{oc}), a similar trend was noted.

To analyse the hysteresis in I_{sc} and V_{oc}, forward and reverse step irradiance measurements were performed. Initially, the irradiance was increased from 11 mW cm^{-2} to 100 mW cm^{-2} (forward) and the resultant I_{sc} and V_{oc} values were noted, Figure 5-6 (a). The same procedure was applied in reverse, with the irradiance decreasing from 100 mW cm^{-2}

to 11 mW cm^{-2}. When taking measurements in ascending order, the current was seen to rise in a linear fashion, Figure 5-6 (b). However, the diode started deviating from the ascending irradiance part, owing to the fact that the diode remained saturated till 80 mW cm^{-2}. At 80 mW cm^{-2} irradiance level, maximum difference of 65.32 mA was observed. This difference began to diminish as the irradiance was further decreased, until the two lines converged at the 11 mW cm^{-2}. A linear trend was also noticed for the forward and reverse V_{oc} vs. illumination cycles, Figure 5-6 (c). However, the voltage saturation at higher irradiance levels (i.e. 90 mW cm^{-2} and 100 mW cm^{-2}) was seen. In contrast to the current measurements, lower V_{oc} levels were observed in the reverse cycle. Further, the difference between the V_{oc} values among the two cycles started increasing for reduced irradiance values and this difference reached the highest value at 11 mW cm^{-2} irradiance.

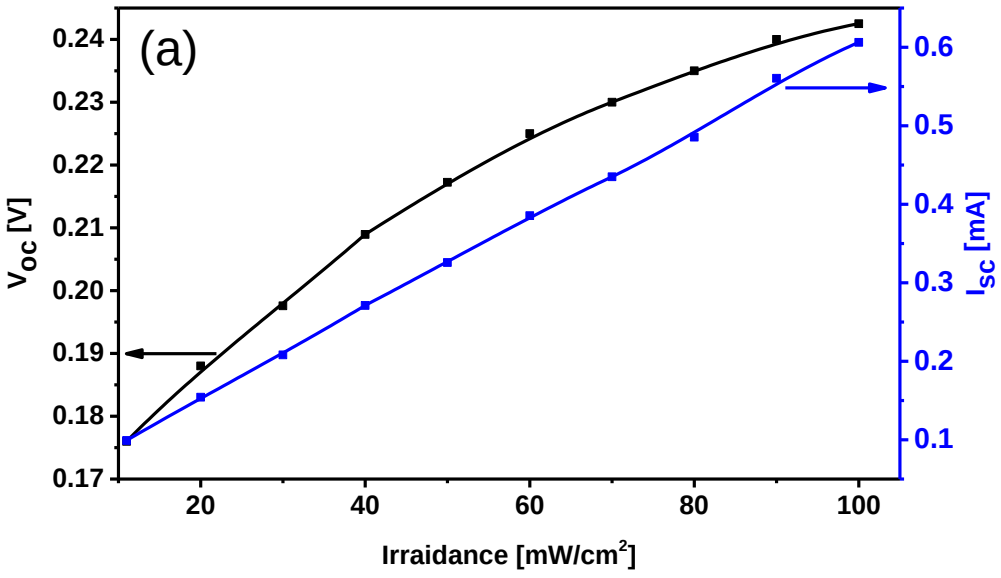

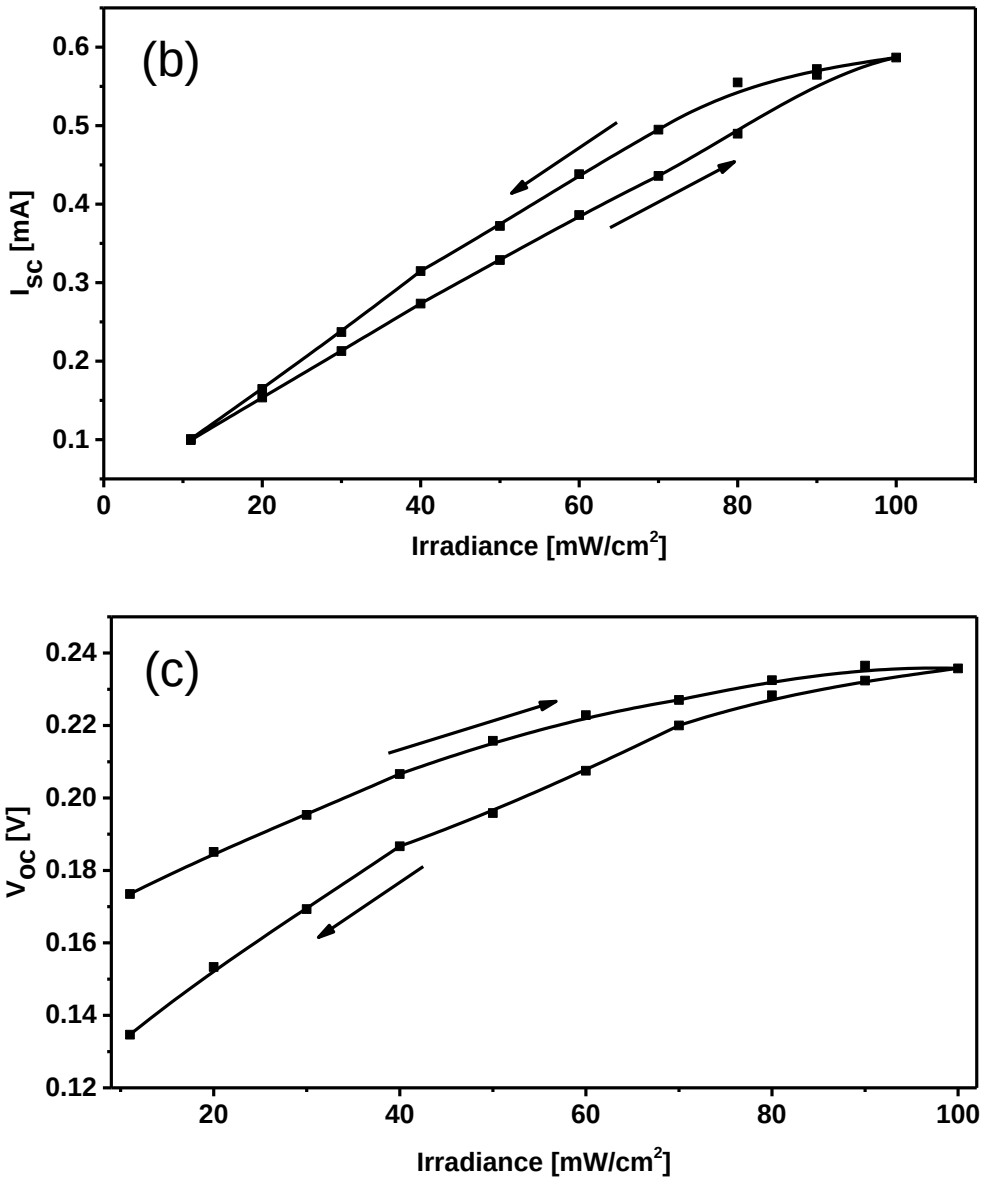

Figure 5-6: (a) I_{sc} and V_{oc} values measured at different irradiance levels ranging from 11 mW cm^{-2} to 100 mW cm^{-2}, (b) I_{sc} values with respect to ascending and descending irradiance levels, (c) V_{oc} values with respect to ascending and descending irradiance levels.

Figure 5-7, shows the photocurrent produced as a function of time under the illumination and dark conditions when 0.15 V potential difference was applied. As seen from the figure, when the sample got excited in the presence of light, a spike was generated indicating the generation of both types of charge carriers. One species of the charge carrier produced recombined at the respective electrode, whereas the other travelled through the active area at a constant velocity, resulting in the plateau region in the transient curve. When the light was ceased, the number of electron–hole pair generated sharply declined, resulting in a tail in the transient current. With the passage of time, the number of charge carriers (generated upon illumination) started to decrease. In the second cycle the current peaked at a relatively lower value, and started stabilizing comparatively quickly. The subsequent transient cycles were almost identical in nature, with an average peak current (measured after stabilization) equal to 0.18 mA. For the stable current cycles, an average transient time constant of 0.43×10^{-3} was found by measuring the slope of the transient cycle's tail area. The response time (t_s) and reset/recovery time (t_c) which are defined as the time required for the photo-current to reach a stable peak value and vice versa, were found to be 0.35 s and 0.23 s, respectively. Further, the responsivity (R) which is the ratio of the photocurrent to illumination power, in the photoconductive mode, was found to have an average value of 1.03×10^{-7} A W^{-1}. To determine photoconductive sensitivity, Eq. 5.3 was used [10].

$$S = \frac{I_{ph} \times T}{P \times A \times V} \qquad \text{……..(5.3)}$$

where I_{ph} is the photo-current generated, T is the thickness of the device, P is the power of the incident light, A is the active area of the diode and V is the applied voltage. The sensitivity was found to be equal to 0.17 μS m W^{-1}. It is evident from the obtained parametric values, that apart for reasonable sensitivity and responsivity values, the samples also showed prompt changes in photocurrent states, as a function of transient irradiance input. Since such photodiodes exhibited a maximum absorption in the wavelength range between 400 nm and 650 nm therefore the sensor implemented is suitable for application related to the detection of light in the visible spectral region [137].

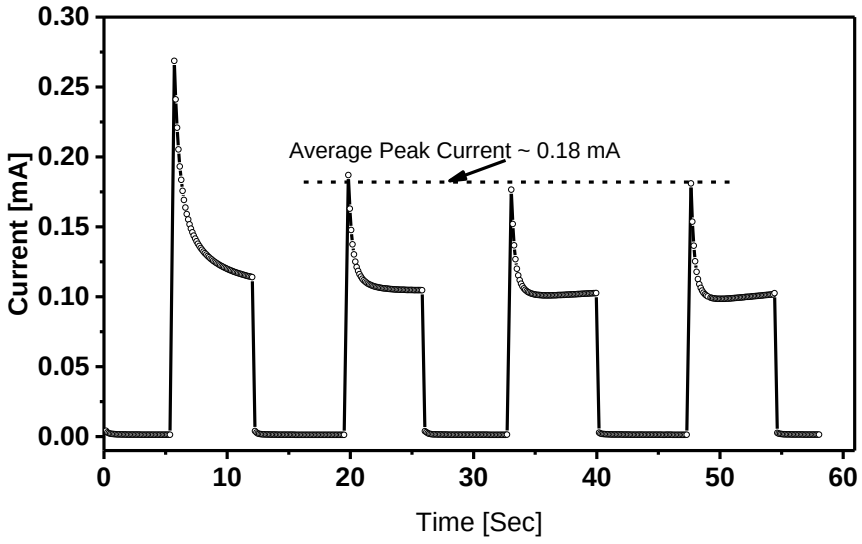

Figure 5-7: Transient response of the photo-detector.

5.4 Conclusion:

This chapter presented a new type of hybrid DSPS configuration based on BHJ thin film and a liquid electrolyte intermediate layer. When measured, the I–V characteristics exhibited a non-linear, asymmetric rectification behaviour. The R_s and R_{sh} resistance values turned out to be 120.19 Ω and 74.71 kΩ, respectively. Under illumination, the photodiodes depicted reasonable photosensitive characteristics with open circuit voltage (V_{oc}) and short circuit current (I_{sc}) varying in a linear fashion with respect to stepped irradiance. Further, the sensors were noted to have a prompt response to any changes in irradiance. The response time and reset/recovery time were found to be 0.35 s and 0.23 s, respectively. These results depict that the new hybrid photo-diode sensor works in an efficient way and can be considered a promising contender in the photo-detection industry.

Chapter 6: Application of CuNWs Based Counter Electrode in DSPS

6.1 Introduction:

When considering counter-electrode for DSPS application, it typically contains a metal oxide layer as a conductive medium and a catalyst layer for efficient charge transportation. Presently, ITO substrate having a Pt coating is the most predominantly utilized counter-electrode configuration used in DSPS assembly. However there are a couple of drawbacks associated with its usage owing to the fact that rare and expensive materials (i.e. ITO and Platinum) are utilized in its manufacturing. In addition, it also exhibits brittleness and thus cannot be rendered suitable for applications requiring flexibility i.e. wearable devices.

Efforts have been made to develop alternative electrode technologies that could exceed the characteristics of ITO, in terms of conductivity, transparency and mechanical performance. The most promising materials currently being researched are metal nanogrids, carbon nanotubes, random networks of metallic nanowires and graphene films [138]. When considering randomly scattered networks, silver nanowires have attracted attention due to their high transparency along with a sheet resistance that is similar to ITO. However, mass production of silver nanowires (AgNWs) based optoelectronic devices is a big challenge because of the high cost of silver. Copper nanowires (CuNWs) can be considered a viable alternative to AgNWs, since they are a 100 times cheaper, are flexible and exhibit high transparency [138, 139]. Further, copper is as conductive as silver, with a bulk resistivity of 1.67 nΩ m as compared to 1.59 nΩ m of silver. These features make CuNWs based electrodes a promising candidate for its incorporation in DSPSs assembly,

as a counter-electrode. However, problems like oxidation and tarnishing that lead towards the instability of CuNWs, pose a serious threat to the wide spread of this technology and thus require addressing [140].

This chapter deals with the fabrication and successful integration of inexpensive CuNWs based counter-electrode in DSPSs, thus replacing the ones based on ITO/Pt configuration. In order to do so, CuNWs were synthesized and deposited onto glass substrate. Later, layers of rGO and PEDOT:PSS were deposited for the purpose of environmental protection and reduction of the root mean square (RMS) roughness of the electrode's surface. In the end, the fabricated TCE was integrated within DSPS, as a counter-electrode and characterized for its performance using various sets of equipment.

6.2 Synthesis and Characterization of CuNWs:

In order to synthesize CuNWs a single step solution based process mentioned by Guo et al was adopted [141, 142]. In short, 1.6 mmol copper chloride ($CuCl_2$) along with 0.8 mmol $Ni(acac)_2$ was added in 20 ml oleylamine solution, being stirred using a magnetic stirrer. The temperature of the solution was kept constant at 80 °C until full dissolution was achieved. Later, the temperature was increased to 175 °C and maintained for 10 hours, to attain fully grown copper nanowires. Upon the expiry of the specified tenure, the solution was cooled down and excess hexane was added to solution for the precipitation of nanowires. When characterized for their internal structure using TEM the NWs tend to be solid form the inside, Figure 6-1 (a). While subjected to SEM analysis, the CuNWs yielded a higher aspect ratio (~ 1600) than any of the studies carried out before, with an average length and diameter equal to 75 µm and 45 nm, respectively, Figure 6-1 (b) [138, 143,

144]. This high aspect ratio later helped in the creation of a percolating CuNWs network with enhanced conductivity and transmittance.

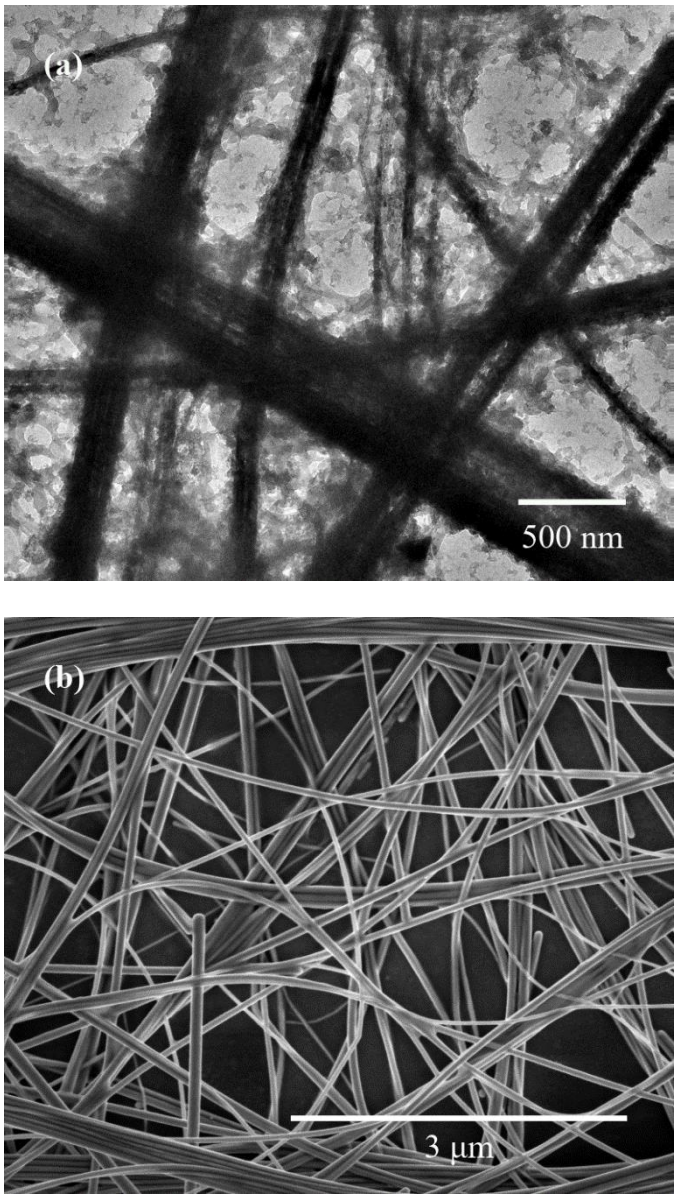

Figure 6-1: (a) TEM Image of CuNWs showing the internal structure, (b) SEM Images of Synthesized CuNWs.

6.3 Fabrication and Characterization of CuNWs Based Counter-electrode:

To start off with the fabrication process, the glass substrates were initially cleaned using the standard cleaning procedure. In order to form a percolating network, the CuNWs were separated from toluene and transferred to IPA solution containing 1 wt% polyvinylpyrrolidone (PVP). The solution was centrifuged in order to wash off excess PVP. Later, the resultant CuNWs with PVP coating were transferred to IPA, which was subsequently used for layer deposition. During the deposition process, the substrates were put on a slightly tilted hot plate with temperature maintained at 70 °C for the prevention of coffee stain effect, which could have proved detrimental for CuNWs homogeneity. The deposited CuNWs network was observed to have been greatly affected by the environment and tended to degrade fast due to their oxidation. The oxidation rate for the CuNWs was observed to be higher as compared to the bulk material due to the larger surface area available to water and oxygen molecules for contact. Hence, addition of an extra layer of protection was found to be necessary for the prevention of CuNWs from getting oxidized. Apart from that, high peaks occurred at points where the nanowires intersected each other, Figure 6-2. This inflation in height increased the likeliness of shortening the subsequent layers, hence hindering the operation of the fabricated device and reducing its performance [145]. Thus making it of key importance to attain a uniform thickness over the whole electrode surface.

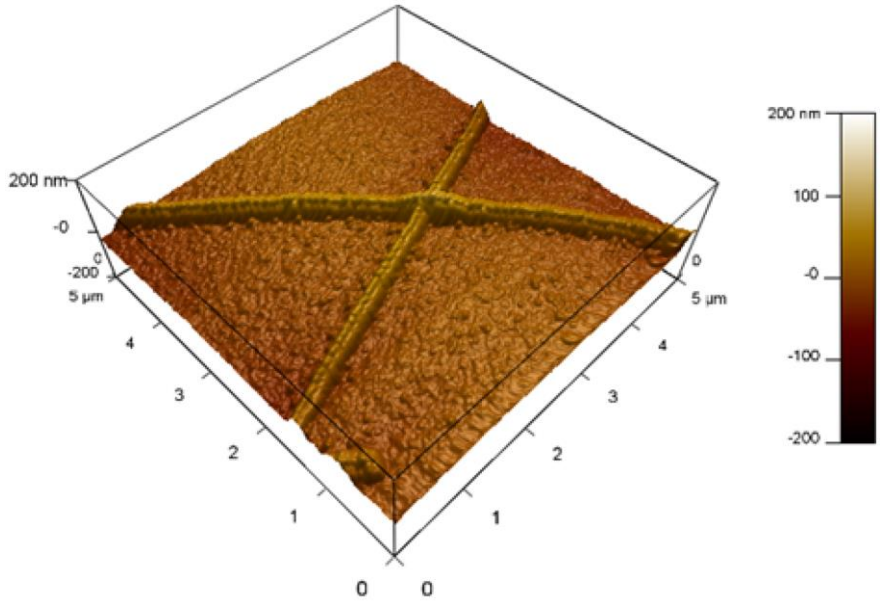

Figure 6-2: 3D AFM image showing the increase in height at the intersection of two nanowires.

6.4 Passivation and Reduction of RMS Roughness of CuNWs Network:

The interatomic spacing between the carbon atoms in graphene/rGO is around 1.42 Å and thus it can provide impenetrability against oxygen and water molecules having diameters of 3.5 Å and 2.7 Å, respectively. In addition, the rGO layer can also provide active sites for I_3^-/I^- electrocatalysis, thereby improving the rate of electron transfer. These benefits make the use of rGO layer on the top of CuNWs, effective. Since the fabrication of pure graphene is expensive therefore an alternative approach was adopted, that relied on the reduction of GO layer. Briefly, GO platelets were separated from their original solution and added to IPA. Later, the solution was used to deposit a layer of GO via spray coating. In order to reduce GO and restore the conductivity of CuNWs (with IPA coating), the

fabricated electrodes were annealed in forming gas environment (95% N_2 + 5% H_2). In addition, the thermal annealing process is also known to bring structural improvements to the deposited rGO layer, eventually resulting in improved conductivity [146]. Although partial reduction was achieved, as indicated by the shift in G band and decrease in the peak intensity ratios of D and G band Figure 6-3 (inset), yet the rGO layer when deposited on top of CuNWs was found to be conductive and completely covered the nanowire network (with the exception of few voids), thus providing active passivation against oxidation (as indicated by the environmental tests in Figure 6-3, without compromising the conductivity of the fabricated electrode.

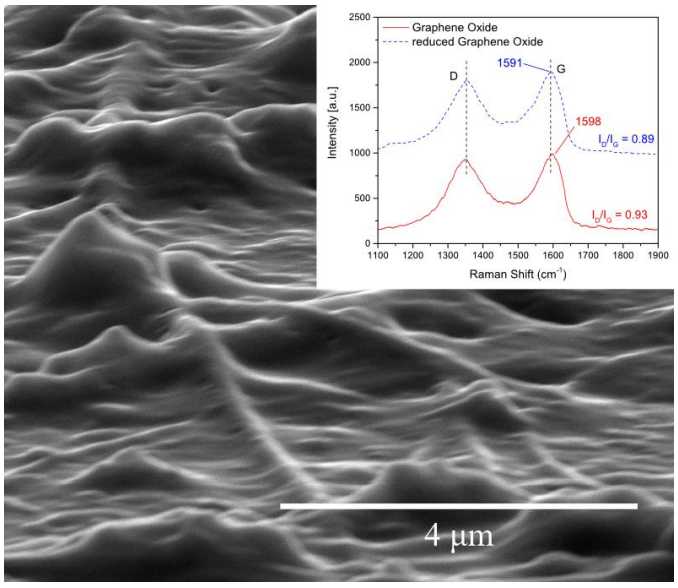

Figure 6-3: Coverage of rGO over CuNWs layer, inset: Raman spectroscopy of GO and rGO layers, deposited on glass substrates.

When characterized for the optical transmittance, both the (CuNWs and CuNWs/rGO based) TCEs depicted a flat transmittance over visible and NIR wavelength range. A decrease of 3.2% was noted in the transmittance (at 550 nm) after the deposition of rGO layer on the top of CuNWs, Figure 6-4.

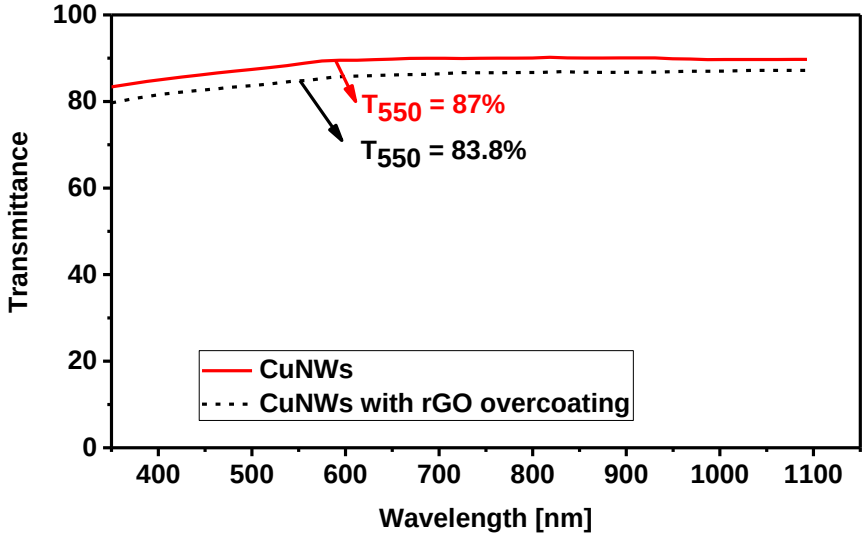

Figure 6-4: Optical transmittance spectra of CuNWs and CuNWs/rGO TCEs as a function of wavelength.

In order to test the effectiveness of the rGO over-coating, stability tests were performed in various environmental conditions. When exposed to ambient environmental conditions for 30 days, the sheet resistance for the CuNWs/rGO electrode configuration remained stable over the course of the test, whereas the sheet resistance of CuNWs samples

was observed to increase constantly, Figure 6-5 (a). A similar trend was noted when the samples were exposed to harsh environmental conditions (80 °C and 80% relative humidity (RH)), for a period of 48 hours. No change in the sheet resistance of the CuNWs/rGO electrodes was observed, whereas on the other hand the sheet resistance of CuNWs based electrodes became double, at the end of the experiment, Figure 6-5 (b).

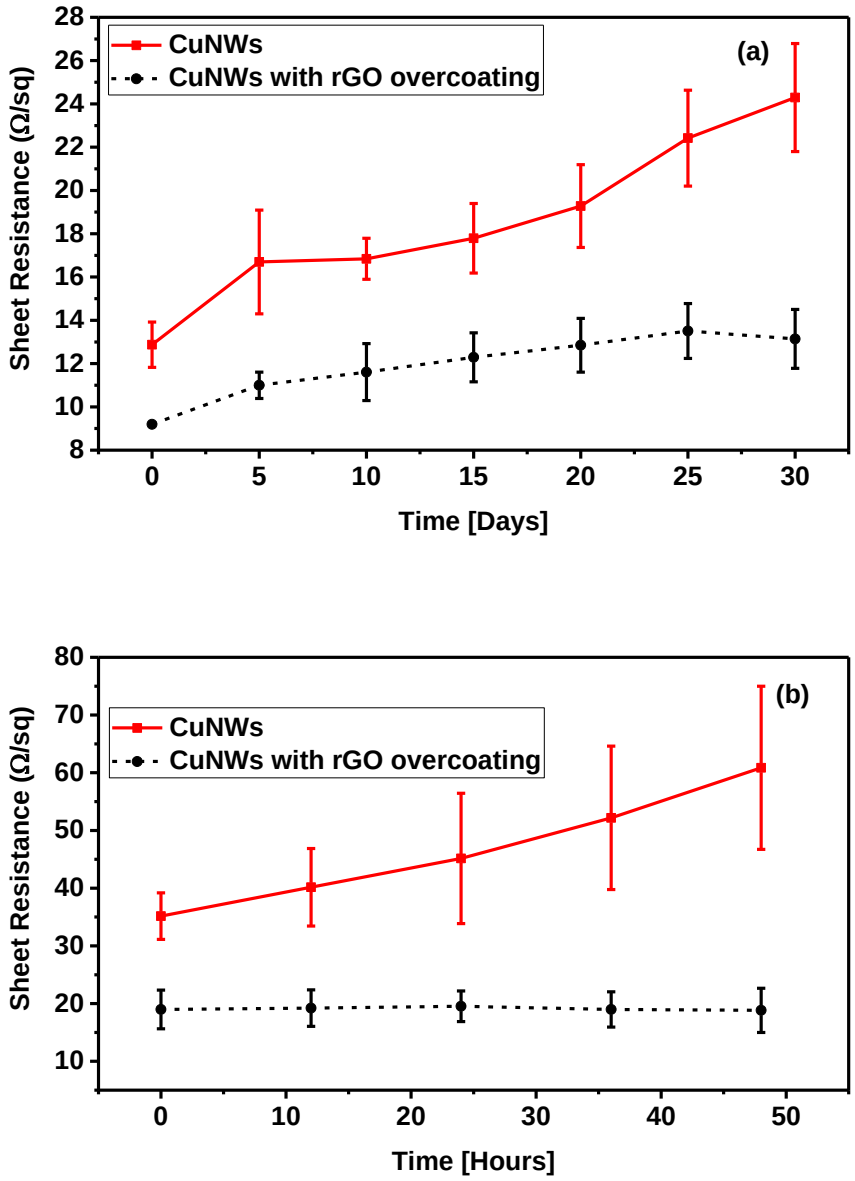

Figure 6-5: (a) Variation in sheet resistance of CuNWs and CuNWs/rGO TCEs when exposed to ambient environment for 30 days, (b) Variation in sheet resistance of CuNWs and CuNWs/rGO TCEs when exposed to harsh environmental (80 °C, 80% RH) conditions for 48 hours.

For the reduction of RMS roughness, PEDOT:PSS was utilized. PEDOT:PSS polymer was heated to 70 °C and then spin coated onto the TCE sample, while being spun at 6000 rpm. Figure 6-6 shows the CuNWs/rGO with a PEDOT:PSS layer over-coating. As depicted in the SEM images gathered at a tilted angle of 10 degrees, PEDOT:PSS entirely covered the underneath CuNWs and reduced graphene oxide layers, thus making the surface smoother.

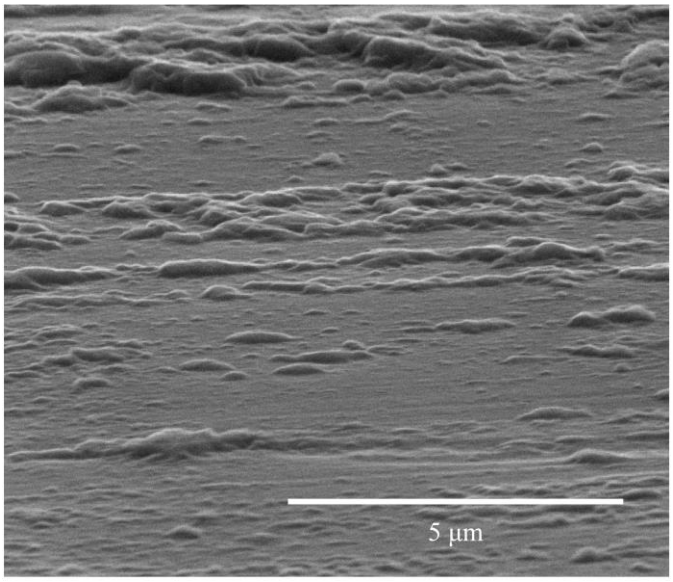

Figure 6-6: Layer of PEDOT:PSS covering rGO and CuNW network layers.

Apart from the prevention from oxidation and reduction in the roughness, the rGO and PEODT:PSS layers also stopped the annealed nanowire intersections from loosening up. The average sheet resistance of the fabricated hybrid electrodes, when checked using four probe method, turned out to be less than 20 Ω cm^{-2}.

6.5 Fabrication and Characterization of CuNWs/rGO/PEDOT:PSS Based DSPSs:

Initially, optimized EPD was used to deposit TiO_2 semiconductor layer on the top of ITO/glass substrate. After the deposition, the substrate was sensitized using N719 and later sintered at 450 °C in a tube furnace. Standard procedures mentioned in Chapter 3, were used for staining the photo-anode and joining it with counter-electrode for DSPS fabrication. A cross-sectional view of the complete DSPS assembly is shown in Figure 6-7.

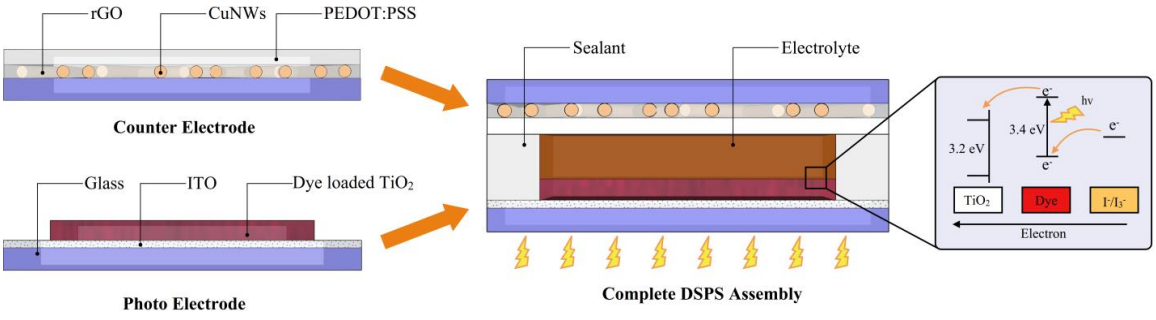

Figure 6-7: Cross-sectional view showing photo electrode and counter-electrode configurations, along with the complete DSPS assembly.

6.6 Photosensor Characterization:

6.6.1 Linearity:

The fabricated hybrid TCEs were integrated as counter-electrode in DSPS devices and were characterized for their photosensor properties. Initially, the DSPSs produced were subjected to varied illumination levels (ranging from ~ 10 000 lux to 100 000 lux) and the subsequent current and voltage values were measured, Figure 6-8. As seen from the current-voltage characteristics plotted at different illumination levels, the photocurrent increased logarithmically with the rise in irradiance level. This is due to the fact that an increased light intensity caused an upsurge in the number of excited dye molecules, which led to an increased number of electron transfers from the dye molecules to the covalently bonded TiO_2 nano-particles, thereby enhancing the photocurrent generation [11]. This trend carried on, until saturation point was reached (i.e. maximum number of electrons were being excited and transferred to ITO via TiO_2 semiconductor layer) making the photo current almost constant, irrespective of light intensity. A logarithmic increase with respect to changes in irradiance level was also observed in case of voltage. The inset in Figure 6-8 depicts the variation in the voltage generated (for seven samples) when multiple measurements were carried out. The average standard deviation of all measurements turned out to be 6.51 mV.

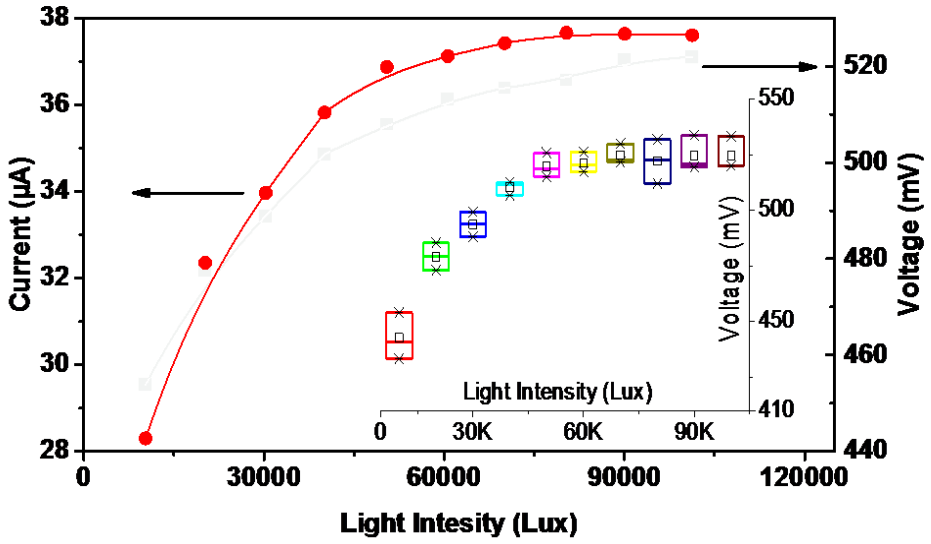

Figure 6-8: The current and voltage versus illumination intensity characteristic of the DSPSs, inset: Variation in open circuit voltage with respect to light intensity, represented by error bars.

6.6.2 Time response:

The photo-response characteristics of the fabricated DSPSs, demonstrated changes in the photocurrent's magnitude as a function of periodic pulses of the simulated solar light. Solar simulator was employed to measure the response and recovery time of the fabricated DSPSs, at an irradiance of 100 mW cm^{-2}. A light pulse spanning over a time duration of 0.5 seconds was applied and the average response (in terms of current generated) towards light was measured (with a forward biased voltage of 1 V), Figure 6-9. The average response time (t_r) and reset time (t_c) obtained from the current v/s time graph, were found to be equal to 118ms and 28ms respectively, making reset time more than 4 times faster as compared to the response time. This is due to the fact that the number of excited dye

molecules steadily rose, when the light was incident upon the DSPSs, whereas the DSPS responded immediately to the absence of light. Overall, t_r and t_c showed that the sensor exhibits rapid changes in states of photocurrent as a function of transient light input.

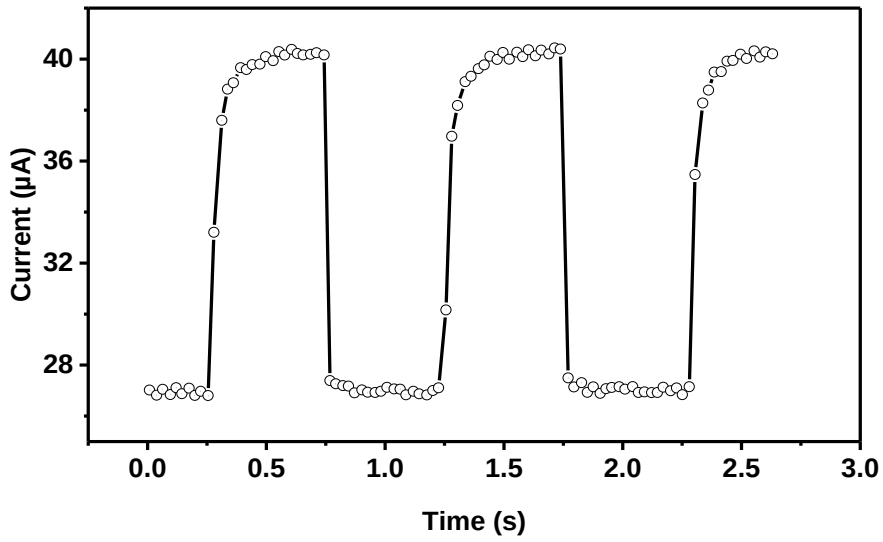

Figure 6-9: Dynamic photocurrent versus time response of the fabricated DSPSs.

The responsivity of the DSPSs is found to be 4.0 x 10^{-4} A W^{-1}. The Photo-conductive sensitivity of a photo diode can be determined by the expression [10]:

$$S = \frac{I_{ph} \times T}{P \times A \times V} \qquad \ldots\ldots\ldots\ldots\ldots\ldots (6.1)$$

Where I_{ph} is the photo-current, T is the thickness of the sensor, P is the power of light, A is the active area of the sensor and V is the applied bias voltage. The Photo-conductive sensitivity of the sensor turned out to be 0.39 μS m W^{-1}.

6.6.3 Hysteresis in open circuit voltage:

Hysteresis is considered as an important factor that needs to be taken into account when calibrating a sensor. Figure 6-10, shows the hysteresis curve of open circuit voltage (V_{oc}) of the DSPS. The average hysteresis value of the curve was found to be 0.011 V as the sensor is exposed to ~10000 lux to 100000 lux and vice versa. The hysteresis effect in V_{oc} started fading away when measurements were carried out after a prolonged exposure of DSPSs, to a certain light intensity.

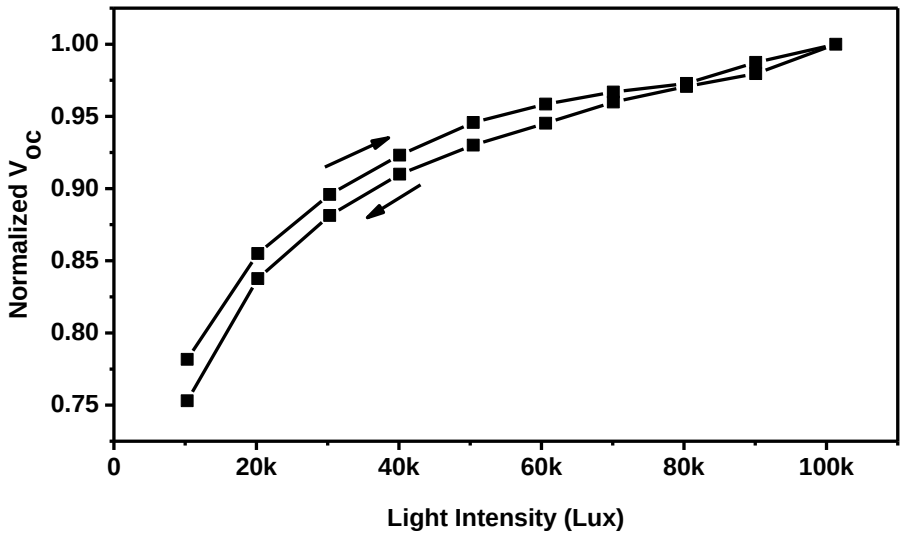

Figure 6-10: Hysteresis curve: V_{oc} as a function of light intensity.

These promising results render CuNWs/rGO/PEDOT:PSS TCE based DSPSs suitable for various photo sensing applications.

6.7 Conclusion:

A new type of transparent conducting electrode configuration consisting of CuNWs, rGO and PEODT:PSS has been fabricated and successfully integrated as a counter-electrode in DSPSs. The responsivity of DSPSs was found to be 4.0×10^{-4} A W^{-1}, whereas the average response time and reset time for these DSPs turned out to be 118 ms and 28 ms, respectively. Thus it can be concluded that the CuNWs/rGO/PEDOT:PSS based transparent conducting electrode could potentially be a viable alternative to the expensive ITO/Pt based cathode in DSPSs.

Chapter 7: Optimization of ITO Glass/TiO2 DSSC Photo-anode for Enhanced DSSC Efficiency

7.1 Introduction:

As discussed before, nano-porous semiconductor layer responsible for dye adsorption and electron transport is the heart of the DSSC [147]. It is of key importance that the deposited semiconductor layer is well packed and offers low resistance to the flow of electrons, generated as a result of excitation of dye molecules. Thus, optimization of various (semiconductor layer related) parameters including thickness, crystallinity and porosity is highly encouraged to increase the power conversion efficiency. The film deposition method employed has a great influence over the key performance and economical parameters (including ones mentioned above) and thus, needs to be chosen carefully. In recent times, EPD process (that relies on the motion of charged particles under the influence of electric field) has attracted a lot of attention owing to the lower cost and temperature requirements, short fabrication time and the ability to effectively control the thickness of semiconductor layer [148]. Apart from the deposition technique, post treatment processes, such as sintering, are also of key importance and play a vital role in enhancing the DSSC efficiency by the creation of vital interconnection between the semiconductor nanoparticles. Optimizing the EPD deposition and subsequent sintering process could lead to a significant increase in a cell's efficiency and thus can play an important role in the commercialization of the DSSC technology.

This chapter focuses on enhancing the efficiency of DSSC by utilizing and optimizing EPD deposition technique, alongside sintering process involved in the fabrication of TiO_2 based photo-anode. To do so, a semiconductor layer was deposited on glass substrates under the influence of an electric field, formed at varied voltage levels ranging from 2.5 V_{DC} to 7.5 V_{DC}. Later, the samples were sintered (using either single step or two step sintering process), dye stained and integrated within DSSCs. Morphological and electrical characteristics of the fabricated photo-anode/DSSC were measured using various sets of equipment and eventually analysed.

7.2 Fabrication of TiO_2 Photo-Anode Using EPD:

Initially, to prepare a TiO_2 suspension for EPD, 3 g of TiO_2 (P25) was added to 60 ml ethanol, along with a small amount of acetylacetone. The solution was stirred for 24 hours, to achieve a homogeneous blend without any clumps. A charging solution was prepared separately by dissolving 63 mg of iodine in a solution containing 250 ml ethanol, 10 ml acetone and 5 ml deionized water. Prior to the deposition, the TiO_2 suspension was added to the charging solution and sonicated for 15 minutes. For the semiconductor film deposition, charged TiO_2 solution was poured into a specially designed vessel, Figure 7-1 (a). Later, two ITO coated glass slides were immersed vertically into the vessel, with one acting as an anode and the other acting as a cathode. The distance between the two electrodes was kept constant at 0.8 cm. Various voltage levels ranging from 2.5 V to 7.5 V were put to trial, while keeping the current constant. Upon the application of a potential difference, the negatively charged TiO_2 nanoparticles started traveling towards the anode, indicating an anodic EPD process, Figure 7-1 (b). The ITO based anode was allowed to sit

in the vessel for 60 seconds, before being taken out and dried in ambient environment for 30 minutes.

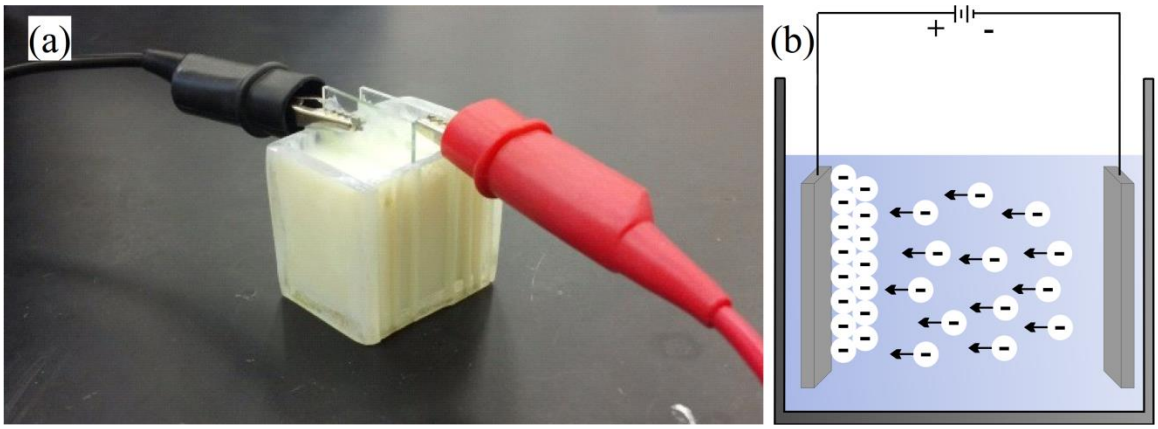

Figure 7-1: TiO_2 deposition on ITO coated glass substrate using EPD (real image), (b) EPD deposition schematic.

To complete the photo-anode fabrication process, the films were subjected to either a single step or two step sintering process (in a tube furnace), to obtain crystallized TiO_2 layers with enhanced nanoparticle interconnectivity. In the case of single step sintering process, the samples were subjected to a temperature of 450 °C for 30 minutes. The two-step sintering process required samples to be initially sintered at 350 °C for 1 hour, followed by sintering at 450 °C for 30 minutes. For assembling a DSSC, standard procedures mentioned in Chapter 3 were adopted.

7.3 Characterization of Photo-Anode and DSSC:

7.3.1 Effect of variations in EPD voltage:

Figure 7-2 (a), shows the *I-V* characteristics of DSSCs containing TiO_2 layer deposited at different voltage levels, along with the External Quantum Efficiency (EQE) spectrum of the N719 dye based DSC (inset). As seen, the highest values for I_{sc} and V_{oc} were obtained for semiconductor layer deposited at 5 V. Figure 7-2 (b) shows the cross-sectional SEM images of the samples prepared at 2.5 V, 5.0 V and 7.5 V for 60 seconds. The thickness of the TiO_2 layers were found to be 3.5 ± 0.5 µm, 17 ± 2 µm and 33 ± 1.5 µm, respectively.

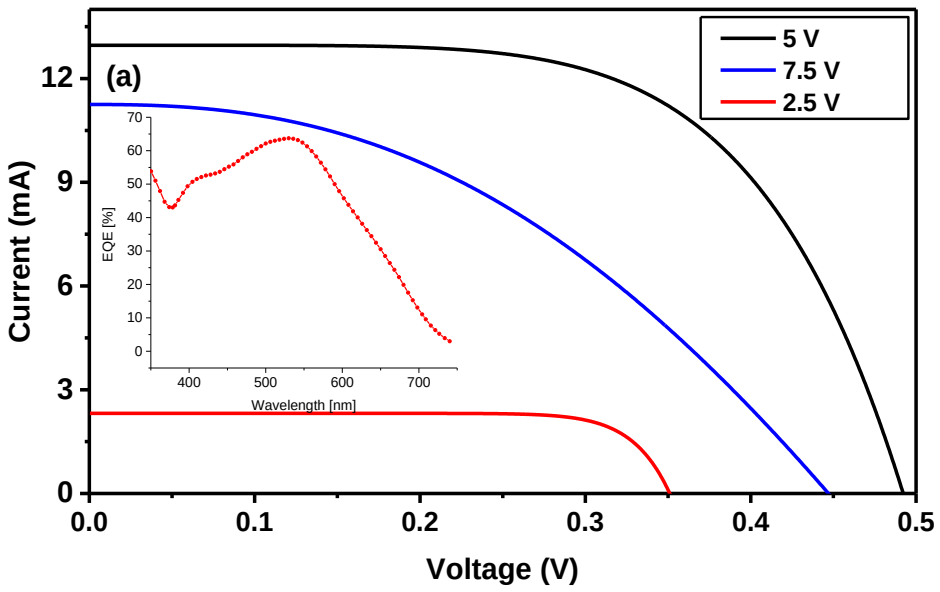

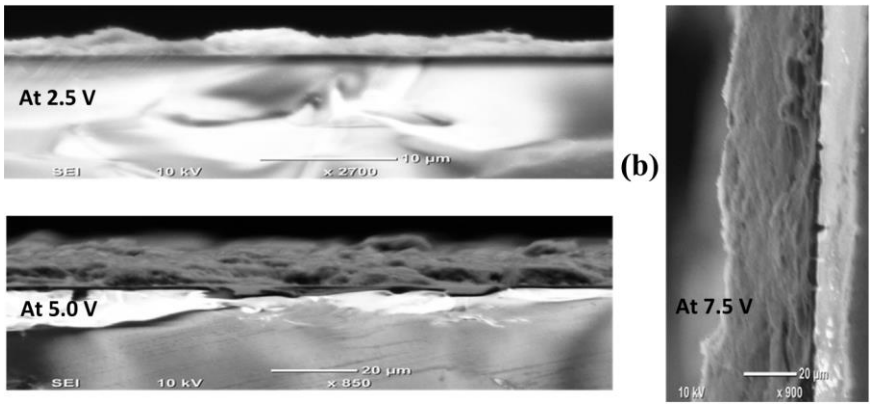

Figure 7-2: (a) I-V curves for DSSCs containing semiconductor layer deposited at different time stamps, inset: EQE spectrum of N719 Dye, (b) Cross-sectional SEM images of the samples prepared at 2.5 V, 5.0 V and 7.5 V for 60 seconds.

One of the key parameters affecting the performance of the DSSC is the terminal velocity (V_t) of the of the particles in the EPD suspension, which is defined by Eq. 7.1.

$$V_t = \frac{\varepsilon \xi E}{4\pi \nu} \qquad \ldots\ldots\ldots\ldots\ldots\ldots (7.1)$$

Where ε is the dielectric constant of the liquid, ξ is surface change density of the particle in the solvent, ν is the viscosity of the solvent and E is the applied potential difference [149].

If the solvent remains the same, and ε, ξ and ν remain constant, E becomes the sole variable parameter responsible for changes in V_t. Increasing the applied voltage will result in an increased V_t, which in turn will increase the TiO_2 deposition rate and vice versa. Thus,

the thickness of the semiconductor layer deposited increases with the increase in the applied potential difference. Therefore, thin TiO_2 semiconductor layers deposited at 2.5 V led to lower dye absorption and thus lower electron generation, eventually resulting in lower efficiency. Conversely, thicker TiO_2 layer deposited at 7.5 V resulted in more dye loading, however, it also led to limited electron transport due to the increased path length, less ordered structure, low packing density and more trap states which are responsible for the recombination of electrons [149, 150]. The films deposited at 5 V presented an optimized film thickness, leading to a free transfer of electrons from particle to particle and thus increased I_{sc}. The increase in the V_{oc} can be attributed to two reasons: (1) retardation of the recombination between the electrons and electrolyte ion species, and (2) band edge movement of the semiconductor with respect to the redox potential [151].

Table 7.1 summarizes the values of major electrical parameters obtained for the semiconductor layers, deposited at various voltage levels. As seen, fill factor (*FF*), which is the measure of the squareness of the I-V curve, decreases with the rise in EPD voltage level. This is attributed to the increased thickness of TiO_2 at higher voltage levels, which eventually resulted in the rise of internal series resistance. The efficiencies for the layers deposited at 2.5 V, 5 V and 7.5 V turned out to be 0.59%, 4.2% and 2.02%, respectively.

Table 7-1: Photovoltaic parameters for DSSCs containing semiconductor layer deposited at different time stamps.

	2.5 V	5 V	7. 5 V
J_{sc} (mA/cm^2)	2.5	13.8	11.1
V_{oc} (V)	0.35	0.48	0.46
V_{mpp} (V)	0.32	0.40	0.20
J_{mpp} (mA/cm^2)	1.8	10.5	10.1
P_{mpp} (mW)	0.59	4.20	2.02
FF (%)	69.51	63.86	42.1
η (%)	0.59	4.20	2.02

Figure 7-3 shows the SEM images gathered for semiconductor layer deposited at 5 V. The highest efficiency obtained was the result of an optimized/homogenized pore density as compared to the rest of the samples, which is essential for achieving maximum dye loading, required for superior performance of DSSC. ImageJ, an open source image processing and analysis software, was utilized to determine the average pore size and layer thickness of the deposited TiO_2 layer. The average diameter of the pores for semiconductor layer deposited at 5 V turned out to be ~30 nm.

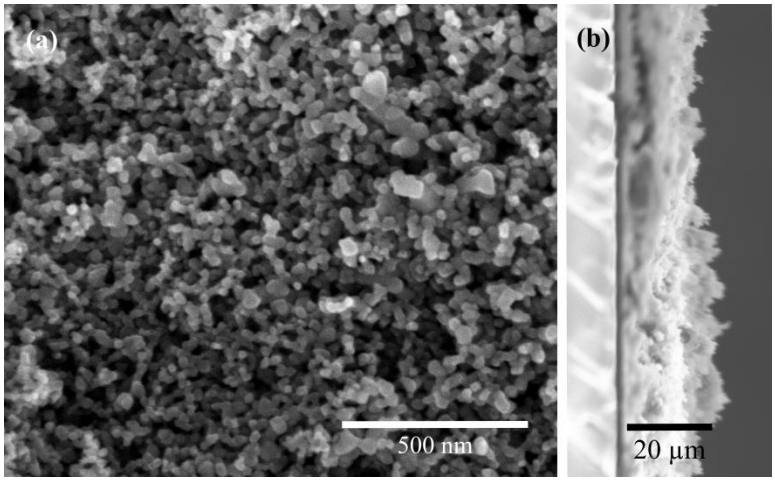

Figure 7-3: (a) SEM image of TiO_2 semiconductor layer deposited at 5 V for 60 seconds. (b) Cross-sectional SEM image of semiconductor layer deposited at 5 V.

7.3.2 Effect of varied sintering process:

Earlier studies have indicated that the sintering profiles used for the TiO_2 semiconductor films have a significant effect on key performance parameters [72]. After the optimization of the EPD process, efforts were diverted towards the optimization of the sintering process. As discussed before, two sintering processes were put to trial and a comparison was established (between the two variants), while keeping the EPD voltage constant at 5 V. In the single step sintering process, the samples were sintered at 450 °C for 30 minutes. Whereas in case of two step sintering process, the samples were initially sintered at 350 °C for 1 hour, followed by sintering at 450 °C for 30 minutes. The two step sintering process produced a lower I_{sc} and a slightly higher V_{oc}, as compared to the single step sintering process, Figure 7-4. After the initial optimization of the EPD process, DSSC

samples (12 in total) were fabricated and divided into two groups (i.e. single step and two step sintered cells) and characterized using the solar simulator. The cells showed similar characteristics (within each group) in terms of the I_{sc}, V_{oc}, *FF* and efficiency, thus confirming the reproducibility of the results obtained as shown in the inset of Figure 7-4.

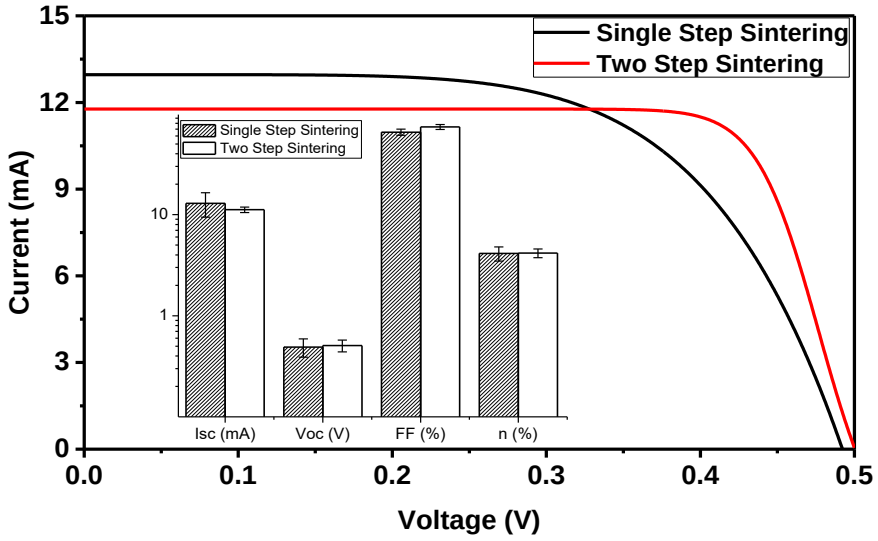

Figure 7-4: I-V curves for DSSCs containing TiO_2 layer sintered using single step and two steps sintering methods. Inset shows the photovoltaic parameters for single step and two step sintered electrodes.

Table 7.2, presents a comparison of various performance parameters for single step and two step sintering processes employed. As seen, the two-step sintering process resulted in an increased *FF* i.e. ~70%, eventually resulting in a slightly increased efficiency (4.5%)

of the DSSCs. According to Huo et al. [152], when employing high temperature single step sintering (at 450 °C), the nucleation and growth of TiO_2 crystals does not get restricted, resulting in large nanocrystal aggregates. On the other hand, in case of two steps sintering, the initial low temperature exposure (in two step sintering) allowed only a portion of anatase nuclei to form, preventing its conversion to sizeable nanocrystal aggregates. This, in turn, enhanced the conductivity (charge transport properties) of TiO_2 layer. However, in the case of two step sintering the value of I_{sc} is lower than that of one step sintering case. This might be due to the different sizes of nanocrystal aggregates, which affect the dye loading and hence the I_{sc} value.

Table 7-2: Performance parameters for the DSSCs containing semiconductor layer sintered using single step and two steps sintering methods.

	5 V-60 s (450 °C)	5 V-60 s (350 °C, 450 °C)
J_{sc} (mA/cm^2)	13.8	12.6
V_{oc} (V)	0.48	0.51
V_{mpp} (V)	0.40	0.40
J_{mpp} (mA)	10.5	11.3
P_{mpp} (mW)	4.20	4.52
FF (%)	63.86	70.03
η (%)	4.20	4.52

For the stability analysis, the DSSC samples were kept in the ambient environment for 100 hours, after the initial I-V characterization. After the first 50 hours, the DSSCs showed no signs of degradation in terms of efficiency as shown in Figure 7-5. Upon measuring the I-V curves at an interval of 25 hours, it came to notice that the cell's efficiency took almost 35 hours to stabilize; at 75% of the initial value. No decrease in the efficiency was observed, afterwards. The electrodes were also characterized using electrochemical impedance spectroscopy (EIS). The Nyquist plots have been given in the inset of Figure 7-5. As seen, each of the generated EIS curves comprised of a depressed semi-circle (at both high and low frequencies) followed by a linear trail at lower frequencies. $Z`$ and $Z``$ appeared to have the lowest value at 100 kHz, and their values increased with the decrease in AC voltage frequency. The data set obtained was fitted using a full Randles equivalent circuit shown in the inset, Figure 7-5 (inset) [153]. The total ohmic resistance (R_{ohm}) that is composed of solution resistance (R_s) and charge transfer resistance (R_{ct}) at the electrode/electrolyte interface, were determined by the intercept of the semi-circle plot with the x-axis. The R_{ohm} for the single and two steps sintered electrodes turned out to be ~78.80 Ω and ~71.74 Ω, respectively. The two step sintering plot has a curve with a lower diameter as compared to the single step plot, indicating a lower charge transfer resistance. Thus, it can be said that the interconnection between TiO_2 nanoparticles of two step sintered semiconductor layer offers less resistance to the electrons generated as a result of dye excitation.

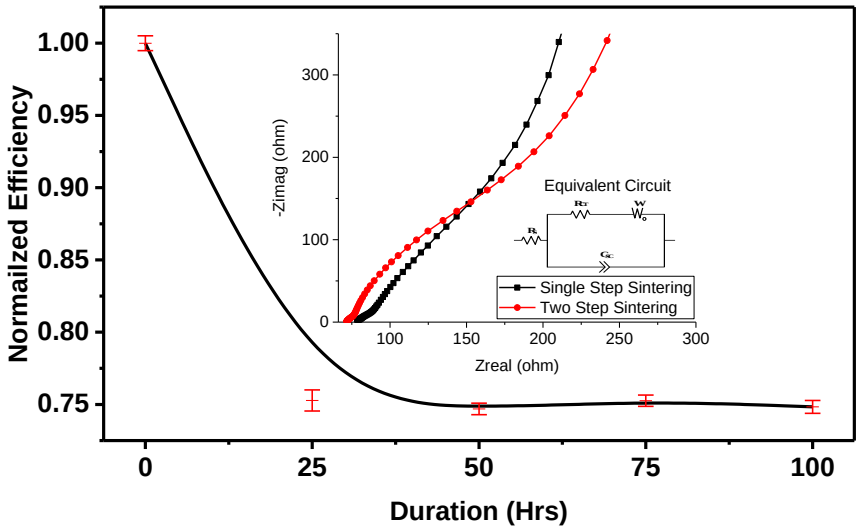

Figure 7-5: Stability of the fabricated DSSC over the course of 100 hours, inset: Nyquist plots establishing a comparison between the impedance of single step and two step sintering processes.

Lastly, it is important to note that DSSC fabrication procedure followed involved a binder free EDP process with no additional compression steps pursued, making it preferable over DSSCs fabricated using relatively complex methods but yielding similar efficiencies.

7.4 Conclusion:

The current chapter dealt with the optimization of DSSC's performance, by fine tuning semiconductor layer deposition and sintering processes. When establishing a comparison amongst DSSC containing photo-anodes deposited at various EPD voltage levels (ranging from 2.5 V to 7.5 V), highest efficiency of 4.2% was achieved for the film deposited at 5

V_{DC}. The efficiency further increased to 4.5% when the single step sintering process was replaced with a two-step sintering process.

Chapter 8: Summary and Future Work

8.1 Summary:

The integration of organic materials in opto-electronic devices has led to the generation of wide range of innovative applications ranging from flexible displays to lightweight or semi-transparent solar cells. When considering photovoltaic and photo-sensory applications, dye-sensitized and bulk heterojunction devices have shown great promise in reducing down the costs related to materials and manufacturing processes. This thesis dealt with fabrication, characterization and optimization of photo-detection and photovoltaic devices that are based on thin (dye-sensitized and bulk heterojunction) active layers.

Tests were conducted to enhance the diode and photo-detection properties of dye-sensitized devices by means of co-sensitizing N719 dye with a newly synthesized organic dye called AS-2. Initially, absorbance measurements for the devices were carried out using a spectrophotometer. Then, the two dyes were mixed together in various proportions and used for sensitization of TiO_2, later to be used in dye sensitized photosensor (DSPS) assembly. When establishing a comparison with N719 based DSPSs, the ones based on dye cocktail having a mixing ratio of 0.25 (AS-2):1(N719) were found to have reduced leakage currents and higher breakdown voltages. Further, when it comes to photodetection properties, they exhibited comparatively better linearity at a higher irradiance level.

Photo-detective properties of a newly hybrid DSPS/BHJ configuration were also investigated. Initially, a thin layer of P3HT:PCBM (1:1) was deposited onto a glass

substrate. Then, the fabricated photoanode was integrated into a photo sensor containing a liquid electrolyte intermediate layer residing between the counter-electrode and photo-anode. The measured *I-V* characteristics resembled to that of a rectifier with a non-linear, asymmetric behaviour. In addition, the photodiodes depicted well-suited photosensitive characteristics with open-circuit voltage (V_{oc}) and short-circuit current (I_{sc}) varying linearly with respect to irradiance. The response time (0.35 seconds) and reset time (0.23 seconds) were also found to be residing within the range suitable for photosensor, thus rendering the newly developed hybrid configuration a promising contender in the photo-detection industry.

Efforts were also made to replace ITO counter-electrode, which apart from having key advantages such as high electrical conductivity and optical transmittance, had some major drawbacks related to the cost and scarceness of materials employed. In this thesis, we proposed an alternative counter-electrode configuration based on randomly scattered CuNWs network. Initially, CuNWs were synthesized and deposited on various substrates via spray coating. Subsequently, layers of rGO and PEDOT:PSS were also deposited for the purpose of environmental protection and reduction of root mean square (RMS) roughness. When characterized, the fabricated electrode exhibited long-term (ambient environment) stability and extreme resilience towards any changes under harsh environmental conditions. When integrated within the dye-sensitized photodetector, the CuNW/rGO/PEDOT:PSS based counter-electrode produced superior results in terms of response time, reset time and responsivity.

Concerning dye-sensitized solar cells (DSSCs), a novel technique known as electrophoretic deposition (EPD) having number of advantages (e.g. short deposition time

and no binder requirement) was utilized and optimized for the preparation of TiO_2 photo-anode with uniform layer thicknesses. To achieve this, various EPD voltage levels ranging from 2.5 V to 7.5 V were investigated. In addition, novel techniques related to the post-deposition sintering process were also developed. Upon characterization, changes to EPD voltage levels and sintering processes were found to have a profound effect on various aspects like film thickness and/or morphology of the photo-anode. When integrated within DSSCs, the photo-anode deposited at 5 V_{DC} produced a power conversion efficiency of 4.2%. This efficiency further increased to 4.5% when the single-step sintering process was replaced by two step sintering process.

The research presented in this thesis was aimed to contribute in the improvement of organic opto-electronic devices. The results achieved hold promises in fostering a great deal faster market penetration and commercialization of organic opto-electronics.

8.2 Future Work:

Due to time constraints, this work has focused on few aspects of organic opto-electronics, however, as for any scientific research, results open new challenges for other researches to capitalise on and contribute for further improvements. In this regard, few suggestions have been made in the upcoming sections. The suggestions made here are by no means restrictive nor incorporate all the possible directions; it is rather an open-ended problem.

Co-sensitization of N719 using newly a developed dye (i.e. AS-2) has been carried out to bring improvements to the photo-detection properties of DSPS. The same process

can be applied to bring improvements to the photovoltaic parameters and enhance the efficiency of DSSCs. In order to do so, one can use a cocktail of various dyes having absorption peaks spread throughout the NIR and visible spectrum.

The configurations implemented in the current thesis utilize a liquid, intermediate electrolyte layer for the transportation of charge between the active layer and counter-electrode. In order to bring improvements to various properties of the opto-electronic devices, experiments can be carried out with electrolytes having different states of matter, i.e. solid, quasi-solid etc. In addition to that, alteration to the active layer can also be carried with the introduction of nanoparticles, nanotubes or nano-rods for the enhancement of parameters.

In the current work, CuNWs/rGO/PEODT:PSS based TCE has been integrated within DSPS, as a counter-electrode. This electrode can also serve the purpose of a photo-anode (owing to its high transparency) in dye-sensitized and bulk heterojunction based devices. In addition, efforts can also be made for the fabrication of flexible DSPSs/DSSC devices. This would require major alterations to standard fabrication processes like semiconductor layer deposition and sintering that would no longer remain viable, owing to the temperature restrictions imposed by the components used.

References

1. Suhir, E., Y.-C. Lee, and C. Wong, Micro-and Opto-Electronic Materials and Structures: Physics, Mechanics, Design, Reliability, Packaging: Volume I Materials Physics-Materials Mechanics. Volume II Physical Design-Reliability and Packaging. Vol. 1. 2007: Springer Science & Business Media.
2. Hamakawa, Y., Thin-film solar cells: next generation photovoltaics and its applications. Vol. 13. 2013: Springer Science & Business Media.
3. Nof, S.Y., A.M. Weiner, and G.J. Cheng, Laser and Photonic Systems: Design and Integration. 2014: CRC Press.
4. Liao, C. and F. Yan, Organic semiconductors in organic thin-film transistor-based chemical and biological sensors. Polymer Reviews, 2013. 53: p. 352-406.
5. Maiellaro, G., et al., Ambient light organic sensor in a printed complementary organic TFT technology on flexible plastic foil. IEEE Transactions on Circuits and Systems I: Regular Papers, 2014. 61: p. 1036-1043.
6. Koster, L., S.E. Shaheen, and J.C. Hummelen, Pathways to a new efficiency regime for organic solar cells. Advanced Energy Materials, 2012. 2: p. 1246-1253.
7. Zhang, G., et al., Very high open-circuit voltage ultraviolet photovoltaic diode with its application in optical encoder field. Applied Physics Letters, 2010. 96: p. 28.
8. Zafar, Q., et al., A MEHPPV/VOPcPhO composite based diode as a

photodetector. Sensors and Actuators A: Physical, 2014. 206: p. 138-143.

9. Rauch, T., et al., Near-infrared imaging with quantum-dot-sensitized organic photodiodes. nature photonics, 2009. 3: p. 332-336.

10. Qadir, K.W., Z. Ahmad, and K. Sulaiman, Performance enhancement of NiTsPc based photo sensor using treated TiO2 NPs film. Journal of nanoparticle research, 2014. 16: p. 2705.

11. Qadir, K.W., et al., Binary blend based dye sensitized photo sensor using PCPDTBT and MEH-PPV composite as a light sensitizer. Synthetic Metals, 2015. 210: p. 392-397.

12. Dagli, N., High-speed photonic devices. 2006: CRC press.

13. Maini, A.K., Lasers and optoelectronics: fundamentals, devices and applications. 2013: John Wiley & Sons.

14. Malinowski, P.E., III-N Ultraviolet Detectors for Space Applications. 2011: Pawel E. Malinowski.

15. Deen, M.J. and P.K. Basu, Silicon Photonics: Fundamentals and Devices. 2012: Wiley Chichester, UK.

16. Rao, M.M., Optical Communication. 2001: Universities Press.

17. Gupta, K. and N. Gupta, Advanced semiconducting materials and devices. 2016: Springer.

18. Golio, M., The RF and microwave handbook. 2000: CRC press.

19. Baeg, K.J., et al., Organic light detectors: photodiodes and phototransistors. Advanced materials, 2013. 25: p. 4267-4295.

20. Eren, H., Electronic portable instruments: design and applications. 2003: CRC

Press.

21. Rashid, M.H., Microelectronic circuits: analysis and design. 2016: Cengage learning.
22. Liu, K., M. Sakurai, and M. Aono, ZnO-based ultraviolet photodetectors. Sensors, 2010. 10: p. 8604-8634.
23. Nabet, B., Photodetectors: Materials, Devices and Applications. 2015: Woodhead Publishing.
24. Azapagic, A., A. Emsley, and I. Hamerton, Polymers: the environment and sustainable development. 2003: John Wiley & Sons.
25. Li, Y., Conducting polymers, in Organic Optoelectronic Materials. 2015, Springer. p. 23-50.
26. Barón, M., et al., Glossary of class names of polymers based on chemical structure and molecular architecture (IUPAC Recommendations 2009). Pure and Applied Chemistry, 2009. 81: p. 1131-1186.
27. Shirakawa, H., et al., Synthesis of electrically conducting organic polymers: halogen derivatives of polyacetylene,(CH) x. Journal of the Chemical Society, Chemical Communications, 1977: p. 578-580.
28. Chiang, C., MA Druy, SC Gau, AJ Heeger, EJ Louis, AG MacDiarmid. YW Parkand H. Shirakawa. J. Am. Chem. Sot, 1978. 100: p. 1013.
29. van Haare, J.A., et al., Redox states of long oligothiophenes: two polarons on a single chain. Chemistry-A European Journal, 1998. 4: p. 1509-1522.
30. Bredas, J.L. and G.B. Street, Polarons, bipolarons, and solitons in conducting polymers. Accounts of Chemical Research, 1985. 18: p. 309-315.

31. Chandrasekhar, P., Conducting polymers, fundamentals and applications: a practical approach. 2013: Springer Science & Business Media.

32. Itaka, K., et al., High-Mobility C60 Field-Effect Transistors Fabricated on Molecular-Wetting Controlled Substrates. Advanced Materials, 2006. 18: p. 1713-1716.

33. Pettersson, L.A., L.S. Roman, and O. Inganäs, Modeling photocurrent action spectra of photovoltaic devices based on organic thin films. Journal of Applied Physics, 1999. 86: p. 487-496.

34. Halls, J.J., et al., Exciton diffusion and dissociation in a poly (p-phenylenevinylene)/C60 heterojunction photovoltaic cell. Applied Physics Letters, 1996. 68: p. 3120-3122.

35. Tang, C.W., Two-layer organic photovoltaic cell. Applied Physics Letters, 1986. 48: p. 183-185.

36. Shoaee, S., et al., Acceptor energy level control of charge photogeneration in organic donor/acceptor blends. Journal of the American Chemical Society, 2010. 132: p. 12919-12926.

37. Clarke, T.M., et al., Analysis of charge photogeneration as a key determinant of photocurrent density in polymer: fullerene solar cells. Advanced Materials, 2010. 22: p. 5287-5291.

38. Hoppe, H. and N.S. Sariciftci, Organic solar cells: An overview. Journal of materials research, 2004. 19: p. 1924-1945.

39. Matthew Menke, S., R. Pandey, and R.J. Holmes, Tandem organic photodetectors with tunable, broadband response. Applied Physics Letters, 2012. 101: p. 223301.

40. Jayaweera, P., et al., Dye-sensitized near-infrared room-temperature photovoltaic photon detectors. Applied physics letters, 2004. 85: p. 5754-5756.

41. Wirth, H., K.-A. Weiß, and C. Wiesmeier, Photovoltaic Modules: Technology and Reliability. 2016: Walter de Gruyter GmbH & Co KG.

42. Li, F. and A. Nathan, CCD image sensors in deep-ultraviolet: degradation behavior and damage mechanisms. 2006: Springer Science & Business Media.

43. Fan, K., J. Yu, and W. Ho, Improving photoanodes to obtain highly efficient dye-sensitized solar cells: a brief review. Materials Horizons, 2017. 4: p. 319-344.

44. Shalini, S., et al., Review on natural dye sensitized solar cells: operation, materials and methods. Renewable and Sustainable Energy Reviews, 2015. 51: p. 1306-1325.

45. O'regan, B. and M. Grätzel, A low-cost, high-efficiency solar cell based on dye-sensitized colloidal TiO 2 films. nature, 1991. 353: p. 737-740.

46. Suhaimi, S., et al., Materials for enhanced dye-sensitized solar cell performance: Electrochemical application. Int. J. Electrochem. Sci, 2015. 10: p. 2859-2871.

47. Taya, S.A., et al., Dye-sensitized solar cells using fresh and dried natural dyes. International Journal of Materials Science and Applications, 2013. 2: p. 37-42.

48. Ono, T., T. Yamaguchi, and H. Arakawa, Study on dye-sensitized solar cell using novel infrared dye. Solar Energy Materials and Solar Cells, 2009. 93: p. 831-835.

49. Mathew, S., et al., Dye-sensitized solar cells with 13% efficiency achieved through the molecular engineering of porphyrin sensitizers. Nature chemistry, 2014. 6: p. 242-247.

50. Luque, A. and S. Hegedus, Handbook of photovoltaic science and engineering.

2011: John Wiley & Sons.

51. Karmakar, A.S. and J.P. Ruparelia. A critical review on dye sensitized solar cells. in Internation Conference on Current Trends in Technology. 2011.

52. Bisquert, J., et al., Physical chemical principles of photovoltaic conversion with nanoparticulate, mesoporous dye-sensitized solar cells. The Journal of Physical Chemistry B, 2004. 108: p. 8106-8118.

53. Nazeeruddin, M.K., E. Baranoff, and M. Grätzel, Dye-sensitized solar cells: a brief overview. Solar Energy, 2011. 85: p. 1172-1178.

54. Andrei, C.A., Towards Efficient Photovoltaic Devices: Key Facts and Experiments on Dye Sensitised Solar Cells. 2017: Cambridge Scholars Publishing.

55. Hamadanian, M., H. Sayahi, and A.R. Zolfaghari, Modified multistep electrophoretic deposition of TiO_2 nanoparticles to prepare high quality thin films for dye-sensitized solar cell. Journal of Materials Science, 2012. 47: p. 5845-5851.

56. Gong, J., J. Liang, and K. Sumathy, Review on dye-sensitized solar cells (DSSCs): fundamental concepts and novel materials. Renewable and Sustainable Energy Reviews, 2012. 16: p. 5848-5860.

57. Adedokun, O., T. Kamil, and A.A. Oladiran, Review on Natural Dye-Sensitized Solar Cells (DSSCs). International Journal of Engineering Technologies, IJET, 2016. 2: p. 34-41.

58. Armstrong, G.A. and J.E. Hearst, Carotenoids 2: Genetics and molecular biology of carotenoid pigment biosynthesis. The FASEB Journal, 1996. 10: p. 228-237.

59. Scheer, H., Light-Harvesting in Photosynthesis. Vol. 122. 2012. 247-251.

60. Davies, K., Annual Plant Reviews, Plant Pigments and Their Manipulation. Annual Plant Reviews. 2004: Blackwell Pub.

61. Davies, K., Annual plant reviews, plant pigments and their manipulation. Vol. 14. 2009: John Wiley & Sons.

62. Shalini, S., et al., Status and outlook of sensitizers/dyes used in dye sensitized solar cells (DSSC): a review. International Journal of Energy Research, 2016. 40: p. 1303-1320.

63. Narayan, M. and A. Raturi, Investigation of some common Fijian flower dyes as photosensi-tizers for dye sensitized solar cellsabstract. Applied Solar Energy, 2011. 47: p. 112-117.

64. Maldonado-Valdivia, A.I., et al., Surfactant influence in the performance of titanium dioxide photoelectrodes for dye-sensitized solar cells. Solar Energy, 2013. 91: p. 263-272.

65. Grätzel, M., Dye-sensitized solar cells. Journal of Photochemistry and Photobiology C: Photochemistry Reviews, 2003. 4: p. 145-153.

66. Mehmood, U., et al., Recent advances in dye sensitized solar cells. Advances in Materials Science and Engineering, 2014. 2014.

67. Hara, K. and S. Mori, Dye-Sensitized Solar Cells, in Handbook of Photovoltaic Science and Engineering. 2011, John Wiley & Sons, Ltd. p. 642-674.

68. Islam, A., et al., Dye sensitization of nanocrystalline titanium dioxide with square planar platinum (II) diimine dithiolate complexes. Inorganic chemistry, 2001. 40: p. 5371-5380.

69. Hara, K., Molecular design of sensitizers for dye-sensitized solar cells. Molecular Catalysts for Energy Conversion, 2009: p. 217-250.

70. Mishra, A., M.K. Fischer, and P. Bäuerle, Metal-free organic dyes for dye-sensitized solar cells: From structure: Property relationships to design rules. Angewandte Chemie International Edition, 2009. 48: p. 2474-2499.

71. Jyoti, D., et al. A critical review on mesoporous photoanodes for dye-sensitized solar cells. in Materials Science Forum. 2014. Trans Tech Publ.

72. Jena, A., et al., Dye sensitized solar cells: a review. Transactions of the Indian Ceramic Society, 2012. 71: p. 1-16.

73. Hagfeldt, A., et al., Dye-sensitized solar cells. Chemical reviews, 2010. 110: p. 6595-6663.

74. Kong, F.-T., S.-Y. Dai, and K.-J. Wang, Review of recent progress in dye-sensitized solar cells. Advances in OptoElectronics, 2007. 2007.

75. Ferrere, S., A. Zaban, and B.A. Gregg, Dye sensitization of nanocrystalline tin oxide by perylene derivatives. The Journal of Physical Chemistry B, 1997. 101: p. 4490-4493.

76. Onwona-Agyeman, B., et al., Sensitization of nanocrystalline SnO2 films with indoline dyes. Japanese journal of applied physics, 2005. 44: p. L731.

77. Kay, A. and M. Grätzel, Dye-sensitized core− shell nanocrystals: improved efficiency of mesoporous tin oxide electrodes coated with a thin layer of an insulating oxide. Chemistry of Materials, 2002. 14: p. 2930-2935.

78. Guo, P. and M.A. Aegerter, RU (II) sensitized Nb 2 O 5 solar cell made by the sol-gel process. Thin Solid Films, 1999. 351: p. 290-294.

79. Wang, Z.-S., et al., Significant influence of TiO 2 photoelectrode morphology on the energy conversion efficiency of N719 dye-sensitized solar cell. Coordination chemistry reviews, 2004. 248: p. 1381-1389.

80. Chiba, Y., et al., Dye-sensitized solar cells with conversion efficiency of 11.1%. Japanese Journal of Applied Physics, 2006. 45: p. L638.

81. Calogero, G., et al., A new type of transparent and low cost counter-electrode based on platinum nanoparticles for dye-sensitized solar cells. Energy & Environmental Science, 2011. 4: p. 1838-1844.

82. Syrrokostas, G., et al., Degradation mechanisms of Pt counter-electrodes for dye sensitized solar cells. Solar Energy Materials and Solar Cells, 2012. 103: p. 119-127.

83. Li, P., et al., High-performance and low platinum loading Pt/Carbon black counter-electrode for dye-sensitized solar cells. Solar Energy, 2009. 83: p. 845-849.

84. Velten, J., et al., Carbon nanotube/graphene nanocomposite as efficient counter-electrodes in dye-sensitized solar cells. Nanotechnology, 2012. 23: p. 085201.

85. Baxter, J.B., Commercialization of dye sensitized solar cells: Present status and future research needs to improve efficiency, stability, and manufacturing. Journal of Vacuum Science & Technology A: Vacuum, Surfaces, and Films, 2012. 30: p. 020801.

86. Bella, F., et al., Aqueous dye-sensitized solar cells. Chemical Society Reviews, 2015. 44: p. 3431-3473.

87. Solanki, C.S., Solar Photovoltaic Technology and Systems: A Manual for

Technicians. Trainers and Engineers, PHI Learning Private Limited, Delhi, 2013.

88. Nicewarner-Pena, S.R., et al., Submicrometer metallic barcodes. Science, 2001. 294: p. 137-141.

89. Wang, J.-G., et al., Controllable template synthesis of superconducting Zn nanowires with different microstructures by electrochemical deposition. Nano letters, 2005. 5: p. 1247-1253.

90. de Menten de Horne, F., L. Piraux, and S. Michotte, Fabrication and physical properties of Pb⁄Cu multilayered superconducting nanowires. Applied Physics Letters, 2005. 86: p. 152510.

91. Cui, Y. and C.M. Lieber, Functional nanoscale electronic devices assembled using silicon nanowire building blocks. science, 2001. 291: p. 851-853.

92. Ferry, D.K., Nanowires in nanoelectronics. Science, 2008. 319: p. 579-580.

93. Tseng, G.Y. and J.C. Ellenbogen, Toward nanocomputers. Science, 2001. 294: p. 1293-1294.

94. Vijayaraghavan, A., Graphene – Properties and Characterization, in Springer Handbook of Nanomaterials, R. Vajtai, Editor. 2013, Springer Berlin Heidelberg: Berlin, Heidelberg. p. 39-82.

95. Skotheim, T.A. and J. Reynolds, Handbook of Conducting Polymers, 2 Volume Set. 2007: CRC press.

96. Choy, W.C., Organic solar cells: materials and device physics. 2012: Springer.

97. Nakamura, J.-i., K. Murata, and K. Takahashi, Relation between carrier mobility and cell performance in bulk heterojunction solar cells consisting of soluble polythiophene and fullerene derivatives. Applied physics letters, 2005. 87: p.

132105.

98. Mozer, A.J., et al., Charge carrier mobility in regioregular poly (3-hexylthiophene) probed by transient conductivity techniques: A comparative study. Physical Review B, 2005. 71: p. 035214.

99. Veldman, D., S.C. Meskers, and R.A. Janssen, The Energy of Charge-Transfer States in Electron Donor–Acceptor Blends: Insight into the Energy Losses in Organic Solar Cells. Advanced Functional Materials, 2009. 19: p. 1939-1948.

100. Bashar, S.A., Study of indium tin oxide (ITO) for novel optoelectronic devices. UMIST, Manchester, 1998: p. 106-109.

101. Chopra, K., S. Major, and D. Pandya, Transparent conductors—A status review. Thin solid films, 1983. 102: p. 1-46.

102. Barbé, C.J., et al., Nanocrystalline titanium oxide electrodes for photovoltaic applications. Journal of the American Ceramic Society, 1997. 80: p. 3157-3171.

103. Pekkola, R., Electronic Structure of Solid-State Dye-Sensitized Solar Cells: Synchrotron Induced Photoelectron Spectroscopy on Nanocrystalline TiO2, Newly Developed Dyes and Spiro-MeOTAD. 2014, Technische Universität.

104. Snaith, H.J. and M. Grätzel, Electron and Hole Transport through Mesoporous TiO2 Infiltrated with Spiro-MeOTAD. Advanced Materials, 2007. 19: p. 3643-3647.

105. Kong, E.-H., Y.-J. Chang, and H.M. Jang, Hierarchically Nanostructured Photoelectrodes for Quantum-Dot-Sensitized Solar Cells, in Quantum Dot Solar Cells. 2014, Springer. p. 39-66.

106. Guo, H., et al., Copper nanowires as fully transparent conductive electrodes.

Scientific reports, 2013. 3.

107. Khan, M.I., A study on the optimization of dye-sensitized solar cells. 2013: University of South Florida.

108. Mete, E., et al., Effect of molecular and electronic structure on the light-harvesting properties of dye sensitizers. The Journal of Physical Chemistry C, 2007. 111: p. 7539-7547.

109. Wingard, J. and D.L. Wise, Biosensors with fiberoptics. 2012: Springer Science & Business Media.

110. Elangovan, R., N. Joby, and P. Venkatachalam, Performance of dye-sensitized solar cells based on various sensitizers applied on TiO2-Nb2O5 core/shell photoanode structure. Journal of Solid State Electrochemistry, 2014. 18: p. 1601-1609.

111. Fan, S., et al., Effect of the co-sensitization sequence on the performance of dye-sensitized solar cells with porphyrin and organic dyes. Physical Chemistry Chemical Physics, 2016. 18: p. 932-938.

112. Kumara, N., et al., Layered co-sensitization for enhancement of conversion efficiency of natural dye sensitized solar cells. Journal of alloys and compounds, 2013. 581: p. 186-191.

113. Sharma, G., et al., Cosensitization of dye sensitized solar cells with a thiocyanate free Ru dye and a metal free dye containing thienylfluorene conjugation. Rsc Advances, 2013. 3: p. 6036-6043.

114. Wu, Z., et al., Co-sensitization of N719 with an organic dye for dye-sensitized solar cells application. Bulletin of the Korean Chemical Society, 2014. 35: p.

1449-1454.

115. Hua, Y., et al., Co-sensitization of 3D bulky phenothiazine-cored photosensitizers with planar squaraine dyes for efficient dye-sensitized solar cells. Journal of Materials Chemistry A, 2015. 3: p. 13848-13855.

116. Al-Alwani, M.A., et al., Dye-sensitised solar cells: Development, structure, operation principles, electron kinetics, characterisation, synthesis materials and natural photosensitisers. Renewable and Sustainable Energy Reviews, 2016. 65: p. 183-213.

117. Shetty, A., et al., Temperature dependent electrical characterisation of Pt/HfO2/n-GaN metal-insulator-semiconductor (MIS) Schottky diodes. AIP Advances, 2015. 5: p. 097103.

118. Sharma, G., et al., Stepwise co-sensitization as a useful tool for enhancement of power conversion efficiency of dye-sensitized solar cells: The case of an unsymmetrical porphyrin dyad and a metal-free organic dye. Organic Electronics, 2014. 15: p. 1324-1337.

119. Arredondo, B., et al., Visible light communication system using an organic bulk heterojunction photodetector. Sensors, 2013. 13: p. 12266-12276.

120. Arredondo, B., et al., High-Bandwidth organic photodetector analyzed by impedance spectroscopy. IEEE Photonics Technology Letters, 2012. 24: p. 1868-1871.

121. Manna, E., et al., Organic Photodetectors in Analytical Applications. Electronics, 2015. 4: p. 688-722.

122. Mathew, A., et al., Effect of iodine concentration on the photovoltaic properties of

dye sensitized solar cells for various I 2/LiI ratios. Electrochimica Acta, 2013. 87: p. 92-96.

123. Wu, J., et al., Electrolytes in dye-sensitized solar cells. Chemical reviews, 2015. 115: p. 2136-2173.

124. Pham, V.T.H., et al., Liquid eutectic GaIn as an alternative electrode for PTB7: PCBM organic solar cells. Japanese Journal of Applied Physics, 2017. 56: p. 046501.

125. Wong, W.S. and A. Salleo, Flexible electronics: materials and applications. Vol. 11. 2009: Springer Science & Business Media.

126. Ahmad, Z., et al., Electrical characteristics of poly (methylsilsesquioxane) thin films for non-volatile memory. Solid State Communications, 2011. 151: p. 297-300.

127. Bakshi, U. and A. Godse, Semiconductor Devices & Circuits. 2008, Technical Publications Pune, India.

128. Wetzelaer, G., et al., Origin of the dark-current ideality factor in polymer: fullerene bulk heterojunction solar cells. Applied Physics Letters, 2011. 99: p. 153506.

129. Usami, A., Chapter 3 - Optical and Electrical Modeling of Nanocrystalline Solar Cells A2 - Soga, Tetsuo, in Nanostructured Materials for Solar Energy Conversion. 2006, Elsevier: Amsterdam. p. 81-104.

130. Tvingstedt, K. and C. Deibel, Temperature dependence of ideality factors in organic solar cells and the relation to radiative efficiency. Advanced Energy Materials, 2016. 6.

131. Wagner, L.C., Failure analysis of integrated circuits: tools and techniques. Vol. 494. 2012: Springer Science & Business Media.

132. Aziz, F., et al., Enhancement of electrical properties of vanadyl phthalocyanine derivative by PCBM. Pigment & Resin Technology, 2015. 44: p. 148-156.

133. Vercik, A., Transport model for disordered organic nanocomposites. MRS Online Proceedings Library Archive, 2014. 1660.

134. Mondal, S., et al., Resistive switching behavior in Lu2O3 thin film for advanced flexible memory applications. Nanoscale research letters, 2014. 9: p. 3.

135. Ahmad, Z., M.H. Sayyad, and K.S. Karimov, CuPc based organic-inorganic hetero-junction with Au electrodes. Journal of Semiconductors, 2010. 31: p. 074002.

136. Shikoh, A.S., et al., Integration of the inexpensive CuNWs based transparent counter-electrode with dye sensitized photo sensors. RSC Advances, 2016. 6: p. 53123-53129.

137. Hailegnaw, B., G. Adam, and T. Yohannes, Effect of short chain iodoalkane solvent additives on photovoltaic performance of poly (3-hexylthiophene) and phenyl-C 61-butyric acid methyl ester based bulk heterojunction solar cells. Thin Solid Films, 2015. 589: p. 272-277.

138. Rathmell, A.R. and B.J. Wiley, The synthesis and coating of long, thin copper nanowires to make flexible, transparent conducting films on plastic substrates. Advanced Materials, 2011. 23: p. 4798-4803.

139. Zhao, Y., et al., Rapid and large-scale synthesis of Cu nanowires via a continuous flow solvothermal process and its application in dye-sensitized solar cells

(DSSCs). RSC Advances, 2012. 2: p. 11544-11551.

140. Lyons, P.E., et al., High-performance transparent conductors from networks of gold nanowires. The Journal of Physical Chemistry Letters, 2011. 2: p. 3058-3062.

141. Guo, H., et al., Copper Nanowires as Fully Transparent Conductive Electrodes. Scientific Reports, 2013. 3: p. 2323.

142. Zhu, Z., et al., Ultrahigh aspect ratio copper-nanowire-based hybrid transparent conductive electrodes with PEDOT: PSS and reduced graphene oxide exhibiting reduced surface roughness and improved stability. ACS applied materials & interfaces, 2015. 7: p. 16223-16230.

143. Rathmell, A.R., et al., The growth mechanism of copper nanowires and their properties in flexible, transparent conducting films. Advanced materials, 2010. 22: p. 3558-3563.

144. Kholmanov, I.N., et al., Reduced graphene oxide/copper nanowire hybrid films as high-performance transparent electrodes. ACS nano, 2013. 7: p. 1811-1816.

145. Leem, D.S., et al., Efficient organic solar cells with solution-processed silver nanowire electrodes. Advanced Materials, 2011. 23: p. 4371-4375.

146. Liu, B.-T. and H.-L. Kuo, Graphene/silver nanowire sandwich structures for transparent conductive films. Carbon, 2013. 63: p. 390-396.

147. Kavan, L., J.-H. Yum, and M. Graetzel, Graphene-based cathodes for liquid-junction dye sensitized solar cells: Electrocatalytic and mass transport effects. Electrochimica Acta, 2014. 128: p. 349-359.

148. Chen, L.-C., et al., Electrophoretic deposition of TiO 2 coatings for use in all-

plastic flexible dye-sensitized solar cells. Surface and Coatings Technology, 2015. 284: p. 51-56.

149. Chen, H.-W., et al., Electrophoretic deposition of TiO 2 film on titanium foil for a flexible dye-sensitized solar cell. Electrochimica Acta, 2011. 56: p. 7991-7998.

150. Hamadanian, M., A. Gravand, and V. Jabbari, High performance dye-sensitized solar cells (DSSCs) achieved via electrophoretic technique by optimizing of photoelectrode properties. Materials Science in Semiconductor Processing, 2013. 16: p. 1352-1359.

151. Kalyanasundaram, K., Dye-sensitized solar cells. 2010: EPFL press.

152. Hou, K., et al., Highly crystallized mesoporous TiO 2 films and their applications in dye sensitized solar cells. Journal of Materials Chemistry, 2005. 15: p. 2414-2420.

153. Ângelo, J., et al., Characterization of TiO 2-based semiconductors for photocatalysis by electrochemical impedance spectroscopy. Applied Surface Science, 2016. 387: p. 183-189.